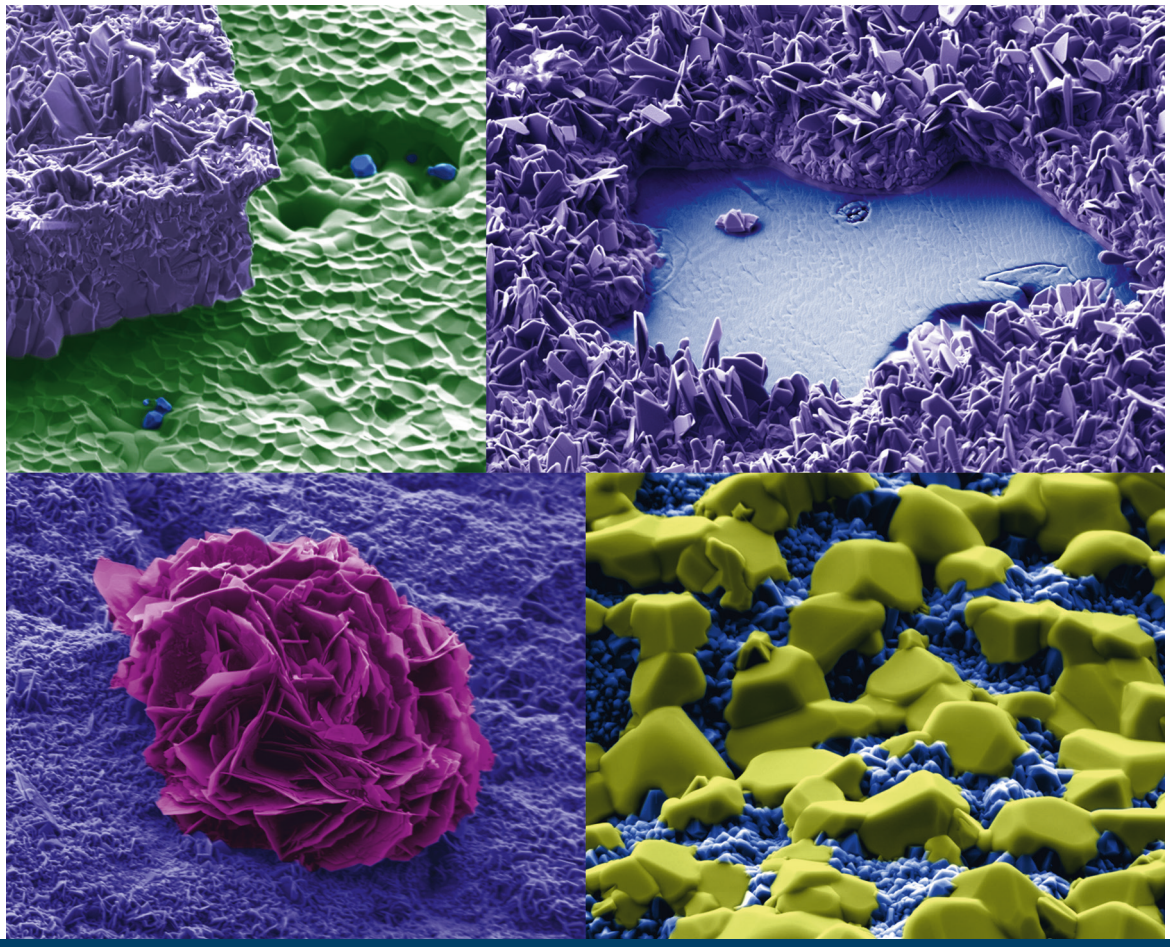

Nanoscale analysis of high-temperature oxidation mechanisms of Cr_2AlC MAX phase and W-Cr-Y self-passivating tungsten alloy

Anicha Jerin Sarah Reuban

Energie & Umwelt / Energy & Environment
Band / Volume 676
ISBN 978-3-95806-855-1

Mitglied der Helmholtz-Gemeinschaft

JÜLICH
Forschungszentrum

Schriften des Forschungszentrums Jülich
Reihe Energie & Umwelt / Energy & Environment Band / Volume 676

Forschungszentrum Jülich GmbH
Institute of Fusion Energy and Nuclear Waste Management (IFN)
Plasma Physics (IFN-1)

Nanoscale analysis of high-temperature oxidation mechanisms of Cr_2AlC MAX phase and W-Cr-Y self-passivating tungsten alloy

Anicha Jerin Sarah Reuban

Schriften des Forschungszentrums Jülich
Reihe Energie & Umwelt / Energy & Environment Band / Volume 676

ISSN 1866-1793 ISBN 978-3-95806-855-1

Bibliografische Information der Deutschen Nationalbibliothek.
Die Deutsche Nationalbibliothek verzeichnet diese Publikation in der
Deutschen Nationalbibliografie; detaillierte Bibliografische Daten
sind im Internet über http://dnb.d-nb.de abrufbar.

Herausgeber und Vertrieb:	Forschungszentrum Jülich GmbH Zentralbibliothek, Verlag 52425 Jülich Tel.: +49 2461 61-5368 Fax: +49 2461 61-6103 zb-publikation@fz-juelich.de www.fz-juelich.de/zb
Umschlaggestaltung:	Grafische Medien, Forschungszentrum Jülich GmbH
Druck:	Grafische Medien, Forschungszentrum Jülich GmbH
Copyright:	Forschungszentrum Jülich 2025

Schriften des Forschungszentrums Jülich
Reihe Energie & Umwelt / Energy & Environment, Band / Volume 676

D 82 (Diss. RWTH Aachen University, 2025)

ISSN 1866-1793
ISBN 978-3-95806-855-1

Vollständig frei verfügbar über das Publikationsportal des Forschungszentrums Jülich (JuSER)
unter www.fz-juelich.de/zb/openaccess.

Abstract

MAX phase materials and self-passivating W-based alloys are potential materials for high-temperature applications, especially for renewable energy technologies where the efficiency is limited by the highest operating temperature of the materials used. An important criterion for the use of such materials at high-temperatures is their resistance to oxidation at these temperatures and environmental conditions, through the formation of a slow-growing, passivating oxide layer. In the present work, the focus is on two such materials: (a) the alumina-forming MAX phase chromium aluminium carbide (Cr_2AlC), which exhibits great potential for use in concentrated solar power (CSP) stations, and (b) the chromia-forming tungsten-based alloy W-11.4Cr-0.6Y, which has been developed as a potential material for use in the plasma-facing first wall of future fusion reactors, and shows increased oxidation resistance due to the addition of yttrium (Y), a well-known reactive element.

In order to develop these materials further and eventually enable their use in high-temperature applications for energy production, the oxidation behaviour and microstructure of the oxide scale under the expected operating conditions, i.e., at temperatures ≥ 1000 °C under a humid atmosphere, were studied. This involved the use of techniques such as thermogravimetric analysis (TGA) to study oxidation kinetics, as well as microstructural characterisation through X-ray diffraction (XRD), focused ion beam – scanning electron microscopy (FIB-SEM), energy-dispersive X-ray spectroscopy (EDX) and transmission electron microscopy (TEM). Since the formation of a passivating oxide scale is a diffusion-controlled process, the study of diffusion pathways such as grain boundaries (GBs), as well as interfaces, which determine the strength of oxide scale adherence, can provide crucial information regarding the oxidation mechanism, both with and without the addition of a reactive element. Hence, a major focus of the present work was on using advanced characterisation tools such as atom probe tomography (APT), which can provide three-dimensional compositional information at the nanoscale. APT was used to study GBs and interfaces, gain more insight into the transport of cations and anions through the oxide scale and bulk material, and determine the key processes that control the growth and formation of the oxide scale.

Since alumina is stable at temperatures greater than 1000 °C, the oxidation behaviour of the MAX phase Cr_2AlC was studied at both 1000 °C and 1200 °C. An α-Al_2O_3 scale is formed at both temperatures, consisting of both inward and outward-growing layers, with a continuous Cr_7C_3 layer beneath the oxide. The decomposition of Cr_2AlC to Cr_7C_3 is the source of more than 70% of aluminium needed for oxide scale formation, while the underlying MAX phase can only tolerate < 1 at.% depletion of Al. Thus, this MAX phase shows a distinctive oxidation behaviour different from the common high-temperature oxidation of alloys. Al diffusion to the oxide scale proceeds differently through the MAX phase and carbide – it occurs predominantly through GBs in Cr_2AlC and through the bulk in Cr_7C_3. However, the rate-

limiting step for oxide scale growth seems to be the ionic diffusion of oxygen through GBs of the large-grained inner alumina layer, resulting in the observed parabolic oxidation kinetics. Importantly, no segregation of Cr, C or any impurities, which could affect ionic transport, was found at these alumina GBs by APT, rendering the results of this work as characteristic of a pure Cr_2AlC oxidation, and shows that the addition of reactive elements could potentially further improve the oxidation resistance.

The oxidation behaviour of the self-passivating tungsten alloy W-11.4Cr-0.6Y, which is a chromia former, was only studied at 1000 °C, since chromia starts to volatilise at higher temperatures. The main focus of this work was on the effect of Y on oxidation resistance, as well as determining the mechanism by which it acts. The oxidation behaviour of the binary alloy W-11.4Cr and the ternary W-11.4Cr-0.6Y alloy, prepared through identical synthesis routes, were studied. A continuous, passivating chromia layer is only obtained with the addition of Y. Although a porous, complex oxide scale containing mixed oxide layers and WO_3 is formed in both cases, the addition of Y results in a less porous oxide scale, which makes it more adherent, and results in a 50-fold reduction in the oxide growth rate, leading to greater oxidation resistance. By performing a two-step oxidation experiment using ^{18}O as a tracer, in combination with APT analysis, it was also shown that Y segregates at chromia GBs and results in the inward growth of oxide, hence providing a possible mechanism for the reactive element effect of Y in chromia-forming W-based alloys.

Kurzzusammenfassung

MAX-Phasen-Materialien sowie selbstpassivierende Legierungen auf Wolframbasis stellen, insbesondere für Technologien im Bereich der erneuerbaren Energien, potenzielle Kandidaten für Hochtemperaturanwendungen dar. Bei diesen Anwendungen ist zu berücksichtigen, dass die Effizienz durch die höchste Betriebstemperatur der verwendeten Materialien begrenzt ist. Ein wesentliches Kriterium für den Einsatz solcher Hochtemperatur-Materialien ist ihre Widerstandsfähigkeit gegen Oxidation bei diesen Temperaturen und Umgebungsbedingungen durch die Bildung einer langsam wachsenden, passivierenden Oxidschicht. Im Rahmen der vorliegenden Arbeit wird der Fokus auf zwei dieser Materialien gelegt: (a) die Aluminiumoxid-bildende MAX-Phase Chrom-Aluminiumcarbid (Cr_2AlC), die ein signifikantes Potenzial für den Einsatz in CSP-Kraftwerken (Concentrated Solar Power) aufweist, und (b) die Chromoxid-bildende Wolfram Legierung W-11.4Cr-0.6Y, welche als potenzielles Material für den Einsatz in der dem Plasma-zugewandten ersten Wand zukünftiger Fusionsreaktoren entwickelt wurde. Durch die Zugabe von Yttrium (Y), einem bekannten reaktiven Element, weist die Legierung eine erhöhte Oxidationsbeständigkeit auf.

Die Weiterentwicklung dieser Materialien mit dem Ziel des Einsatzes in Hochtemperaturanwendungen zur Energieerzeugung erfordert die Untersuchung des Oxidationsverhaltens und der Mikrostruktur der Oxidschicht unter den zu erwartenden Betriebsbedingungen, folglich bei Temperaturen ≥ 1000 °C sowie unter feuchter Atmosphäre. Zu diesem Zweck wurden Verfahren wie die thermogravimetrische Analyse (TGA) zur Untersuchung der Oxidationskinetik, sowie die mikrostrukturelle Charakterisierung durch Röntgendiffraktometrie (XRD), fokussierte Ionenstrahl-Rasterelektronenmikroskopie (FIB-SEM), energiedispersive Röntgenspektroskopie (EDX) und Transmissionselektronenmikroskopie (TEM) eingesetzt. Da die Bildung einer passivierenden Oxidschicht ein diffusionsgesteuerter Prozess ist, kann die Untersuchung von Diffusionspfaden wie Korngrenzen (KG) oder Grenzflächen, sowohl mit als auch ohne Zugabe eines reaktiven Elements, die Stärke der Haftung der Oxidschicht bestimmen und somit entscheidende Informationen über den Oxidationsmechanismus liefern. Daher wurde ein Schwerpunkt der vorliegenden Arbeit auf die Verwendung fortschrittlicher Charakterisierungswerkzeuge gelegt, darunter die Atomsondentomographie (APT), welche dreidimensionale Informationen zur nanoskopischen Zusammensetzung liefern kann. APT wurde eingesetzt, um die Korngrenzen und Grenzflächen zu analysieren, um die Diffusionsprozesse von Kationen und Anionen durch die Oxidschicht sowie das Volumenmaterial zu untersuchen, und um die entscheidenden Prozesse zu identifizieren, welche das Wachstum und die Bildung der Oxidschicht steuern.

Aufgrund der Stabilität von Aluminiumoxid bei Temperaturen über 1000 °C wurde das Oxidationsverhalten der MAX-Phase Cr_2AlC sowohl bei 1000 °C als auch bei 1200 °C untersucht. Bei beiden Temperaturen bildet sich eine α-Al_2O_3-Schicht, die aus nach innen und

außen wachsenden Schichten besteht und eine durchgehende Cr_7C_3-Schicht unter dem Oxid aufweist. Die Zersetzung von Cr_2AlC zu Cr_7C_3 stellt die Quelle von mehr als 70% des für die Bildung der Oxidschicht benötigten Aluminiums dar. Die darunter liegende MAX-Phase hingegen toleriert lediglich eine Verringerung an Aluminium von weniger als 1 at.%. Daher bildet sich in dieser MAX-Phase ein signifikantes Oxidationsverhalten aus, das sich von der konventionellen Hochtemperaturoxidation von Legierungen unterscheidet. Die Diffusion von Aluminium in die Oxidschicht erfolgt in der MAX-Phase und im Karbid in unterschiedlicher Weise. Vorwiegend findet sie durch die Korngrenzen in Cr_2AlC und durch die Masse in Cr_7C_3 statt. Der für das Wachstum der Oxidschicht maßgeblich verantwortliche Prozess ist offenbar die Ionendiffusion von Sauerstoff durch die Korngrenzen der grobkörnigen inneren Aluminiumoxidschicht. Dies führt zu einer beobachtbaren parabolischen Oxidationskinetik. Es sei darauf hingewiesen, dass bei den untersuchten Aluminiumoxid-Korngrenzen keine Entmischung von Chrom, Kohlenstoff oder Verunreinigungen, welche den Ionentransport beeinflussen könnten, durch APT festgestellt wurde. Somit können die Ergebnisse dieser Arbeit als charakteristisch für eine reine Cr_2AlC-Oxidation gelten. Zudem lässt sich ableiten, dass möglicherweise die Zugabe von reaktiven Elementen die Oxidationsbeständigkeit weiter verbessern könnte.

Das Oxidationsverhalten der selbstpassivierenden Wolframlegierung W-11.4Cr-0.6Y, welche Chromoxid bildet, wurde lediglich bei einer Temperatur von 1000 °C untersucht. Grund hierfür sind ist die einsetzende Verflüchtigung von Chromoxid bei höheren Temperaturen. Im Rahmen dieser Arbeit wurde der Fokus auf die Untersuchung der Auswirkungen von Y auf die Oxidationsbeständigkeit sowie die Erforschung des zugrunde liegenden Wirkungsmechanismus gelegt. Des Weiteren wurde das Oxidationsverhalten der binären Legierung W-11.4Cr sowie der ternären Legierung W-11.4Cr-0.6Y, welche durch identische Synthesewege hergestellt wurden, untersucht. Die Bildung einer kontinuierlichen, passivierenden Chromoxidschicht konnte lediglich durch die Zugabe von Y beobachtet werden. Obwohl in beiden Fällen eine poröse, komplexe Oxidschicht mit Mischoxidschichten und WO_3 gebildet wird, resultiert die Zugabe von Y in einer weniger porösen Oxidschicht mit besserer Haftung sowie einer 50-fachen Verringerung der Oxidwachstumsrate, was zu einer höheren Oxidationsbeständigkeit führt. Die Durchführung eines zweistufigen Oxidationsexperiments unter Verwendung von ^{18}O als Tracer in Kombination mit einer APT-Analyse ermöglichte darüber hinaus die Demonstration der Segregation von Y an Chromoxid Korngrenzen und des dadurch bedingten Einwärts-Wachstums von Oxid, was einen möglichen Mechanismus für den reaktiven Elementeffekt von Y in chromoxidbildenden W-basierten Legierungen darstellt.

Table of Contents

Chapter 1 Introduction

Climate change refers to the long-term effect of increased greenhouse gas (GHG) production on average global temperatures and weather patterns. Since the start of the Industrial Age in the 18th century, the major contributor to the increase in GHG production, primarily carbon dioxide (CO_2) and methane (CH_4), is human activities, such as the use of fossil fuels as the main source of energy for transport, heating and powering the electric grid [1]. The effect of this is widespread and concerning – in recent years the number of extreme weather events such as flash floods, wildfires and droughts has increased, rising sea levels threaten the habitability of low lying regions, and with every passing year summer temperature records are being broken [2]. With the climate crisis already starting to have a foothold on our individual lives as well as causing economic and environmental damage, it is crucial to take steps to reduce GHG production.

To keep global increase in temperatures to less than 1.5 °C, which is expected to be the tipping point beyond which irreversible changes may start to take place [3], the global GHG emissions must be reduced by 43% before 2030 and reach net-zero by 2050, as outlined in the Paris Agreement [4]. Reaching these goals requires the reduction in our dependence on fossil fuels as a primary source of energy, which necessitates the development and transition to cleaner energy sources with lower GHG emissions and more sustainable technologies for energy production. These include renewable energy sources such as solar energy, wind power, geothermal energy and nuclear energy.

1.1 Efficiency of energy production

In order for renewable energy technologies to be a more cost-effective alternative to traditional fossil fuel driven technologies, and hence be more likely to be adopted widely, it is important that the efficiency of energy conversion is as high as possible. The energy conversion efficiency, denoted by η, is the ratio between the useful energy output and the total input energy. When the energy conversion is based on a Carnot cycle, which is one of the fundamental thermodynamic cycles to convert heat to work, the efficiency can be expressed as [5]:

$$\eta = 1 - \frac{T_C}{T_H} \qquad \text{(Equation 1.1)}$$

Here, T_C and T_H are the temperatures of the cold and hot reservoirs respectively. T_H represents the highest temperature of the heat source used to power the generator, which means that if a higher T_H is achieved, η will be closer to 1, which indicates a higher efficiency. Even if a given energy technology can achieve very high

temperatures, the efficiency is still limited by the highest temperature that the materials used in such a system can withstand. Therefore, to achieve higher efficiencies, specifically in energy technologies working on the principle of converting heat energy into useful forms of energy, higher operating temperatures will need to be used, which requires the development of high-temperature materials with a combination of suitable properties for the specific energy application.

1.2 High-temperature energy technologies

There are several energy applications where the properties of materials being used is a limiting factor for the highest operating temperature and the resulting efficiency that can be achieved. This is illustrated using examples of two such sustainable energy technologies – concentrated solar power (CSP) and nuclear fusion.

1.2.1 Concentrated solar power (CSP)

The earth receives an average of 1361 W/m^2 of solar irradiance at the top of the atmosphere [6], which diminishes as sunlight passes through the atmosphere to reach the earth's surface. The solar irradiance at the middle latitudes is ~800 W/m^2 [7]. If this solar power is concentrated over a smaller area, with the use of mirrors or lenses for example, this could provide much higher power densities which can be used for direct heat generation or conversion to other forms of power such as electricity. Concentrated solar power (CSP) works on this principle.

A CSP plant primarily consists of three component systems – a solar collector field, a solar receiver and a system for power conversion, and there are four main types of CSP systems. The parabolic trough and linear Fresnel reflector technologies use a linear focus system, and have a relatively low concentration ratio of less than 100. With a point focus system, which is used in the central receiver and dish Stirling concepts, solar power can be concentrated by a factor of more than 1000. Of these, the central receiver system, also known as a solar tower, has a higher power capacity and shows the largest potential for improvement in efficiency and cost reduction [8].

CSP plants based on central receiver technology use a system of rotatable mirrors called heliostats to concentrate and focus solar radiation onto a central receiver mounted atop a tower, as shown in the schematic in **Fig. 1.1**. The receiver gets heated up as a result and this heat is transferred to the power conversion system using a heat transfer fluid (HTF). The material used as a HTF should be thermally stable, have low melting point and high boiling point, low reactivity with the materials it comes in contact with, high thermal conductivity and heat capacity, and low viscosity [9]. Commonly used HTFs include water/steam, thermal oils, molten salts (such as

nitrates, carbonates or halides of Na, K and Li), or even air and other gases [10]. If the HTF can be stored in thermal energy storage facilities, this can also provide a way to produce power in the absence of sunlight.

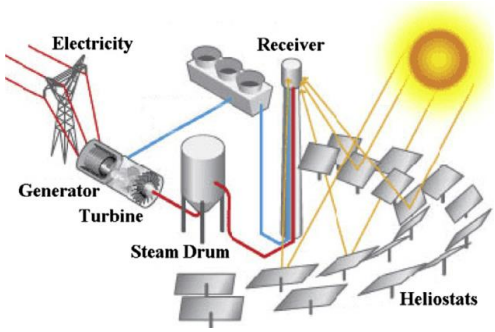

Fig. 1.1: Schematic of a CSP plant using a central receiver system to concentrate solar radiation and generate electricity [7].

In existing commercial CSP plants, the maximum operating temperature is limited to < 600 °C, which is the temperature up to which the nitrate-based molten salts used as the HTF in such plants are stable [11]. The operating temperatures can be increased to ~800 °C by using more thermally stable HTFs (e.g. $MgCl_2$–KCl–NaCl) [12] or by using other approaches such as solid particle receivers, which can potentially reach operating temperatures ≥ 1000 °C [11].

Commercial systems in operation so far use refractory alloys such as Inconel or ceramics such as SiC for the receiver. However, the properties of these materials can worsen at higher temperatures due to phase transformation, creep and thermal fatigue, and degraded oxidation resistance and corrosion in molten salts [7]. In order to operate CSP plants at temperatures > 800 °C and increase efficiency, the material used for the receiver must have a combination of microstructural stability, good thermal conductivity and low expansion coefficient at high temperatures. Importantly, it must also be resistant to oxidation in the atmosphere and corrosion in molten salts or other HTFs, and maintain the specific optical properties such as absorptivity over the operation period of the plant [13].

1.2.2 Nuclear fusion

One of the most important energy applications currently in the research and development stage is nuclear fusion. Making fusion power a reality could provide a reliable source of energy that is not based on fossil fuels. While CSP utilizes the energy produced by the sun, fusion aims to utilize the very process that powers the sun and other stars. Energy generation in the sun's core occurs due to the fusion of hydrogen nuclei (i.e., protons), in a plasma confined under the massive gravitational force of the

sun at very high temperatures, to form helium-4. Since the mass of the helium-4 nucleus is slightly less than the total mass of the four protons it is produced from, the mass difference leads to the release of 26.7 MeV energy according to the mass-energy equivalence principle. However, in a fusion reactor, the use of a fusion reaction involving the hydrogen isotopes deuterium (D) and tritium (T) is proposed, since this reaction has a higher probability of successful initiation [14].

Compared to nuclear fission, using fusion for energy production has many advantages. The D-T fusion reaction, for example, involves the reaction of D and T nuclei to form helium-4 and a free neutron, with the release of 17.6 MeV energy in total. Since the products of this reaction are not radioactive, the amount of high-level nuclear waste produced is reduced. Additionally, fusion is not based on a chain reaction and any changes that cause the cooling of plasma or loss of confinement will immediately stop the reaction. Hence, it is an inherently safe process compared to fission [15].

Magnetic confinement fusion (MCF) is one of the two major branches of fusion reactor designs, the other being inertial confinement. MCF involves creating the fusion reaction in a magnetically confined plasma within a vacuum vessel, with tokamaks and stellerators being two main device configurations using this approach [15]. Large-scale fusion projects such as the Joint European Torus (JET) and the International Thermonuclear Experimental Reactor (ITER), which is currently being built, use tokamak designs.

Fig. 1.2 shows the schematic of a fusion reactor with a tokamak design. It consists of a vacuum vessel, within which the plasma is confined by the magnetic field generated by a system of superconducting magnets consisting of a central solenoid and poloidal and toroidal magnetic field coils. The inside of the vacuum vessel consists of two plasma-facing components (PFCs) – the first wall, which covers most of the internal area, and the divertor, located at the bottom – which are in close proximity to the high-temperature plasma. A cooling system absorbs the heat from the PFCs, which can then be used to produce steam and drive a generator to produce electricity.

Some of the major challenges in the realization of fusion power is creating the conditions for the fusion reaction to take place and sustain the reaction, as well as finding the right materials for the PFCs that can withstand the high particle and heat loads under plasma operation. It should also be able to operate at a high temperature so that the heat generated can be used to produce power with increased efficiency [15].

Tungsten (W), the metal with the highest melting point, shows great potential for use as a plasma-facing material in a fusion reactor [16]. However, one of the major disadvantages of pure W is its catastrophic oxidation behaviour, which becomes

important to consider from the safety perspective. Neutron irradiation of the first wall of the fusion reactor activates W, and WO_3 formed and released into the environment in case of an accident will be radioactive. Therefore, rather than using pure W, W-based alloys with the addition of elements that can help form a passivating oxide layer under an accidental scenario are being developed, so that the material still has the beneficial properties of W while also being oxidation resistant [17].

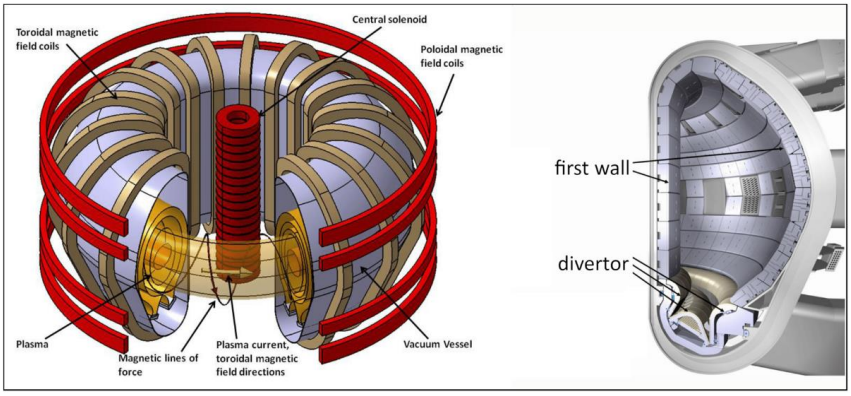

Fig. 1.2: Schematic of a fusion reactor with a tokamak design and the cross-section of the vacuum vessel showing the first wall and divertor [18].

1.2.3 Importance of oxidation resistance

As seen from these examples, there are many properties to consider when selecting materials for high-temperature applications, some being specific to that particular energy application. One of the most important properties is the resistance of these materials to environmental degradation under these high operating temperatures, specifically oxidation and/or corrosion. It is important to use materials that are resistant to oxidation because if a material readily oxidizes under operating conditions, this can lead to a large amount of the material being consumed by the reaction, as well as the damage and loss of structural integrity of the components, which can compromise the safety of the whole system. In the long run, corrosion and oxidation can also lead to considerable economic losses [19].

Although heat-resistant materials such as porcelain and stoneware have existed for millennia, the development of high-temperature materials for energy applications, particularly alloys, primarily started in the 20th century. This was largely triggered by the search for materials that could withstand the high temperatures and centrifugal forces in a turbine engine, which is an essential component of aircraft as well as power generating plants [19]. When solely considering resistance to oxidation, it would seem that ceramic materials like alumina and silica can be a good choice, since they are already in a stable state and do not oxidize further. Although ceramics show very good

oxidation resistance at high temperature as compared to metallic alloys, they tend to be brittle, more prone to cracks and may fracture due to the repeated thermal cycling over a long period of time. They also have lower thermal conductivity as compared to metallic alloys, which increases the chances of thermal fatigue and failure [7]. Some alloys have been developed that show excellent mechanical strength under high temperatures, such as Ni-based superalloys. However, under high temperatures, metallic alloys can undergo changes in the microstructure as well as degradation in oxidation resistance. In addition, given that in some applications the components will be exposed to the humidity in the atmosphere, it is also important to consider the effect of humidity on the oxidation resistance.

No material is perfect, since both metallic alloys and ceramics have their respective disadvantages, and there is always scope for improvement in properties. Hence, the quest for new materials, as well as trying to mitigate the shortcomings of existing material systems, is always on. One of the most attractive materials in this respect is a class of ternary carbides and nitrides called MAX phases, which shows properties bridging those of metals and ceramics. There is also considerable interest in trying to make materials such as W-based alloys more oxidation resistant, given that W is the metal with the highest melting point. These materials, for the most part, are still in the developmental stage and not widely used in real applications, but have attracted attention as materials that could push the frontiers of the highest temperatures that we can operate at and pave the way for the development of new energy technologies.

For the development of new materials and the improvement of old, understanding the fundamental mechanisms is essential. Since oxidation resistance is a key material property that limits the temperature at which a material can be used, the focus of this work is to analyse and explain the oxidation mechanisms of MAX phases and W-based alloys. This can give important insights into how these materials work and help find ways to improve and optimize their performance.

A detailed overview of the various aspects of this work is given in the following chapters. Chapter 2 provides the scientific background for the concepts of oxidation resistance, and the existing knowledge on MAX phases and W-based alloys. Chapter 3 outlines the scope and main objectives of this thesis. The experimental methods used for synthesis, oxidation and characterization, including both microscopic and nanoscale techniques, are described in Chapter 4. Chapter 5 is fully devoted to the analysis and results pertaining to the oxidation mechanism of the MAX phase material Cr_2AlC. Chapter 6 provides a similar analysis of the W-based alloy W-11.4Cr-0.6Y, with a focus on the effect of Y as a reactive element. Finally, in Chapter 7, the key takeaways of this study are mentioned, along with the potential directions for future research in this field and for these material classes.

Chapter 2 Scientific Background

The aim of this chapter is to give an overview of the literature and scientific background of the main topics and materials studied in this project. The first section covers the theory governing the high-temperature oxidation of materials, along with descriptions of the characteristics of passivating oxide scales, as well as the significance of the addition of reactive elements. The second section gives an introduction to MAX phases and their properties, with a particular emphasis on the material Cr_2AlC. The final section gives a summary of W-based alloys, and specifically describes the properties and characteristics of W-11.4Cr-0.6Y. For both these materials, an overview of the current knowledge is provided, describing their unique properties as well as summarizing the open questions pertaining to their oxidation mechanisms.

2.1 Oxidation of materials

The term oxidation is fundamentally defined in electrochemistry as any chemical reaction where the oxidation state of an ion increases, specifically, when it forms a compound such as an oxide, carbide, sulphide, etc. [20]. Although technically all of these processes can be considered 'oxidation' from an electrochemical point of view, this term is more commonly used to denote the reaction of an ion in the presence of oxygen to form an oxide. In the presence of other oxidants such as CO_2, CO, H_2S, SO_2 or SO_3, to name a few, the compound formed could be a carbide or sulphide, and this process is called carburization or sulphidation respectively. In this thesis, the term oxidation specifically refers to the reaction of the material with oxygen in an oxidizing environment, resulting primarily in the formation of an oxide.

2.1.1 Thermodynamics of oxidation

The general reaction for the reaction of a metal with oxygen can be written as:

$$\frac{2x}{y}\mathrm{M} + \mathrm{O}_2 \rightarrow \frac{2}{y}\mathrm{M_xO_y} \qquad \text{(Equation 2.1)}$$

Here, M denotes the metal reacting with oxygen (O_2), to form an oxide (M_xO_y). However, the mere presence of oxygen is not the only factor that determines if this reaction will take place. To determine these factors, the thermodynamics of the oxidation reaction also need to be considered.

The driving force for a reaction to take place is given by the Gibbs free energy (ΔG) of the reaction, which is defined as:

$$\Delta G = \Delta H - T\Delta S \qquad \text{(Equation 2.2)}$$

Here, ΔH is the change in enthalpy, ΔS is change in entropy and T is the temperature. When ΔG > 0, the forward reaction is not thermodynamically possible, ΔG = 0 indicates equilibrium, and ΔG < 0 indicates that a spontaneous reaction is expected.

For the general oxidation reaction shown in Equation 2.1, ΔG can be expressed in terms of the thermodynamic activities (a_i) of the reactants and products as follows:

$$\Delta G = \Delta G^\circ + RT \ln\left(\frac{a_{M_xO_y}^{\frac{2}{y}}}{a_M^{\frac{2x}{y}} \cdot a_{O_2}}\right) \qquad \text{(Equation 2.3)}$$

Here, ΔG° is the change in free energy when all the species are in their standard states and R is the gas constant. Since the activity is taken as unity for pure solids and liquids, $a_{M_xO_y}$ and a_M are both equal to 1. The activity of gaseous species is given by the effective partial pressure, hence $a_{O_2} = p_{O_2}$, where p_{O_2} is the partial pressure of oxygen. This results in the simplification of the expression to:

$$\Delta G = \Delta G^\circ + RT \ln \frac{1}{p_{O_2}} \qquad \text{(Equation 2.4)}$$

At equilibrium, i.e., when ΔG = 0, the standard free energy change for the reaction is as follows:

$$\Delta G^\circ = -RT \ln \frac{1}{p_{O_2}} \qquad \text{(Equation 2.5)}$$

Hence, the two important factors to consider for the oxidation reaction from the point of thermodynamics are the temperature as well as the partial pressure of oxygen. The value of p_{O_2} at equilibrium indicates the minimum partial pressure of oxygen required to form a stable oxide from a pure metal at a given temperature, and is also known as the dissociation pressure.

The Ellingham/Richardson diagram [21] shown in **Fig. 2.1** represents the relationship between the Gibbs free energy, partial pressure of oxygen and temperature. To find the equilibrium p_{O_2} for a given reaction, a line is drawn from the origin (point marked O in the top left) passing through the energy line for the reaction of interest at a specific temperature, and extended till it intersects the p_{O_2} scale. The dashed line in this diagram demonstrates this for the oxidation of Fe at 1000 °C, and shows that a partial pressure of 10^{-15} atm is required for the formation of FeO at this temperature [22]. A similar procedure can be followed to find the equilibrium pressure ratios of H_2/H_2O or CO/CO_2, which are gas mixtures under which oxidation can occur, by drawing a line from the points marked H and C respectively.

The Ellingham/Richardson diagram also illustrates the relative stability of different oxides. The more negative the value of ΔG° is for an oxide, the more thermodynamically stable it is and the lower the value of equilibrium p_{O_2} required for its formation. This explains why elements such as Al, Cr and Si form more stable oxides even at high temperatures than the ones higher up such as Fe and Ni. These elements are hence used for the formation of protective oxide scales, which is described in detail in Section 2.1.5.

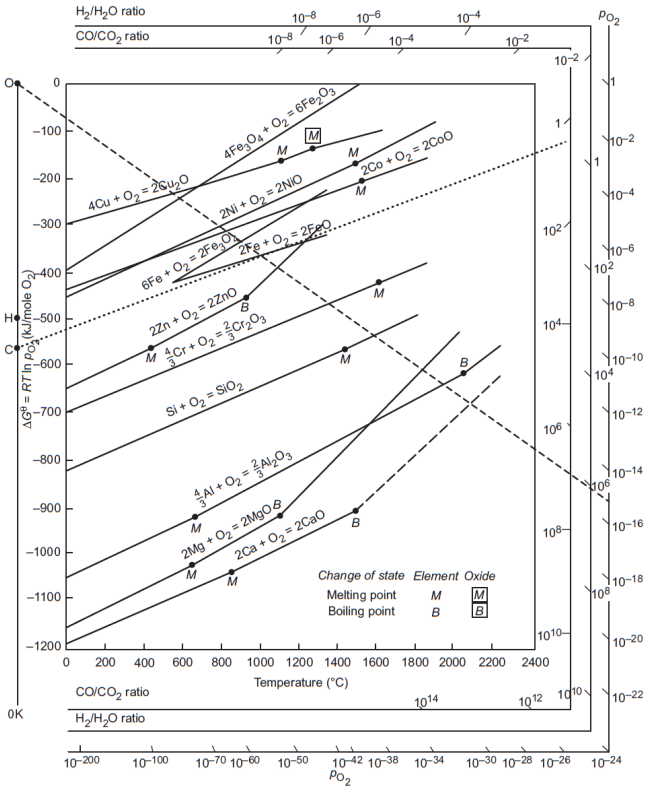

Fig. 2.1: Ellingham/Richardson diagram showing the dependence of the standard Gibbs free energy of formation of selected oxides as a function of temperature [22].

2.1.2 Kinetics of oxidation

Apart from the analysis of the thermodynamic stability of the oxide formed during oxidation, it is also important to consider how quickly the reaction proceeds. From Equation 2.1, we see that the reactants are the metal and oxygen, while the product is the oxide. Therefore, the extent to which oxidation proceeds can be estimated by measuring either the amount of metal or oxygen consumed, or the amount of oxide formed [23].

Measuring the amount of metal consumed can be done by measuring the loss in weight of the original specimen or measuring the metal thickness after the reaction, which either involves the destruction of the specimen or the use of multiple specimens. Measuring the amount of oxide formed based on the oxide thickness can also involve the destruction of the sample in some cases. The only non-destructive methods of measurement are measuring the amount of oxygen consumed or the overall weight gain or loss of the specimen.

By measuring the extent of oxidation with time, the oxidation rate and kinetics can be determined. The different kinds of oxidation kinetics and rate-controlling processes are described in this section, while the next section describes how the rate of oxidation is experimentally measured using thermogravimetric analysis.

2.1.2.1 Linear kinetics

When the amount of oxide growth is directly proportional to the time of oxidation, the oxidation shows linear kinetics, that is:

$$\Delta m = k_l \cdot t \qquad \text{(Equation 2.6)}$$

Here Δm is the mass change of the sample during oxidation, k_l is the linear rate constant and t is time. When oxidation follows linear kinetics, this is an indication that the oxidation reaction is controlled by a planar phase boundary process, i.e., the reaction of metal ions with oxygen ions at the metal-gas interface [19]. This is typically seen at the initial stage of oxidation, where the oxygen is in direct contact with metal ions and they readily react with each other. In the case of alloys and materials with more than one metallic ion that can be oxidized at the given temperature and p_{O_2}, this means that multiple oxides can be formed simultaneously, including mixed oxides. In materials showing good oxidation resistance, this stage is often called the transient stage of oxidation since it lasts for a short time and then the more stable oxide formation starts to dominate, after which the rate of oxidation typically slows down to parabolic or sub-parabolic kinetics. However, in materials that do not form a passivating oxide, the kinetics remains linear or even faster than linear, since the oxide growth continues to be controlled by the direct reaction of metal with oxygen. This is due to the availability of open paths to the underlying metal, for instance through cracks or voids in the oxide.

2.1.2.2 Parabolic kinetics

When the amount of oxide formed decreases with time, such that it is directly proportional to the square root of time, the oxidation follows parabolic kinetics:

$$\Delta m = k_p \cdot t^{1/2} \qquad \text{(Equation 2.7)}$$

Here, k_p is the parabolic rate constant. As derived by Wagner in his theory of metal oxidation [24], parabolic kinetics is shown by materials where the oxide growth is diffusion-controlled, that is, the rate-controlling step is the diffusion of cations (positively charged ions) and/or anions (negatively charged ions) through the oxide scale. This can also be expressed in terms of migration of electrons and holes across the oxide scale. According to Wagner's theory, it is assumed that the oxide layer is thick, fully adherent and dense, and that the metal-oxide and oxide-gas interfaces are in thermodynamic equilibrium, i.e., the concentrations of the diffusing species at these interfaces does not change with time.

The further growth of the oxide is determined either by (a) the diffusion of metal ions through the oxide layer towards the oxide-gas interface, in which case the oxide growth is outward, or (b) the diffusion of oxygen ions through the oxide scale towards the oxide-metal interface, in which case the oxide growth is inward. The direction of growth depends on whether the diffusion of cations or oxygen through the oxide scale is more significant. The oxide growth is not always mono-directional, it can also be a combination of inward and outward growth, which indicates that the diffusion of cations and oxygen ions are both significant.

2.1.2.3 Sub-parabolic and cubic kinetics

For some materials, the rate of oxidation is often found to be even slower than parabolic, in which case it is termed as sub-parabolic kinetics. Sometimes, the oxidation rate fits to a cubic rate law, i.e., the oxide growth is proportional to the cube root of oxidation time. When a material shows sub-parabolic or cubic kinetics, the oxide growth is still diffusion controlled, but it is an indication that there is another factor that slows down the diffusion with time. For example, if the ions diffuse via the grain boundaries (GBs) of the oxide scale, a factor that slows down the diffusion could be the coarsening of grains in the oxide layer, since it decreases the available grain boundary area for diffusion [25].

In most materials which form a passivating oxide layer, the rate of oxide growth is governed by parabolic or sub-parabolic kinetics over the long-term, which are both essentially diffusion-controlled processes. Hence, the diffusion of cations and anions plays a central role in the kinetics of oxidation resistant materials, which is why studying the ionic transport through the oxide as well as the bulk material is important to understand the mechanism of oxidation.

2.1.3 Thermogravimetric analysis

The analysis of oxidation rate by measuring the weight gained in the process of oxidation is called thermogravimetric analysis (TGA). While the weight gained by the

specimen can be determined by oxidizing several samples in a furnace and measuring the weight at specific points of time, the more common and accurate method is to continuously measure the mass gained by the sample using a microbalance setup. This method is usually more expensive and needs more specific equipment, such as having a microbalance with high sensitivity, which also needs to be protected from corrosive gases by flushing it with a noble gas. Helium is commonly used since it is lighter than most gases and hence keeps the microbalance at the top of the setup protected. The weight change (Δm) measured by the microbalance is transmitted to a data acquisition system, and specific programs can be used to immediately visualize the data, which gives us an idea of how quickly the oxidation proceeds. More details about the experimental setup for thermogravimetric analysis are described in Section 4.2.1.

2.1.3.1 Analysis of thermogravimetric data

The kinetics of oxidation, as described earlier, usually fit to linear, parabolic or cubic functions. A more generalized approach to the analysis of thermogravimetric data is by fitting the data to a power law equation, of the general form [26]:

$$\Delta m = k \cdot t^n \qquad \text{(Equation 2.8)}$$

Here, instead of having an equation where the the time t is raised to a fixed power, it is assigned to a variable parameter n, which is called the scale growth exponent. As a general rule, the lower the value of n, the slower and hence more oxidation resistant the material is. By fitting the data to this general equation first, and looking at the value of n, the oxidation kinetics shown by the material can be determined. This is especially useful when trying to determine if the data fits better to a parabolic or cubic equation, or if it is even slower than cubic in some cases.

However, it must be noted that the most common approach to analysing thermogravimetric data traditionally has been to fit the data to a parabolic equation, such as Equation 2.4, and compare the behaviour of different materials or alloy compositions by comparing the value of the parabolic rate constant. A lower value of k_p indicates that the oxidation proceeds more slowly, and hence is an indication of better oxidation resistance. Although this is not the best method, the analyses done in older studies often use this approach. Hence, it may be necessary to also analyse data using this method in order to compare rate constants, for instance.

2.1.3.2 Effect of volatilization

Along with the growth of the oxide, according to Equation 2.1, there can be additional reactions, depending on the conditions of oxidation. For example, Cr_2O_3 can react further with oxygen and water vapour and form gaseous species such as CrO_3, $CrO_2(OH)_2$ and $CrO_2(OH)$, especially at temperatures higher than 1000 °C (more details in Section 2.1.5.2). During the oxidation of W on the other hand, the WO_3

formed can directly sublimate into the gaseous form at temperatures higher than 900 °C [27]. In such cases, when the weight change of the sample is measured through thermogravimetry, the data obtained is a combination of mass gain due to oxidation as well as mass loss due to volatilization, which can be incorporated as an additional constant volatilisation loss term in the rate equation. Sublimation rates can also be measured using dedicated setups, such as the attachment of a collecting plate to a normal TGA setup to collect sublimated material and measuring the mass gain of this plate to determine the amount of material sublimated [28].

2.1.4 Evaluation of oxidation resistance

In the previous sections, the various thermodynamic and kinetic aspects of an oxidation reaction were explored. Whether a material shows good oxidation resistance or not depends on many factors related to both the thermodynamics and kinetics of the reaction, as well as the morphology and microstructure of the oxide that is formed. The most important factor is the ability of the material to form a passivating oxide layer under the given conditions.

One of the most basic factors used to determine if a certain oxide can form a protective layer is the Pilling-Bedworth ratio (PBR) [19]. This is defined as the ratio between the volume of oxide formed and the volume of metal that was consumed in the process of forming the oxide, that is:

$$PBR = \frac{V_{M_xO_y}}{x \cdot V_M} \qquad \text{(Equation 2. 9)}$$

A ratio of less than 1 cannot result in the formation of a protective oxide since the oxide formed will not fully cover the surface of the material. On the other hand, if the ratio is too high, the oxide formed will be very thick and will not be mechanically stable since the amount of stress increases with thickness. The ideal PBR is around 1.5 [29]. Although this is a simple way to determine if a protective oxide can be formed, it is not a foolproof method, since metals such as Cr and Si have a PBR of ~2 and are still some of the best passivating oxide formers, after Al which has a PBR of 1.3.

One of the assumptions of this method is that the oxide formed grows in the inward direction, in which case having a ratio greater than 1 can cause mechanical stresses [22]. If the oxide with a PBR > 1 grows in the outward direction, i.e., new oxide forms at the oxide-gas interface, the growth is unconstrained. However, outward growth poses other problems, such as the increased chance of void formation at the metal-oxide interface, which can lead to spallation. Therefore, although PBR can be a useful parameter in some cases, there are multiple factors to be taken into account when determining the ability of a material to be oxidation resistant.

From the thermodynamics of oxidation, it is evident that oxidation and corrosion at high temperatures cannot be completely eliminated for most engineering materials, but the key is to form a stable, protective oxide scale such that the further growth of the oxide slows down. For this to be realized, the oxide scale must have the following properties [29]:

- **High thermodynamic stability:** The oxide formed must be stable under the given conditions, without decomposing into other reaction products. This means that $\Delta G°$ for the formation of the oxide is highly negative, i.e., in the Ellingham-Richardson diagram the line representing the formation of this oxide should be lower than other less-favourable oxides.
- **High melting temperature:** The melting point of the oxide formed should be higher than the highest operating temperature intended for the material. Some oxides such as Cu_2O have a melting point of 1235 °C, which is relatively low for oxides. For comparison, the melting point of Al_2O_3 is 2072 °C and Cr_2O_3 is 2435 °C. The oxide formed should not sublimate under these conditions as well.
- **Low growth rate:** The rate of oxide growth should be low and should also slow down with time. The faster the oxide grows, the thicker the oxide scale gets, which can cause mechanical stresses, especially when the growth direction is inward.
- **Good adhesion to the metal surface:** The oxide formed must adhere well to the underlying surface. In other words, the metal-oxide interface must be strong. The formation of voids at this interface can make it weaker and could lead to less adhesion. The segregation of certain elements at this interface, particularly sulphur, is also known to destabilize the interface and make it prone to delamination [30].
- **High density and homogeneity:** The oxide formed must be dense, with no cracks and voids. The presence of cracks or open voids can provide faster paths for the diffusion of oxygen to the underlying material, which can cause an increase in the oxidation rate or even lead to breakaway oxidation in some materials [31]. Additionally, it is an advantage to have materials that can self-heal in case of a damaged or cracked oxide layer, which has been observed in some MAX phases like Ti_2AlC and Ti_3AlC_2 [26].
- **Similar CTE as underlying material:** When the coefficient of thermal expansion (CTE) of the oxide formed and the underlying material are very different, this can lead to the development of large stresses in the oxide, which can result in cracking or delamination. This is particularly important to consider in applications where the material is subjected to cyclic heat loads. In a CSP receiver for example, the material undergoes rapid heating and cooling during times of sun and clouds, which can put a lot of strain on the oxide layer if the difference in CTE is large.

2.1.5 Passivating oxide scales

When considering the factors for good oxidation resistance described in Section 2.1.4, such as thermodynamic stability and slow growth of the oxide, there are primarily three oxides that satisfy these criteria: aluminium oxide or alumina (Al_2O_3), chromium oxide or chromia (Cr_2O_3) and silicon dioxide or silica (SiO_2). Therefore, in order to design materials that can show good oxidation resistance by forming a passivating oxide layer by the selective oxidation of one of these elements, the material must contain a sufficient amount of Al, Cr or Si. The minimum amount of the particular element required can vary depending on the element and the alloy system. This can also be influenced by the addition of certain elements in minor quantities, as well as the reactive element effect, which will be described in detail in a later section.

2.1.5.1 Alumina scales

Aluminium oxide, more commonly referred to as alumina, has a hexagonal crystal structure as the thermodynamically stable α phase, also known as corundum. It also has other metastable forms such as the monoclinic θ-Al_2O_3, cubic γ-Al_2O_3, tetragonal δ-Al_2O_3, hexagonal ε-Al_2O_3, κ'-Al_2O_3 and X-Al_2O_3 [32].

Since pure Al has a melting point of 660 °C at standard atmospheric pressure (1 atm), studies on the oxidation resistance of alumina at high temperatures can only be performed on alumina-forming alloys and compounds. The most common and well-studied alumina formers are the aluminides Ni-Al and Fe-Al, and the Al-containing Ni and Fe-based Ni-Cr-Al and Fe-Cr-Al alloy systems [30]. Among ceramics, AlN is the most well-studied alumina former, while Al_4C_3 is also expected to form alumina but has only limited studies [33].

Coming to the kinetics of alumina formation, alumina typically grows at a slower rate than chromia when comparing parabolic rate constants. Additionally, unlike chromia, which forms volatile species and hence the operating temperature is limited to less than 1000 °C, alumina is stable up to temperatures of 1300 °C, at which point it can volatilize in the presence of water according to the following reaction [34]:

$$\frac{1}{2}Al_2O_3(s) + \frac{3}{2}H_2O(g) \rightarrow Al(OH)_3(g) \qquad \text{(Equation 2. 10)}$$

Since alumina grows more slowly and is also stable up to a higher temperature, alumina scales are preferred over chromia especially for high-temperature applications.

In Ni-Cr-Al and Fe-Cr-Al systems, which typically contain ~20 wt.% of Cr, a minimum of 5 wt.% Al is necessary for the formation of a protective alumina scale at temperatures of 1000 °C or greater. Even if the amount of Al is lower than this value,

these alloys have enough Cr to form a chromia layer, however this limits their application to temperatures less than 1000 °C due to the volatilization of chromia. Having too much Al can also negatively affect the mechanical properties of these alloys, such as causing a reduction in ductility [35].

Alumina is a highly stoichiometric compound, i.e., the concentration of native point defects (i.e., oxygen and aluminium vacancies $V_O^{\cdot\cdot}$ and $V_{Al}^{'''}$) is extremely low and as a result the intrinsic diffusion is very slow [32]. For example, the bulk diffusivity of oxygen at 1100 °C is ~10^{-15} cm^2s^{-1}, which is far too low and does not explain the observed rates of oxide growth. The GB diffusion of oxygen is much faster, for example, it is 10^5 to 10^6 times higher than bulk diffusion at temperatures of 1300-1500 °C, which can be studied using ^{18}O tracers. Similar data for Al boundary diffusion does not exist since it has only one stable isotope. Nevertheless, it is clear that the kinetics of oxidation in alumina formers is controlled by GB diffusion [32].

The formation of the metastable forms of alumina can occur under certain conditions and depends on factors such as the temperature of oxidation, partial pressure of oxygen, as well as the presence of impurities [35]. These metastable forms also have different morphologies and are usually formed at the transient stage. They can transform into α-Al_2O_3 under more favourable conditions for the formation of the stable phase, usually when there is an increase in temperature, since α-Al_2O_3 is more stable at higher temperatures. This can sometimes lead to the development of tensile stresses or void formation in the scale, since α-Al_2O_3 is more dense and the unit cell occupies approximately 8-13% less volume than the metastable phases [32,36]. Nevertheless, the possible formation of transient phases of alumina makes the understanding of the growth of alumina scales more complex than chromia scales.

2.1.5.2 Chromia scales

Chromium oxide, more commonly referred to as chromia, has the chemical formula Cr_2O_3 and has a hexagonal crystal structure similar to the structure of corundum (α-Al_2O_3).

Stainless steel is one of the well-known examples of alloys in which the addition of Cr to carbon steel (along with other alloying additions such as Ni) results in the formation of a thin passivating chromia film which prevents the rusting of steel in air and aqueous environments. However, stainless steels are not typically designed for high-temperature applications. For example, the most common grade of stainless steel, Type 304, contains 18 wt.% Cr and is corrosion resistant up to ~870 °C [37]. Ferritic grade steels like Fe-Cr-Al are designed for increased oxidation resistance at high-temperatures, which contain the addition of ~5 wt.% Al, and forms a protective alumina scale instead.

Common chromia formers include Ni-Cr, Fe-Cr, Fe-Ni-Cr and Co-Cr alloys. At least 12 wt.% of Cr is necessary in most alloys for the formation of a protective chromia scale. However, due to the formation of a depletion layer below the oxide, which can compromise the ability of the alloy to continue forming a protective chromia layer in the event of damage to the already existing scale, it is common to increase the amount of Cr to 18-20 wt.% in Ni-Cr alloys, 20-25 wt.% in Fe-Cr alloys and up to 30 wt.% in Co-Cr alloys [38].

The use of passivating chromia-forming materials for high-temperature applications is practically limited to ≤ 900 °C due to the volatilization of chromia at higher temperatures. At temperatures ≥ 1000 °C, chromia reacts further with oxygen and water vapour and forms gaseous species such as CrO_3, $CrO_2(OH)_2$ and $CrO_2(OH)$, according to the following equations [34]:

$$\frac{1}{2}Cr_2O_3(s) + \frac{3}{4}O_2(g) \rightarrow CrO_3(g) \qquad \text{(Equation 2. 11)}$$

$$\frac{1}{2}Cr_2O_3(s) + \frac{3}{4}O_2(g) + H_2O\,(g) \rightarrow CrO_2(OH)_2(g) \qquad \text{(Equation 2. 12)}$$

$$\frac{1}{2}Cr_2O_3(s) + \frac{1}{2}O_2(g) + \frac{1}{2}H_2O\,(g) \rightarrow CrO_2(OH)(g) \qquad \text{(Equation 2. 13)}$$

This leads to the loss of chromia scale and also creates the possibility of undesired Cr deposition in other parts of the system. For example, ferritic stainless steel, a potential material for use in solid oxide fuel cells (SOFCs), is a chromia former. When exposed to high temperatures, the volatile Cr-containing species formed can be deposited at the cathode-electrolyte interface, leading to blocking of catalytic sites for the oxygen reduction reaction, also called cathode poisoning [39].

Chromia scales typically grow in the outward direction, i.e., it is controlled by the diffusion of Cr towards the oxide-gas interface [40]. It has been shown that GB diffusion is much faster than bulk diffusion both for Cr and O, however there are contradictory results regarding whether Cr or O self-diffusion is faster [41].

2.1.5.3 Silica scales

Silica (SiO_2) as a protective oxide scale is typically a feature of ceramics or intermetallic compounds. In many non-oxide ceramics such as $MoSi_2$, $FeSi_2$, SiC and Si_3N_4, the formation of a silica scale is an important factor that enhances the high-temperature performance of these materials [33]. The use of Si as an alloying element in metallic alloys is limited – it is usually at very low concentrations since it reduces the weldability and toughness of alloys due to the formation of intermetallic compounds with other elements present [38]. The amount of Si that can be used is usually not enough to form a single phase passivating silica scale in alloys, hence alloys are more commonly designed to either form a protective chromia or alumina scale. Some silica

formers like SiC also show active oxidation at low pO_2 and high temperature, when SiO vapour is formed rather than solid SiO_2. This can lead to mass loss rather than mass gain. The formation of a passivating SiO_2 layer is favoured at high pO_2 and very high temperatures [42]. Hence, silica formers show good oxidation resistance only under specific conditions.

2.1.6 Reactive element effect

It has been observed that the small addition (< 1 wt.%) of certain chemically reactive elements such as Y, Zr, Hf, La and Ce to chromia and alumina forming alloys drastically increases the oxidation resistance and adherence of the scale to the underlying material. This is known as the reactive element effect. The first application of this effect was demonstrated and patented by Pfeil in 1937 [43], where the addition of up to 0.5 wt.% Ce to the chromia-forming alloy Ni-Cr was shown to improve its oxidation resistance and make it suitable for making electrical resistance elements.

The reactive elements have ionic sizes much greater than that of the other elements in the alloy, resulting in limited solubility in the alloy. They also tend to have a strong affinity for elements such as oxygen and sulphur. Hence, they are usually found as secondary phases, even if they are added initially as an alloying element, as seen in W-Cr-Y alloys where Y is present as Y-O particles after the material is synthesized [44]. The incorporation of these elements in the material can be in the form of dispersed oxides, intermetallic compounds, ion implantation into the alloy, or very thin deposits of the oxide onto the external surface of the alloy [45].

The beneficial effects of the addition of reactive elements are many-fold, as described below:

- **Increased adhesion of the scale:** The oxide scale adherence to the underlying material is greatly increased – no scale spallation occurs even after thermal cycling tests [46,47]. The extent of wrinkling and detachment of the scale is also decreased [30].
- **Reduction of the parabolic rate constant:** In chromia formers, the growth rate of the oxide scale is reduced by a factor of 10 or more, resulting in a more slow-growing scale. A thinner scale is also less susceptible to spallation due to lower mechanical stresses [48].
- **Change in growth mechanism of the scale:** In chromia, the growth mechanism changes from outward (i.e., dominated by outward cation diffusion) to inward (i.e., dominated by inward oxygen ion diffusion) [49]. New growth of the oxide typically occurs at the oxide-gas interface, but the addition of reactive elements causes it to occur at the oxide-alloy interface instead, which can reduce the possibility of void formation at this interface. In alumina formers, the growth

mechanism changes from mixed growth to being predominantly inward in the presence of reactive elements [30].

- **Alteration of the oxide microstructure:** The addition of reactive elements results in finer grained chromia scales, with grain growth in the direction towards the oxide-metal interface [49]. In alumina scales, the microstructure changes from coarse and equiaxed grains to fine and columnar [30]. A finer grain size can improve the mechanical properties of the scale, such as plasticity.
- **Reduction of the minimum amount of Cr or Al required:** The amount of Cr necessary to form a continuous, protective chromia scale, is reduced from about 20-35 wt.% to 10-13 wt.% in common binary alloys with the addition of reactive elements [50].

Although the addition of reactive elements is beneficial for both chromia- and alumina-forming materials, especially by making the scale more resilient to stresses generated due to thermal shock, the effect is more pronounced in chromia formers.

While the effects of reactive element addition are well known, there is still a lot of debate about the exact mechanism by which these elements act which gives rise to these desirable effects. The most commonly proposed mechanisms are as follows:

- **Segregation of the reactive element at oxide scale GBs:** It has been observed that reactive elements often segregate at the GBs of chromia and alumina scales formed on doped alloys. This segregation can alter the amount of cationic and/or anionic diffusion through the oxide scale, which in turn can affect the transport processes responsible for continued growth of the oxide [35]. For example, in chromia formers, the presence of Y segregation at chromia GBs hinders the GB diffusion of Cr ions, which makes the inward diffusion of oxygen ions the dominant process, and hence changes the oxide growth direction from outward to inward. It has also been shown to decrease the diffusion of oxygen, which can reduce the rate of growth of the oxide as well [49].
- **Elimination/reduction of sulphur segregation:** Sulphur segregation at the oxide-alloy interface is known to weaken the interface and increase the chance of scale spallation. Since the reactive elements have a high affinity for sulphur, they can form sulphide or oxy-sulphide particles and thus reduce the possibility of sulphur segregation at the interface. Another proposed mechanism is the preferential segregation of sulphur to the surfaces of the internal reactive oxide particles rather than that of the oxide scale, which can also help strengthen the oxide-alloy interface by preventing the contamination of this interface [30].
- **Growth of oxide "pegs" or intrusions into the alloy:** In some doped alloys, there is a growth of pegs at the oxide-alloy interface that grow into the alloy. These pegs are usually mixed oxides containing the reactive element. The growth of these

structures is believed to support the adhesion of the oxide layer to the substrate [45]. However, pegging is absent in some scales which still show good adherence, and some scales show poor adherence despite the presence of pegs [50]. Therefore, pegging may be a contributing factor for increased oxide scale adherence in some alloys but cannot explain the reactive element effect on its own.

Another important point to note is that the addition of reactive elements is only beneficial when added in small quantities. Excessive addition can result in the formation of large amounts of secondary phases, which are susceptible to internal oxidation and can degrade the oxidation resistance rather than improve it [30].

2.1.7 Effect of impurities

Many commonly used materials have some amount of impurities, which can be incorporated from the raw materials or during the synthesis process. Impurities tend to segregate primarily at defects, such as GBs and interfaces, rather than within the lattice. Even if present in low concentrations in the bulk of the material, the segregation of impurities at GBs and interfaces could affect transport processes through the oxide scale as well as the alloy, and also affect the stability of interfaces, especially when there is more than a monolayer coverage of impurity atoms at these two-dimensional defects. As mentioned earlier, diffusion through both alumina and chromia scales is primarily via GBs, hence the analysis of GBs is an important aspect of the study of oxidation mechanisms in these systems. The most significant impurity that affects interface stability is the presence of sulphur, hence efforts are made to keep the amount of sulphur low in the manufacture of the material or to mitigate the effects of sulphur by using reactive elements [30]. The segregation of some aliovalent elements such as Nb at oxide GBs has also been found to accelerate the rate of oxidation [51].

It is a point worth noting that sometimes reactive elements can be unintentionally present as impurities, and since they have a significant effect even at low concentrations, they can affect the oxidation behaviour of what is believed to be an undoped alloy. It is important to analyse impurity concentrations and distribution so that the possible unintended beneficial or detrimental effects can be understood better.

2.1.8 Effect of water vapour

Water vapour is naturally present in the atmosphere, and is also a component of many industrially important gases such as syngas and coal gas as well as combustion gases. The presence of water vapour can affect the oxidation behaviour of materials in different ways. In steels, oxidation in water vapour containing environments can drastically change the growth rate, microstructure and phases formed. For example, a very thin protective oxide scale is formed when the chromia-forming P91 steel is

oxidized in a dry N_2-1%O_2 atmosphere, but the addition of 2% H_2O results in the formation of a porous, rapidly growing multiphase scale [52]. In Ti_2AlC, the oxidation rate is slightly faster in a humid atmosphere, compared to a dry air oxidation at the same temperature and duration [53]. On the contrary, the α-Al_2O_3 scales formed on reactive element doped alloys grow more slowly in the presence of water vapour, and also seems to enhance the formation of transient phases of alumina [54].

Water vapour can affect oxidation by participating in reactions at the oxide-gas interface, which can produce volatile hydrated species such as hydroxides and oxyhydroxides. This is a well-known disadvantage of chromia scales which limits their use to ≤ 900 °C. Water vapour can also affect diffusion within the oxide scale, possibly due to the formation of hydrogen or hydroxyl species which can affect vacancy concentrations within the scale. The effect of water vapour on alumina formers is made more complicated by its effect on favouring transient alumina formation [55].

In any case, for most applications, water vapour is invariably present, and it is important to consider the potential impact this might have on the oxidation resistance of the material.

2.2 MAX phases

MAX phases are a large class of nanolaminated materials with a hexagonal layered structure. The earliest MAX phases discovered were ternary carbides and nitrides consisting of an early transition metal (M), a Group-A element (i.e., Group 13-16) (A) and carbon or nitrogen (X), with the general formula $M_{n+1}AX_n$, where n is typically 1, 2 or 3. The ternaries M_2AX, M_3AX_2 and M_4AX_3 are also commonly denoted as 211, 312 and 413 phases respectively. Apart from the ternaries, additional elements can also be introduced to form either solid solution MAX phases, where the added elements form a solid solution at the M, A and/or X sites (e.g. $(Ti_{1-x}Cr_x)_2AlC$), or chemically-ordered MAX phases, where elements are added at a specific ratio and occupy well-defined positions in the crystal structure (e.g. Cr_2TiAlC_2). Recently, the definition of MAX phases has been expanded to include B and P as X elements [56]. There are more than 340 different MAX phase compositions that have been successfully synthesised so far, and around 180 more new compositions have been identified as theoretically stable but not confirmed experimentally yet [56]. **Fig. 2.2** shows all the elements in the periodic table that form the 342 MAX phases discovered as of the year 2024.

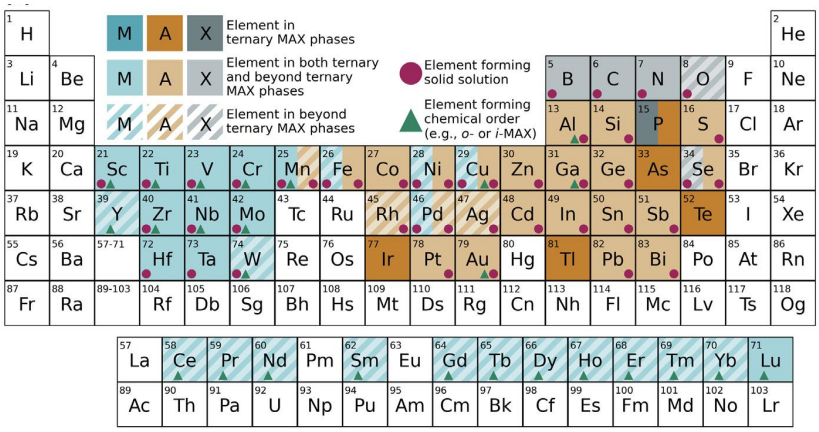

Fig. 2.2: An overview of all elements that have been shown to form stable MAX phases as of the year 2024, including ternary MAX phases and beyond ternary phases such as solid-solution and chemically-ordered MAX phases [56].

MAX phases are well known for their unique combination of properties and are considered to be a bridge between metals and ceramics. They are easily machinable and highly resistant to thermal shock, while also being lightweight and stiff. They behave like metallic conductors of electricity and heat, while additionally, some phases are also oxidation and corrosion resistant. The characteristic combination of properties is attributed to the nature of their crystal structure and bonding. Due to this unusual but desirable combination of properties, MAX phases have attracted a lot of interest for various potential applications including high-temperature structural and energy applications, heat exchangers, electrical contacts as well as catalysis. They are also precursors for MXenes, a class of 2D materials formed when the A layers are selectively etched away, which has been a rapidly growing research field ever since their discovery in 2011 [57].

2.2.1 History

The history of MAX phases can be traced back to the 1960s, when Von Hans Nowotny and his colleagues synthesised and discovered more than 100 new carbides and nitrides [58]. Of these, about 30 phases were hexagonal complex carbides, which they named H-phases. The general structure of these phases was denoted by them as "T_2MC", i.e., they are similar to the 211 MAX phases. Here, T denoted a transition metal and M was another transition element or Group-A element. They noted that an important feature of these phases is that they consist of T_6C octahedral groups linked at the edges, shown in **Fig. 2.3**, while there is no bonding between the M atoms and C [59].

However, for decades after their discovery, the H-phases did not attract a lot of attention, and only a handful of studies on their synthesis and characterisation were made by Ivchenko *et al.* in the 1970s [60,61]. Similarly, there are also very few studies on 312 MAX phases in this period [62,63], and were limited by the fact that producing phase-pure compounds was a challenge using the existing methods.

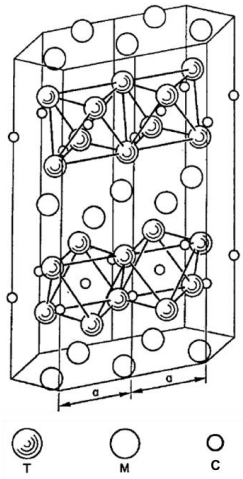

Fig. 2.3: Crystal structure of the H-phase discovered by Nowotny *et al.* [58].

The turning point in the history of MAX phases came in 1996 when Barsoum and El-Raghy used reactive hot pressing and successfully synthesised highly pure Ti_3SiC_2 samples that were fully densified [64]. The characterisation of this material led to the discovery of the noteworthy feature of MAX phases – the unique combination of properties such as machinability and thermal shock resistance with oxidation resistance and damage tolerance. This was followed by the synthesis and characterisation of related 211 MAX phases, which were also found to a show a similar combination of properties [65,66]. A few years later, the first 413 MAX phase, Ti_4AlN_3, was discovered [67]. With this discovery, it was soon realised that these materials constituted a wider family of compounds that have the general formula $M_{n+1}AX_n$. The name "MAX phases" (rather than $M_{n+1}AX_n$) was first popularised with the publication of a feature article by Barsoum and El-Raghy in the science and technology magazine *American Scientist* [68], and the name has stuck ever since.

2.2.2 Structure and bonding

MAX phases have hexagonal symmetry and belong to the $P6_3/mmc$ space group (number 194). Each unit cell contains two formula units. The unit cells of 211, 312 and 413 MAX phases are shown in **Fig. 2.4**. As mentioned earlier in the description of H-phases, the X atoms occupy the octahedral void formed by six M atoms, forming M_6X

octahedra that are linked at the edges. These octahedra are also present in binary MX compounds having the rock salt crystal structure. The A atoms, however, are found as single layers in between the linked M-X layers. The number n in $M_{n+1}AX_n$ represents the number of layers of M_6X octahedra in between successive layers of A atoms. The layered structure of MAX phases can also be clearly seen in high-resolution TEM images, such as in the HAADF-TEM image of Ti_3SiC_2 shown in **Fig. 2.5**. Note that the A layers act as mirror planes and the M-X layers are twinned with respect to each other.

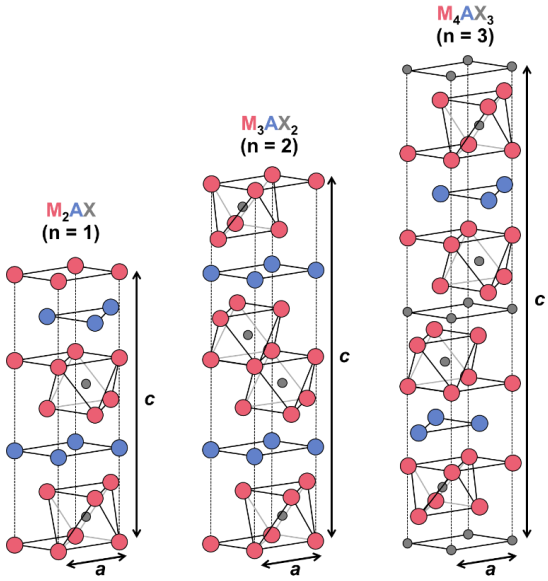

Fig. 2.4: Unit cells of $M_{n+1}AX_n$ phases for n = 1, 2 and 3 (adapted from [69]).

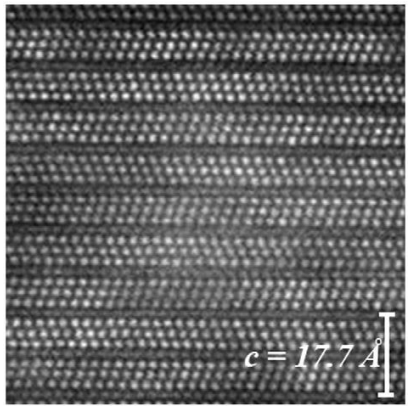

Fig. 2.5: HAADF-TEM image of Ti_3SiC_2 along the [11$\bar{2}$0] zone axis showing the characteristic 'zig-zag' pattern of layers in MAX phases [69].

The lattice parameter *a* of MAX phases is about 3 Å. However, the lattice parameter *c*, which is the height of the unit cell, is much larger, being ~13 Å for M_2AX, ~18 Å for M_3AX_2 and ~23-24 Å for M_4AX_3 phases, resulting in *c*/*a* ratios ranging from 4 to 8 [69]. Due to the highly anisotropic nature of the crystal structure, this also results in some anisotropicity in the properties of MAX phases, such as elastic constants, thermal expansion coefficients and conductivity [70,71].

A large number of DFT studies have been performed on MAX phases since the late 1990s [71–73], and it has been found that these materials have a combination of covalent, ionic and metallic bonding, similar in some aspects to the corresponding MX compounds. Like the MX binaries, the M and X atoms in MAX phases form strong covalent bonds due to strong interactions between the *d* orbitals of M atoms with the *s* and *p* orbitals of X atoms, and are in general even stronger than the M-X bonds in the binary phase [71]. Covalent bonding also occurs between M and A atoms, however, the interaction between the *d* and *p* orbitals in this case is relatively weaker than that of the M-X bonds. The ionic character of bonds in MAX phases is due to partial charge transfer from M atoms to A and X atoms, the magnitude of which depends on the electronegativity of the elements present. For example, in Ti-containing MAX phases, the charge transfer is estimated to be higher when the A-element is Si or Ge [71]. The strong covalent and ionic bonding results in properties typical of ceramics such as high melting point and stiffness. By changing the A and/or X-elements, the bond strengths can be modified, leading to the possibility of tuning the macroscopic properties of the material for specific applications.

Metallic dd_σ bonding occurs between adjacent M atoms and is the main contributor to the electronic density of states at the Fermi level ($N(E_F)$) in MAX phases. This parameter is an indication of the transport properties of the material, such as electrical and thermal conductivity. The $N(E_F)$ of MAX phases is large, even higher than that of some of the parent binary compounds [71], and explains why they are good conductors of heat and electricity. Thus, the combination of strong covalent and ionic bonds along with metallic bonding leads to MAX phases having desirable properties of both ceramics and metals.

2.2.3 Synthesis of MAX phases

The number of MAX phases successfully synthesised has been increasing at a rapid rate. As of 2024 [56], over 340 MAX phases have been synthesised, which is more than double the number reported in 2019 [74]. This includes ternary MAX phases, solid solution MAX phases and chemically ordered MAX phases such as *o*-MAX and *i*-MAX phases. Of the 124 ternary MAX phases discovered so far, the majority consists of M_2AX phases, followed by M_3AX_2 phases and M_4AX_3 phases. There are a handful of

synthesised MAX phases where $n > 3$, such as Ta_6AlC_5 and Ti_7SnC_6, however they have not been synthesised in the pure form and hence not characterised in detail. It must be noted that as the value of n increases, this also results in the properties of these phases getting closer to that of the corresponding binary MX compounds [74].

The synthesis of MAX phases can be broadly divided into two methods [56] – the bottom-up approach and top-down approach – which are described in the following sections.

2.2.3.1 Bottom-up synthesis

The bottom-up approach is the widely used method of synthesis – more than 85% of the currently known phases are bottom-up MAX phases. This approach involves direct synthesis routes where the desired MAX phase is obtained in one step. The most common method used is solid state reaction or solid-liquid state reaction, where the raw material consisting of a mixture of either pure elemental powders or a mix of elements and compounds is heated under an inert atmosphere. The temperature can range from 1000-1700 °C, and the time needed for the completion of the reaction can vary from a few hours [64] up to several days [75]. When no external pressure is applied, this is known as pressureless sintering, and results in the formation of a highly pure material, but can result in low densification in some cases. The porous material is usually then ball milled into a powder and can be densified using techniques such as hot pressing or field assisted sintering. These techniques can also be used directly on the raw starting material for simultaneous synthesis and densification [76]. Molten salt shielded synthesis has also been developed recently for the synthesis of MAX phases without the necessity of an inert atmosphere [77]. Other methods include self-propagating high-temperature synthesis and microwave-assisted synthesis [78].

MAX phases have also been synthesised in the form of thin films. This has mainly been done through physical vapour deposition methods such as cathodic arc deposition, pulsed laser deposition and magnetron sputtering [69,79]. The targets used can either be that of the pure elements or compounds. Chemical vapour deposition [80] and thermal spraying [81,82] have also been used to create MAX phase coatings, for applications such as bond coats for TBCs and nuclear fuel cladding.

2.2.3.2 Top-down synthesis

The top-down approach involves the modification of an existing MAX phase precursor synthesised using the bottom-up route. It is a relatively new approach – the first top-down ternary MAX phases were synthesised in 2017 [83]. Through this approach, the partial or complete replacement of A layers with elements from outside the Group-A elements became possible, leading to the expansion of the elements from which MAX phases could be formed. There are two ways by which this can be realised. One is the

molten salt replacement method where the A elements can be replaced by transition metals such as Mn, Fe, Co, Ni, Cu and Zn. This is carried out by the reaction of the MAX phase precursor with a transition metal halide such as $CuCl_2$ or $ZnCl_2$, for example [84,85]. The second method is the incorporation of noble metals such as Au or Ir in MAX phase thin films via a thermally induced exchange reaction. Here, a thick layer of the noble metal is deposited on the thin film and then annealed, which leads to the replacement of the original A-layers in the MAX phase with the noble metal [83,86].

2.2.4 Properties of MAX phases

Since the bonding in MAX phases is similar in many ways to that of MX binaries, they show several common physical properties such as good electrical and thermal conductivity, high stiffness, thermal stability and low coefficient of thermal expansion. The electrical resistivity of most MAX phases at room temperature ranges from 0.2-0.7 μΩm, and in some cases they are even better conductors than metals. For example, Ti_3SiC_2 and Ti_3AlC_2 show better conductivity than Ti [87]. They are also good thermal conductors, having conductivities in the range of 12-60 W/mK at room temperature. The average CTE of MAX phases lies in between that of non-oxide ceramics and metals [88]. Most have CTEs in the range of 8-10 μK^{-1}, with the notable exceptions being some Cr-containing phases which have CTEs between 12-14 μK^{-1} [87].

An interesting thing to note is that at elevated temperatures, MAX phases do not melt congruently but decompose peritectically into a solid $M_{n+1}X_n$ carbide or nitride and an A-rich liquid phase. Some MAX phases are very refractory materials, for example, Ti_3SiC_2 decomposes at temperatures above 2300 °C into TiC and a liquid phase [89]. However, they can decompose at lower temperatures in the presence of impurities [70].

MAX phases are quite stiff – the Young's modulus ranges from 170-370 GPa [90]. They also have relatively low densities, in the range of 4-6 g/cm^3, which is similar to that of many structural ceramics [88]. Due to the low density, the value of specific stiffness is also very high.

When considering the mechanical properties, MAX phases are significantly different from the MX compounds. Rather than being brittle and hard like ceramics, MAX phases are easily machinable, damage tolerant and resistant to thermal shock, which are properties associated more with metals. The machining of MAX phases occurs by the breaking off of microscopic flakes, akin to the shaving of ice [91], and not due to plastic deformation like in metals [70]. When MAX phases are exposed to some kind of damage, for example via Vickers indentations, the extent of damage is only limited to a small area around the indentations, and no crack propagation is seen. The energy

absorbing mechanisms include crack deflection, delamination, grain pull-out and kinking of grains [92]. Exposing MAX phases to thermal shock (by quenching for example) does not make them brittle but in some cases even increases the residual flexural strength [90].

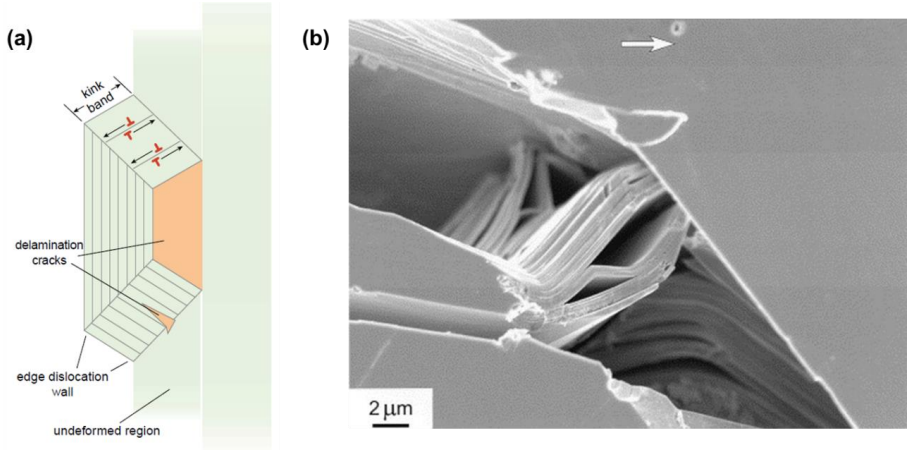

Fig. 2.6: Deformation micromechanisms in MAX phases: (a) a schematic showing the formation of kink bands [68] and (b) SEM image showing the formation of bridging ligaments within a crack in a fractured Ti_3SiC_2 sample, which restricts its propagation (the arrow indicates the direction of crack propagation) [93].

The stark difference in mechanical behaviour as compared to ceramics is due to the hexagonal, nano-layered structure of MAX phases, and the main deformation micromechanisms being the formation of kink bands (KBs) along with the formation of tenacious bridging ligaments, which restrict the propagation of cracks [68], as shown in **Fig. 2.6**. They typically show pseudo-ductile behaviour at high temperatures or constrained deformation, but can be brittle when thin and under tension, especially at lower temperatures. Hence, they are considered to lie in between metals and ceramics when it comes to mechanical properties [90].

2.2.5 MAX phases for high-temperature applications

Since MAX phases show favourable electrical, thermal and mechanical properties at high temperatures, they have attracted a lot of interest as potential candidates for high-temperature structural and energy applications. However, their ability to be used at high temperatures in the presence of air or other oxidising environments is more importantly determined by their oxidation and corrosion resistance.

The general reaction of MAX phases with oxygen is as follows:

$$M_{n+1}AX_n + bO_2 \rightarrow M_{n+1}O_x + AO_y + X_nO_{2b-x-y} \qquad \text{(Equation 2.14)}$$

As described in Section 2.1.5, good oxidation resistance can be achieved if a passivating oxide such as alumina, chromia or silica is formed. Hence, as a basic requirement, the M or A element should form one of these oxides. Additionally, it is important to consider the influence of the structure and bonding of MAX phases. Since the M-X layers are strongly bonded, they are stable at high temperatures, while the A atoms can diffuse more easily due to the weaker M-A bonds. Therefore, it is more likely that a stable oxide can be formed if the A element is responsible for forming the passivating oxide. Taking this into account, this narrows down the MAX phase compositions that could form a passivating oxide layer to those which have Al or Si as the A element.

Although Si-containing MAX phases show potential for high-temperature applications, the concentration of Si is not enough to form a pure layer of SiO_2 when oxidised. For example, the oxidation of Ti_3SiC_2 results in the formation of a duplex scale consisting of both SiO_2 and TiO_2, which becomes less protective at temperatures > 1000 °C [94]. It has been shown that the oxidation resistance of this MAX phase can be improved by forming a composite with SiC, which increases the amount of Si available to form a silica scale [95]. Despite the addition of SiC, a duplex scale is still formed, and is not protective at temperatures > 1200 °C.

Some Al-containing MAX phases, on the other hand, are able to form a dense, adherent and pure α-Al_2O_3 scale at temperatures up to 1400 °C. These alumina-forming MAX phases include Ti_2AlC, Ti_3AlC_2 and Cr_2AlC, which are considered to be some of the most oxidation resistant MAX phases in the temperature range of 900-1400 °C [26]. However, not all Al-containing MAX phases behave this way. Although V_2AlC, Ta_2AlC and Nb_2AlC contain Al, the formation of M-oxides as well as M-Al mixed oxides dominates and a protective alumina layer is not formed. Additionally, some of the oxides formed, especially in V_2AlC, have low melting points and tend to bleed away during oxidation [96]. This reduces the maximum temperature at which these MAX phases can be used to 600-900 °C. Hence, for high-temperature applications, i.e., at 1000 °C or higher, the MAX phases that show the most potential are the alumina-forming phases Ti_2AlC, Ti_3AlC_2 and Cr_2AlC.

Cr_2AlC forms a stable, protective alumina scale up to 1250 °C [97], while the Ti-containing phases Ti_2AlC and Ti_3AlC_2 are oxidation resistant up to higher temperatures. Ti_2AlC has been shown to form a 15 μm thick α-Al_2O_3 scale after thermal cycling tests at 1350 °C, which is adherent even after 8000 cycles [98]. The good adherence of the alumina scale is attributed to the close similarity in the CTE of the MAX phase with that of alumina. Ti_3AlC_2 also forms an adherent and slow-growing α-Al_2O_3 scale up to 1300 °C, while at higher temperatures the formation of the mixed oxide Al_2TiO_5 reduces the adherence of the scale [99].

Although a continuous alumina scale is formed in Ti_2AlC and Ti_3AlC_2, minor amounts of TiO_2 are also formed, as seen in **Fig. 2.7**, and are sometimes also present as nodules on the surface. The oxidation of Ti and subsequent formation of TiO_2 is found to occur more at lower temperatures, especially at 600 °C [100], and at the initial transient stage of oxidation. While this is normally not a point of concern, TiO_2 is a fast-growing oxide and as a result the oxidation behaviour of these phases is very sensitive to the Al content, presence of impurities such as TiC, as well as the surface finish of the material [101]. Al depletion in Ti_3AlC_2 results in accelerated or breakaway oxidation at 1100 °C [102]. Breakaway oxidation of Ti_2AlC occurs at 1200 °C when the mean surface roughness (R_a) is greater than 3 μm [103], which is also attributed to the increased growth of TiO_2.

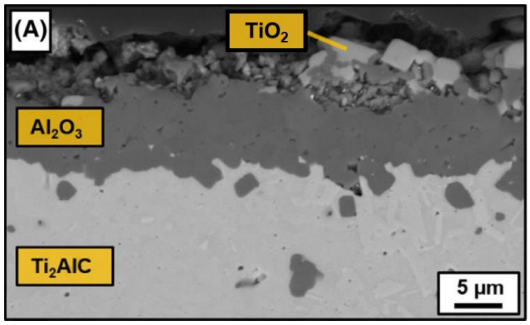

Fig. 2.7: Cross-section of oxide scale formed at 1200 °C on Ti_2AlC [88].

In contrast, the oxidation of Cr is very limited in Cr_2AlC. Even if oxidation does occur, it forms chromia which is also a passivating oxide. Hence, the oxidation behaviour of Cr_2AlC is not as sensitive as Ti_2AlC and Ti_3AlC_2 with respect to these factors, and is not known to show breakaway oxidation [104]. Due to the mismatch in CTEs of Cr_2AlC and alumina, delamination of the oxide scale sometimes occurs at temperatures ≥ 1150 °C [101], but a more recent study on highly pure samples has shown no delamination even after thermal cycling tests at 1200 °C [105]. Additionally, Cr_2AlC also shows better corrosion resistance in molten salts than the Ti-containing MAX phases [106,107], which is important for energy applications such as CSP where molten salts can be used as a heat transfer fluid (HTF). Due to its combination of excellent oxidation and corrosion resistance, Cr_2AlC is considered to be a promising MAX phase material for high-temperature applications in extreme environments.

2.2.6 Oxidation behaviour of Cr_2AlC

The oxidation behaviour of Cr_2AlC is unique among the alumina-forming MAX phases. Along with the formation of the protective α-Al_2O_3 layer, a porous chromium carbide layer is also formed below the oxide scale. The carbide formed in most cases is pure Cr_7C_3 [108,109] but a mixture of Cr_7C_3 and Cr_3C_2 has also been found to form in

some studies [97,110]. However, based on thermodynamic calculations, the formation of Cr_7C_3 is favoured over Cr_3C_2 [111]. The carbide is thought to form due to the depletion of Al during the formation of alumina and subsequent enrichment of Cr and C at the region below the oxide layer. Unlike in the Ti-containing phases Ti_2AlC and Ti_3AlC_2 which do not form a carbide during oxidation, it is believed that C does not diffuse out as fast as Al in Cr_2AlC, which leads to its accumulation at the oxide-MAX phase interface and could be the reason for the formation of carbide in this case. It is also believed that the oxide formed on Cr_2AlC is more impervious to C diffusion than that formed on Ti_2AlC [70]. **Fig. 2.8** shows the typical microstructure of the cross-section of the oxide scale formed in Cr_2AlC.

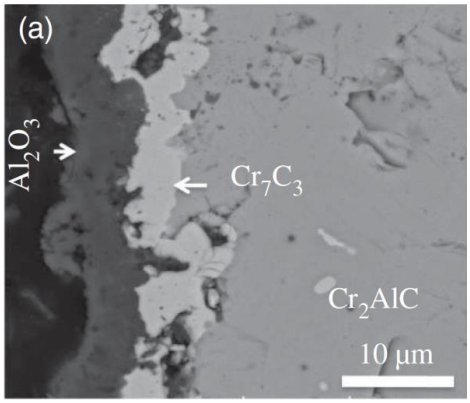

Fig. 2.8: Cross-section of oxide scale formed at 1200 °C on Cr_2AlC [26].

As mentioned earlier, the maximum temperature up to which Cr_2AlC shows good oxidation resistance is slightly less than that of the Ti-containing MAX phases. Lee *et al.* studied the long-term oxidation of Cr_2AlC at 1300 °C in air and showed that it cannot survive for a long time at this temperature, since the Cr_7C_3 layer starts to show excessive void formation and destroys the subscale region [112]. Tian *et al.* studied the oxidation up to 1250 °C, where they concluded that Cr_2AlC shows parabolic kinetics when oxidised at this temperature, and this seems to be the limit to which a passivating oxide layer can be formed without the complete deterioration of the carbide layer [97]. However, there is some debate about the oxidation kinetics shown by Cr_2AlC. While it was initially believed that Cr_2AlC primarily shows parabolic oxidation behaviour [108], it was later shown that the behaviour at temperatures greater than 800 °C is better described by cubic or even slower-than-cubic kinetics [26]. In either case, it is clear that the oxidation of Cr_2AlC is a diffusion-controlled process. It has been proposed that the growth of the scale is determined by the diffusion of oxygen via oxide GBs, similar to that of FeCrAl(X) alloys, and the continued growth of oxide grains over a long period of time can slow down diffusion and result in cubic kinetics since the available GB area for diffusion decreases [113].

A number of different factors can influence the oxidation behaviour of Cr_2AlC. The presence of undesired impurities or phases, in particular chromium carbides, is found to negatively affect the oxidation as the amount of impurities increases [114]. Some amount of alumina is also typically seen in as-sintered microstructures, but this is not expected to affect oxidation behaviour since it remains inert during oxidation. The grain size of Cr_2AlC is also believed to affect the formation of the oxide and carbide layer. Li *et al.* observed that a finer grain size leads to a faster oxidation rate [115]. It is assumed that Al preferentially diffuses via the grain boundaries in Cr_2AlC, so a finer grain size implies more GB diffusion paths, and this would lead to the faster diffusion and formation of the protective alumina scale. It was also observed in this study that the fine-grained Cr_2AlC samples only formed an alumina layer with no carbide layer below, which seems to be a case of anomalous behaviour and may not be directly related to the grain size.

Like some other properties of MAX phases, the oxidation resistance is also anisotropic in nature, and this effect is more pronounced in textured or single crystal samples. In textured Ti_2AlC and Ti_3AlC_2, the oxidation behaviour has been shown to be markedly anisotropic. Due to the layered structure of MAX phases, Al can rapidly diffuse in the direction parallel to the basal planes, which results in the formation of a thicker oxide on the surface perpendicular to the basal planes [116]. A similar effect has been seen in the oxidation of single crystal Cr_2AlC, where the oxide is thicker on the surface of the crystal perpendicular to the basal planes [111].

The effect of water vapour on oxidation behaviour is also important to consider, especially for high-temperature applications where the material is exposed to steam or the atmosphere, which naturally contains some amount of humidity. So far, most of the oxidation studies done on Cr_2AlC have been carried out under controlled conditions, mostly in a dry, synthetic air atmosphere, but there are a handful of studies done on Cr_2AlC under more realistic conditions. The performance of Cr_2AlC under a burner rig loading with thermal cycling at 1200 °C has been studied, and it is shown that even after 500 cycles in these aggressive conditions, the oxidation resistance is excellent, with no spallation or cracks [105]. Recently, a study on the high-temperature oxidation behaviour of Cr_2AlC under controlled humidity conditions has also been performed, where the effect of gas volatilization on the oxidation mechanism is examined [117]. It is shown through thermodynamic calculations that the volatilization of species is significantly higher in wet air than dry air, and it is primarily that of the chromium carbide rather than the alumina layer.

2.2.7 Open questions

One of the most attractive characteristics of MAX phases is the possibility to tune their properties by modifying their chemistry while retaining the crystal structure. While some macroscopic properties such as stiffness, conductivity and magnetism are directly related to bond strengths and chemistry, other properties such as oxidation resistance may be more difficult to tune since it depends on multiple factors. However, since the nature of the A-element as well as its competition with the oxidation of the M-element seem to be some of the important factors determining oxidation behaviour, efforts have been made to modify the oxidation resistance by partially replacing some of the A atoms with another element. For example, partially replacing Al atoms with Si in Cr_2AlC thin films to form the solid solution MAX phase $Cr_2Al_{1-x}Si_xC$ has been shown to increase the thickness of the alumina layer formed when up to 0.7 at.% of Si is added [118].

Since the addition of reactive elements such as Y in alumina formers is known to enhance the oxidation resistance, a few attempts have also been made to dope Cr_2AlC with Y. The addition of up to 0.2 at.% of Y as a dopant to Cr_2AlC coatings has been shown to improve the oxidation resistance at temperatures up to 1200 °C, however the addition of a slightly higher amount (0.3 at.%) of Y degrades the oxidation performance [119]. It is proposed that the reduction in oxidation rate is due to the slowing down of bulk Al diffusion from the MAX phase by Y atoms. On the other hand, the direct incorporation of 16.7 at.% Y in Cr_2AlC to form the *i*-MAX phase $(Cr_{2/3}Y_{1/3})_2AlC$ resulted in the formation of an orthorhombic crystal structure and also forms a duplex oxide scale consisting of chromia and $Y_3Al_5O_{12}$ (YAG) [120]. Efforts have also been made to synthesise metastable $(Cr,Y)_2AlC$ MAX phase solid solutions [121]. While the addition of Y to improve oxidation resistance shows some promise, the mechanism is not fully understood yet, and also necessitates a deeper understanding of the oxidation mechanism of pure Cr_2AlC to examine the possibility of improving oxidation resistance with reactive element additions.

It has also been observed that the published results on the oxidation behaviour of Cr_2AlC occasionally show some inconsistencies. For example, when comparing the mass gain curves for Cr_2AlC oxidised at 1200 °C under similar conditions, including the data obtained from this work, it is observed that the rate of growth is different in the three cases shown here, in **Fig. 2.9**(a). Additionally, some uncommon oxide scale microstructures have also been reported, such as the absence of carbide formation, as seen in **Fig. 2.9**(b), and the formation of a mixed Al-Cr oxide surrounded by alumina, shown in **Fig. 2.9**(c).

In order to understand the possible reasons for better or worse oxidation performance under similar conditions, as well as the formation of different oxidation products, it is important to know the mechanism of oxidation and the important factors controlling the rate of oxidation. This requires the analysis of diffusion pathways such as GBs and interfaces, as well as a careful analysis of the presence of impurities that could cause unexplained behaviour, which has not been performed so far.

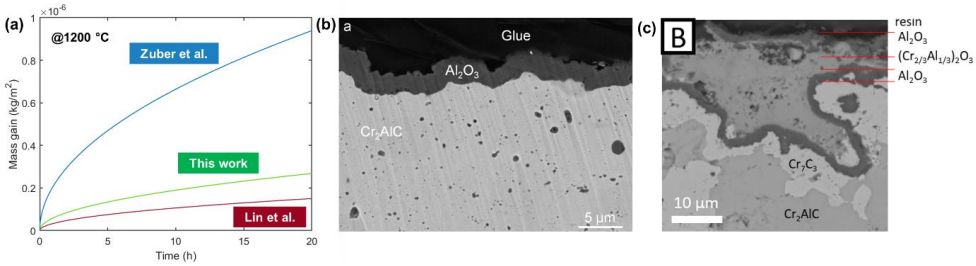

Fig. 2.9: Inconsistencies in the reported oxidation behavior of Cr_2AlC: (a) Mass gain curves at 1200 °C in humid air/atmosphere obtained from [117] (blue) and [108] (red), as compared to the data obtained in this work (green), (b) oxide scale microstructure showing no formation of carbide layer [115] and (c) oxide scale showing the formation of a mixed Al-Cr oxide [117].

2.3 Self-passivating tungsten alloys

2.3.1 Tungsten – properties and applications

The refractory element tungsten (W) has the highest melting point (3422 °C) among metals and the second highest among all elements, second only to carbon (C) which sublimes at 3825 °C [122]. α-tungsten is the most common allotrope and has a body-centered cubic structure belonging to space group Im3m (number 229). It is one of the densest elements, having a density of 19.3 g/cm^3, similar to that of gold. It also has high thermal conductivity coefficient of 1.75 Wcm^{-1}K^{-1} at room temperature, which makes it suitable for use as a heat sink material [123]. Additionally, the coefficient of thermal expansion is low, being in the range of 4.32-4.68 µK^{-1} at room temperature, which makes it possible to use with ceramics for high-temperature applications [123]. The combination of these properties makes tungsten an attractive high-temperature material.

Although polycrystalline tungsten shows good mechanical properties at elevated temperatures, such as high strength, yield point and creep resistance, it is brittle at lower temperatures. The temperature at which the transition between the ductile and brittle behavior occurs is known as the ductile-to-brittle transition temperature (DBTT). The DBTT is sensitive to the microstructure as well as the presence of

impurities. Cold worked microstructures, such as that of rolled sheets, foils and extruded wires, show a lower DBTT. On the other hand, annealing increases the DBTT due to the coarsening of grains [123]. However, the workability of tungsten can be improved with certain alloying additions such as Re, which also has the added benefit of increasing the strength of tungsten at high temperatures. The addition of thoria (ThO_2) particles to tungsten also increases its strength via the dispersion-strengthening mechanism and additionally enhances the thermionic emission of tungsten by lowering the work function [123].

Tungsten and its alloys have been used in various applications such as filaments in incandescent light bulbs, as a non-consumable electrode in gas tungsten arc welding (GTAW), thermionic electron emission guns, heating elements, thermocouples as well as certain aerospace applications, to name a few. However, one of the major factors that limits its use for high-temperature applications is its reactivity with oxygen. Tungsten starts to oxidize in air at a temperature of 400 °C, with the rate of oxidation increasing rapidly above 700 °C. It does not form a protective oxide scale and additionally, the oxide formed (WO_3) sublimates significantly at temperatures above 900 °C, which results in catastrophic oxidation. Tungsten and its oxide can also react with water vapor at elevated temperatures, forming volatile tungsten oxide hydrate ($WO_2(OH)_2$) [27]. Hence, an inert atmosphere or vacuum is necessary when using tungsten at high temperatures to prevent its oxidation, which places restrictions on its potential applications.

2.3.2 Tungsten for nuclear fusion applications

Tungsten is a prime candidate for use as a plasma-facing armor material of the first wall in a future fusion reactor. Due to its high melting point and high thermal conductivity, it is one of the few materials that can handle the high heat loads expected during operation. Being a heavy metal, it is also resistant to erosion under plasma operation. Tungsten also has a low hydrogen retention, which is beneficial since the fuel for the fusion reaction consists of the hydrogen isotopes D and T. The combination of these properties makes W a suitable material for the first wall armor [16,124].

However, the oxidation behavior of tungsten is an important point to consider, especially in the context of safety. This is not a point of concern during regular plasma operation since the system is under vacuum and the expected temperature range of the first wall is 550 to 730 °C (considering the DEMOnstration power plant) [125]. The production of neutrons from the fusion reaction can cause neutron irradiation of the first wall, thus activating W. In case of an accident scenario, for example in a loss-of-coolant accident (LOCA), modelling studies have shown that the temperature of the vacuum vessel can rise up to ~1000 °C in the initial days, and to a maximum of 1450 K

or 1177 °C after 20-40 days [126]. These high temperatures combined with the ingress of air can result in the oxidation of the activated tungsten in the first wall, resulting in the formation and sublimation of radioactive WO_3. Hundreds of kilograms of radioactive WO_3 could be released into the environment per week [127], which can create hazardous conditions in and around the power plant in the aftermath of an accident. Hence, preventing the oxidation of tungsten in case of an accident is a crucial factor that needs to be taken into account so that the safety of the fusion power plant can be ensured.

2.3.3 Self-passivating W-based alloys

Due to the catastrophic oxidation behavior of W at high temperatures, a few efforts have been made in the past to create tungsten alloys that are more resistant to oxidation and expand its use to applications in oxidizing environments. Attempts to improve the oxidation resistance of W up to 1200 °C as well as at ultra-high temperatures (1600-3000 °C) with the addition of elements such as Ta, Zr and Th and oxide dispersions such as Al_2O_3 and MgO were made in the 1960s [128,129]. An alternate approach being explored at this time was the use of high-temperature oxidation resistant coatings, such as WSi_2 and high-melting oxides, on W and W alloys [130]. However, this was a challenging task. At the same time, refractory alloys based on elements other than W were also being developed and showed better oxidation resistance, which possibly led to a dwindling interest in trying to fabricate oxidation-resistant W alloys.

But in recent decades, with the increased focus on fusion research, the quest to improve the safety of a fusion reactor having the first wall made of tungsten led to a renewed interest in oxidation resistant tungsten alloys. The main approach has been to alloy W with elements which could form a passivating oxide layer and suppress the formation of WO_3. Since Al, Cr and Si are the elements that can form passivating oxide scales when added to alloys, as described in Section 2.1.5, some of the first attempts to improve the oxidation resistance were to fabricate binary alloys of W with these elements and study their oxidation behavior. The various binary and ternary alloys based on these systems that have been developed and studied so far are described below.

2.3.3.1 W-Al alloys

Al has limited solubility in W (≤ 2.6 at.%) and also forms a range of intermetallic phases such as WAl_4, WAl_5 and WAl_{12} [131]. Nevertheless, W-Al alloys have been fabricated via non-equilibrium alloying methods such as magnetron sputtering [132] and mechanical alloying [133], presumed to consist of a combination of metastable phases.

One study has shown that the solubility of Al in W can be increased to more than 50% through mechanical alloying of W and Al powders [133].

However, studies on the oxidation resistance of these alloys are very limited. Binary W-Al thin films were fabricated using magnetron sputtering and their oxidation performance at 1000 °C was tested. It was found that the addition of 12.1 wt.% Al to W showed the best oxidation resistance, having a parabolic oxidation constant (k_P) of 11.3×10^{-6} $mg^2cm^{-4}s^{-1}$ [134]. Adding the reactive element Y to this system to improve the oxidation resistance was also attempted, however, compositions with < 1 wt.% Y could not be produced. The W-Al-Y thin films synthesized showed much worse oxidation behavior than the binary alloy, possibly due to over-doping of Y [134].

Although Al-containing alloys cannot be used for fusion reactor applications, since Al can transmute into radioactive products with a long half-life [124], W-Al alloys could be developed for other high-temperature applications such as CSP receivers.

2.3.3.2 W-Si alloys

The W-Si system is similar in some ways to the W-Al system. Si has a slightly higher solubility – W can dissolve a maximum of 5.5 at.% Si – and also forms a few intermetallic phases, of which the silicides WSi_2 and W_5Si_3 are stable [135].

Binary W-Si thin films, containing up to 18 wt.% Si, were developed in 2007 by Koch and Bolt, where it was shown that the oxidation rate decreased with increasing Si content. With 18 wt.% Si, the linear oxidation rate (k_l) of the thin film sample at 1000 °C was 1.3×10^{-3} $mgcm^{-2}s^{-1}$, which is an order of magnitude less than that of a pure W thin film oxidized at the same temperature [17]. Bulk W-Si samples with 32 at.% Si have been prepared using FAST/SPS by Liu *et al.*, which also shows an 18-fold decrease in oxidation rate compared to bulk tungsten when oxidized at 1000 °C. However, sintering results in the formation of a microstructure consisting of W_5Si_3 and silica particles in a tungsten-rich matrix [136].

The oxidation resistance of W-Si thin films was further improved with the addition of 10 wt.% Cr and making thicker coatings. The k_l of a 4.6 μm thick W-10Si-10Cr (wt.%) was 1.9×10^{-6} $mgcm^{-2}s^{-1}$, which is three orders of magnitude less than that of a 1.5 μm thick W-18Si sample [17]. It was concluded that the formation of a thin outer chromia scale along with silica below led to the decreased rate of oxidation. Recently, Y-containing bulk W-Si alloys have also been prepared. The alloy with composition W-6.7Si-3.8Y (wt.%) shows a much lower amount of mass gain after oxidation compared to the binary alloy, and maintains its shape after up to 80 h of oxidation at 1000 °C. The oxide scale formed is complex, consisting of a mix of silica, WO_3, yttria, Yi-Si-O and W-Y-O particles in different parts of the scale [137].

As mentioned earlier, brittle tungsten silicides are formed during the fabrication of bulk W-Si alloys via sintering. While their presence has not been found to degrade the oxidation performance, these intermetallic phases do degrade the workability of W [138]. Therefore, although ternary W-Si alloys show promising results with respect to oxidation behavior, they have a disadvantage when considering the mechanical properties, especially for bulk alloys.

2.3.3.3 W-Cr alloys

Unlike the W-Al and W-Si systems where many intermetallic phases are formed, W and Cr form a binary isomorphous system. Both W and Cr have a body-centered cubic (bcc) structure. Cr is fully soluble in W above 1677 °C, forming a continuous solid solution, which also has a bcc structure. Below this temperature, a miscibility gap is present, where the phase separation into a Cr-rich solid solution ((αCr, W) or α1) and W-rich solid solution ((αW, Cr) or α2) can occur, as seen in the phase diagram shown in **Fig. 2.10**.

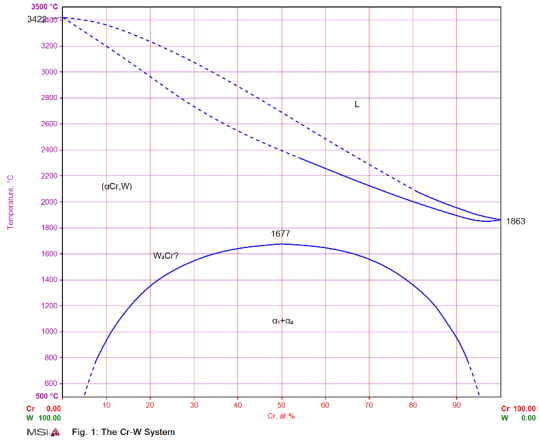

Fig. 2.10: W-Cr binary phase diagram showing that it forms an isomorphous system with the presence of a miscibility gap below 1677 °C [139].

Both binary W-Cr alloys and ternary alloys with the addition of elements such as Nb, Ti, Y and Zr have been studied. Binary W-Cr alloys prepared by sintering mechanically alloyed powder were first studied by Telu *et al.*, where they found that the best oxidation behavior was shown by the alloy with the composition $W_{0.5}Cr_{0.5}$, and the oxide scale formed consisted mainly of Cr_2WO_6, WO_3 and some amount of Cr_2O_3 [140]. They also studied the effect of Nb addition to the binary alloys, and showed that the rate of oxidation is reduced as compared to the binary, but the oxide scale primarily consists of Cr_2WO_6 and $Nb_2O_5{\cdot}3WO_3$, with no formation of chromia [141].

Koch *et al.* studied W-14Cr-2Ti and W-18Cr-2Ti thin films and showed that the oxidation performance was drastically improved compared to W-Si-Cr thin films

[138]. A study of bulk W-12Cr-2.5Ti alloys revealed that the oxide scale formed consists of an outer thin chromia layer, with layers of Cr_2WO_6, Ti_2CrO_5 and WO_3 below [142]. Koch *et al.* had also studied a yttrium-containing alloy of composition W-7Y-3Cr (wt.%) in the same study, which showed relatively slow oxidation but performed worse than the W-Cr-Ti alloys [138]. The worse oxidation performance despite the addition of the reactive element Y is possibly due to the relatively low amount of Cr and over-doping of Y, which can have a negative effect.

A systematic study of W-Cr-Y thin films of various compositions was performed by Wegener *et al.*, where the ideal composition for the best oxidation resistance in the presence of the reactive element Y was obtained with the addition of ~12 wt.% Cr and 0.6 wt.% Y [127]. A dense chromia layer is formed, with no formation of mixed oxide or WO_3, as shown in **Fig. 2.11**. Studies of the oxidation performance of W-Cr-Y as compared to W-Cr-Ti alloys have shown that the Y-containing alloys show the lowest mass gain, both as thin films [143] and bulk alloys [144]. The addition of yttria to W-Cr has also shown a similar beneficial effect on oxidation performance when compared to the binary alloy [145]. Zr has also been used as a reactive element in W-Cr alloys, and it has been determined that the ideal Zr:Cr ratio for improvement in oxidation resistance is in the range of 5-10% [146]. Studies of quaternary alloys containing both Y and Zr showed that the addition of Zr results in a very slight decrease in the oxidation rate, but does not seem to impact the oxide scale thickness and microstructure as compared to the W-Cr-Y alloy [147].

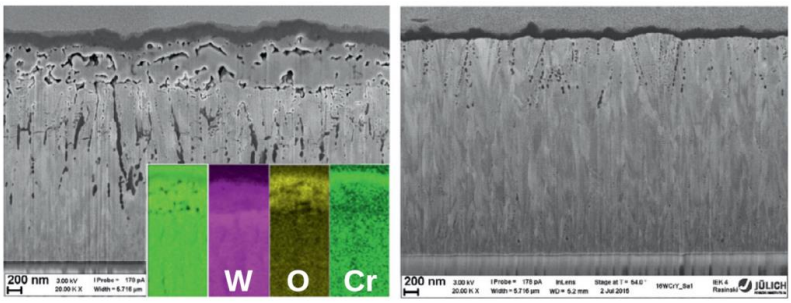

Fig. 2.11: Oxidised microstructure of thin films of (a) W-Cr and (b) W-Cr-Y [127].

2.3.4 Oxidation behaviour of W-Cr-Y

The W-Cr-Y alloys being researched and developed at Forschungszentrum Jülich are also known by the acronym SMART, which stands for "Self-passivating Metal Alloys with Reduced Thermo-oxidation" [148]. A unique aspect of using a W-based alloy containing elements lighter than W, such as Cr and Y, especially in light of fusion reactor applications, is that during regular plasma operation in a fusion reactor, these

lighter elements get preferentially sputtered away, leaving almost pure tungsten as the plasma facing surface. Hence, this still retains the beneficial aspects of using a pure W first wall. In case of a LOCA, as described in Section 2.3.2, the alloying elements in the bulk of the alloy are able to form a passivating oxide layer, preventing the oxidation of W and sublimation of its oxide. This enables these alloys to behave like pure W during plasma operation and as a self-passivating alloy under accidental conditions when oxidation can occur, as summarized in **Fig. 2.12**.

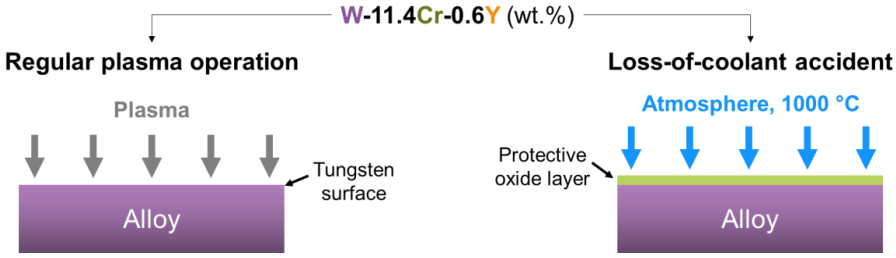

Fig. 2.12: Unique property of SMART materials for fusion reactor applications: like pure W under plasma operation but can form a passivating oxide layer under oxidation-prone conditions.

The first experiments to determine the optimum composition of the W-Cr-Y alloy for best oxidation performance were performed using thin films produced via magnetron sputtering. It was determined that ~12 wt.% Cr and 0.6 wt.% Y were necessary to form a passivating chromia layer on W-Cr-Y thin films [127]. However, since thin films do not have a large enough reservoir of Cr to sustain the formation of chromia over longer oxidation times, bulk W-Cr-Y alloys were also synthesized by sintering mechanically alloyed powder [44], which also showed the formation of a passivating chromia scale, as seen in **Fig. 2.13**. While hot isostatic pressing (HIP) or pressureless sintering has been used by some research groups for compaction of these alloys [145,149], it was shown that FAST/SPS can be a better alternative to these methods since it reduces the sintering time from several hours to a few minutes and also allows for better control of grain size and microstructure [44].

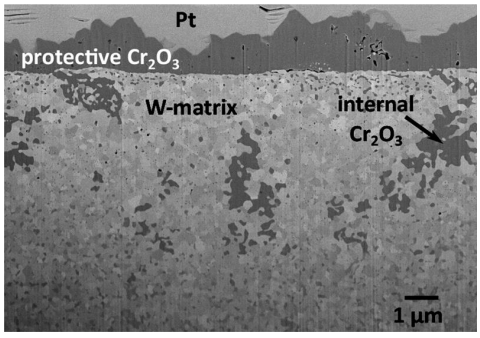

Fig. 2.13: Cross-section of oxide scale formed on W-11.4Cr-0.6Y after oxidation at 1000 °C for 44 h in Ar-20%O_2 [150].

The ideal grain size for good oxidation resistance of bulk W-Cr-Y alloys was determined to be ~200 nm [44]. Studies on the effect of varying Y concentration on bulk alloys have shown that the ideal grain size and Y distribution for good oxidation performance could only be obtained when 0.6 wt.% Y is added, as shown in **Fig. 2.14**, and therefore it was confirmed that W-11.4Cr-0.6Y was the best composition for bulk alloys as well [150].

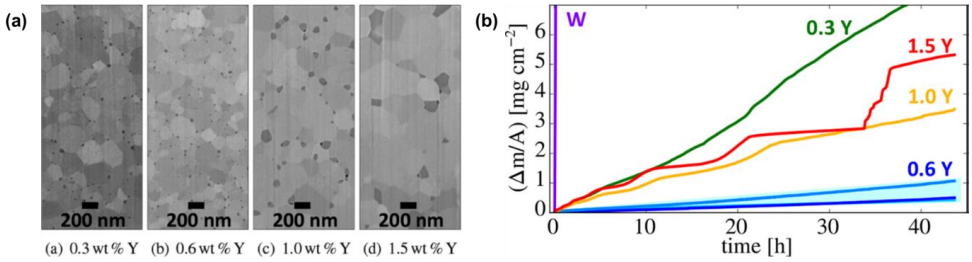

Fig. 2.14: Effect of varying Y concentration of W-11.4-xY alloys: (a) as-sintered microstructure and (b) oxidation rate [150]. Both over-doping and under-doping negatively impact the oxidation resistance.

Along with oxidation studies, the rate of sublimation of these alloys under humid air was also extensively studied using a dedicated setup in the thermogravimetric analyzer (TGA). While a passivating chromia layer is also formed under humid oxidation, it was shown that the sublimation of the oxide formed on W-Cr-Y was more than an order of magnitude less than that of tungsten oxide at 1000 °C. The main contribution to sublimation of the alloy was determined to be the volatilization of chromia [28]. It was also shown that under a humid atmosphere, the formation of W-containing oxides was suppressed. It was proposed that the presence of free H from water plays a role in suppressing the oxidation of W, since the Gibbs free energy for the formation of H_2O is more negative than that of WO_3 [28].

2.3.5 Open questions

In binary W-Cr alloys, the presence of Cr alone is not enough to create a fully passivating chromia scale – the addition of the reactive element Y is essential to improve the oxidation resistance and enable the formation of a chromia layer. However, the mechanisms for how and why Y acts in bulk W-based alloys to improve the oxidation behavior is not clear yet.

The reactive element effect has been extensively studied for Y in many other chromia-forming materials such as Ni-Cr, Fe-Cr and Co-Cr based alloys [151–155]. Several mechanisms have been proposed, the most significant of them being the effect of Y segregation at chromia grain boundaries (GBs), which can affect the diffusion of the cations (Cr ions) as well as anions (O ions) involved in the formation of the oxide scale. It has been shown that the oxide growth direction changes from the outward direction

to the inward direction with the addition of Y, which is more beneficial since it reduces the possibility of void formation at the oxide-alloy interface, hence increasing the adherence of the oxide to the substrate [49]. Other proposed mechanisms include the binding of undesirable impurities such as S due to the high affinity of Y for these elements, and the formation of "pegs" or intrusions at the oxide-alloy interface that could strengthen this interface [45].

In W-based alloys, studies of the Y effect are very limited. Studies comparing bulk W-Cr and W-Cr-Y alloys produced by hot isostatic pressing (HIP) have been performed, but the amount of Cr is different for the binary and ternary alloys [144,149], which makes it less straightforward to determine the effect of Y alone. Additionally, although the oxidation rates were compared, the oxide scale microstructures with and without Y were not analyzed. A direct comparison of the effect of Y addition on the oxidation rate and oxide scale microstructure has been done on W-Cr thin films [127], where it is seen that Y addition results in the formation of a continuous chromia layer and less porous oxide scale. However, for bulk alloys, a comprehensive study of the effect of Y addition on the different aspects of oxidation behaviour, such as the oxidation rate, surface and cross-sectional oxide scale microstructure, and the overall morphology has not been performed yet.

An ^{18}O tracer study has also been performed on W-Cr-Y thin films using a three-step oxidation experiment followed by measurement of ^{18}O depth profiles using secondary ion mass spectrometry (SIMS), where it was concluded that the oxide growth in the presence of Y is in the outward direction [156]. However, this goes against the general mechanism by which Y acts in other chromia formers, since Y addition is largely found to result in inward growth of the oxide scale, which is beneficial for scale adherence. Hence, it is worth performing such a study again to verify the oxide growth direction, and could benefit from the use of additional techniques to identify the isotopes without ambiguity. It is also worth mentioning that thin films have a different microstructure as compared to bulk alloys, as well as a limited supply of Cr and Y due to the limited volume of material, and hence cannot accurately represent the oxidation behavior of bulk alloys.

Chapter 3 Objectives

In this work, two potential materials for high-temperature applications – the MAX phase Cr_2AlC and the self-passivating W-based alloy W-11.4Cr-0.6Y – are studied. There are several key differences between the oxidation properties and open questions with respect to these two materials: Cr_2AlC forms a passivating alumina scale, while W-Cr-Y forms a chromia scale with the help of the reactive element Y.

The primary objective of this thesis is to use nanoscale analysis methods, particularly atom probe tomography, to unveil the oxidation mechanism of the MAX phase Cr_2AlC, as well as understand the mechanism by which the addition of the reactive element Y improves the oxidation resistance of W-Cr-Y.

In particular, for the MAX phase, this involves the following:

- Determining the oxidation kinetics for the oxidation of Cr_2AlC at 1000 °C and 1200 °C, along with a detailed microstructural characterisation of the oxide scale.
- The analysis of the local chemistry of possible diffusion pathways for O and Al ions, which includes GBs of alumina, carbide and Cr_2AlC, as well as interfaces between these phases. The three-dimensional compositional information at the nanoscale is obtained using APT, and can help determine which diffusion processes control the rate of oxide growth.
- Investigating the possible effects of the presence of impurities on the oxidation process.

For the W-based alloy, this involves the following:

- Studying the effect of Y addition on the oxidation behaviour of bulk W-Cr alloys. This involves comparing the behaviour of the alloys W-11.4Cr and W-11.4Cr-0.6Y, which only differ by the addition of 0.6 wt.% Y, based on various aspects of oxidation resistance, such as oxidation rate, overall morphology of the oxide scale and microstructure, so that the beneficial effects of Y can be qualitatively determined.
- Determining the mechanism of the reactive element effect of Y on this alloy system. For this purpose a two-step oxidation experiment is performed using ^{18}O as a tracer on both the binary and ternary alloys, in combination with APT analysis of the oxide scale formed on the ternary alloy.

By gaining a better understanding of the oxidation mechanisms in these materials and identifying the important factors controlling the rate of oxidation and the microstructure formed during oxidation, this can give insights into ways to further improve the performance of these materials.

Chapter 4 Experimental Methods

This chapter describes the various experimental methods used for the synthesis of the materials studied, the setups used for oxidizing the samples, and lastly the techniques employed for micro- and nano-structural characterization and analysis of the materials before and after oxidation.

4.1 Material synthesis and preparation

4.1.1 Mechanical alloying

Mechanical alloying involves the high-energy ball milling of a mixture of elemental powders. Through the process of repeated cold welding, fracturing and re-welding of powder particles, alloying at the atomic level can be achieved. This makes it possible to synthesize non-equilibrium phases such as nanocrystalline materials, supersaturated solid solutions and amorphous alloys like bulk metallic glasses, to name a few [157,158]. While it was first used to synthesize an oxide dispersion strengthened (ODS) Ni-based superalloy [159], today this technique is used to synthesize a wide variety of materials, especially for materials where alloying is difficult to achieve through conventional methods.

Planetary ball mills are commonly used for mechanical alloying. The elemental powder mixture is poured into jars along with a specific amount of milling balls, usually made of dense, hard materials such as stainless steel, tungsten carbide (WC) or zirconia (ZrO_2). Process control agents (PCA) such as ethanol and toluene are sometimes added to prevent excessive welding of the powders to the milling media. The jars are then rotated at a specific speed until alloying is achieved. Ball milling can cause the powder to heat up, since some of the impact energy is dissipated as heat. In order to prevent the oxidation of the powder under these conditions, milling is done under an inert atmosphere such as argon. It is important to note that milling for too long can result in the uptake of impurities such as Fe, C or Zr from the milling media used and should be avoided. The various parameters such as the material of the jars and balls, ball-to-powder ratio, rotational speed and time of milling are optimized to ensure complete alloying while minimizing the level of impurities.

4.1.2 Field-assisted sintering

Field-assisted sintering technique (FAST), also known as spark plasma sintering (SPS), is a synthesis technique in which the material in the form of powder is consolidated under the application of pressure and high temperature via current-induced heating, to get a fully densified material. The typical setup used for FAST/SPS is shown in **Fig.**

4.1. The compacted powder of the material to be sintered is placed within electrically conductive dies (made of graphite for example), and uniaxial pressure is applied on both ends using a loading system. At the same time, a current is produced by the application of a voltage to the external circuit, and this generates heat within the sample via Joule heating (if the sample is conductive), and no external source of heat is needed. The temperature is monitored using a thermocouple or pyrometer. Very high heating and cooling rates can be achieved since the generation of heat depends on the current and not on external heating elements. The highest heating rates are up to 1000 °C/min, and temperatures up to 2400 °C can be reached [160].

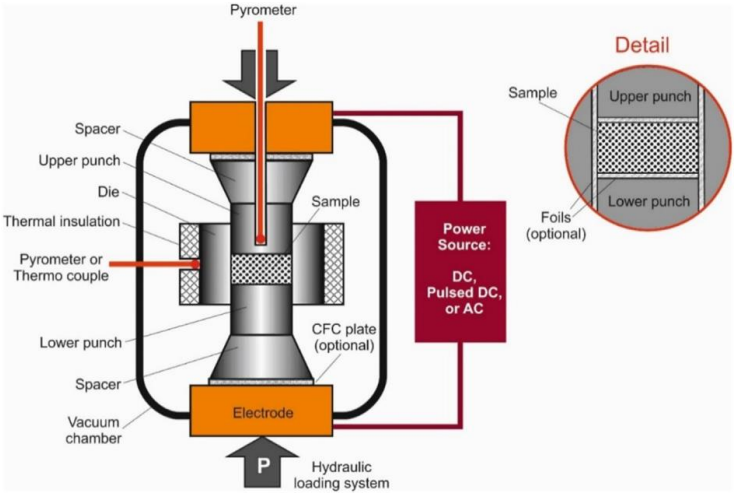

Fig. 4.1: Basic schematic of the setup used for FAST/SPS [161].

Due to the high heating rates and simultaneous application of pressure, the densification process is relatively quick (typically a few minutes), as compared to other densification techniques such as hot isostatic pressing (HIP), which may take several hours. Therefore, this technique causes minimal grain growth, which can be useful for the synthesis of nano-grained materials. By varying the pressure and current, the amount of grain growth and precipitation of secondary phases can also be controlled, which makes this an effective technique for synthesizing materials with the desired microstructure.

The details of the procedure and parameters used for the synthesis of the MAX phase Cr_2AlC and the alloy W-Cr-Y are described in detail in Sections 5.2 and 6.2 respectively.

4.1.3 Cutting of samples for oxidation tests

After sintering, the material is in the form of pellets of diameter 20 mm. Samples for oxidation studies were cut from the sintered pellets using a diamond wire saw or

electrical discharge machining (EDM). For thermogravimetric analysis, the samples were cut into cuboidal shape of dimensions approximately 5 × 4.5 × 3 mm, so that the total surface area of the sample is approximately 1 cm^2. For the oxidation done in a tube furnace for the ^{18}O isotope tracer experiment, flat samples of dimensions 10 × 10 × 1 mm were used. The samples in all cases were ground to a 1200 grit surface finish using abrasive SiC grinding sheets. Following this step the MAX phase samples were also polished with diamond paste of particle sizes 3 μm and 1 μm.

4.2 Oxidation tests

4.2.1 Thermogravimetric analysis (TGA)

Thermogravimetric analysis (TGA) is used to measure the amount of mass gained by a sample during oxidation as a function of time, at the desired temperature and under a specific atmosphere. The mass gain is a measure of the amount of oxide that is formed on the sample, which indicates the extent to which the oxidation reaction has taken place, and hence this allows us to study the rate of growth of the oxide scale. The mass gain curve can be fit to a general power law equation like Equation 2.8, through which the kinetics of oxide scale formation can be determined. The plot can also indicate signs of spallation (sharp decrease in mass gain), breakaway oxidation (rapid increase in mass gain, often following linear kinetics) or sublimation of volatile species (slow decrease in mass gain over time, if the rate of sublimation is faster than the rate of oxidation).

Oxidation experiments were performed using the thermogravimetric analyser TAG-16/18 from Setaram [162], which is a symmetrical analyser, i.e., it consists of two identical furnace chambers with a symmetrical gas flow arrangement, as shown schematically in **Fig. 4.2**. The sample to be oxidised is placed in the furnace chamber on the right, inside an alumina crucible hung from the microbalance using thin steel and Pt rods. The furnace chamber on the left consists of an identical setup, where a reference sample, usually made of an inert material like alumina, of the same geometry and dimensions of the sample to be oxidized is placed and hung from the other end of the microbalance. Counterweights are added to a small pan in the microbalance chamber, usually on the lighter reference sample side, to balance the mass before the experiment is started. The symmetrical arrangement ensures that the gas flow on both sides is identical, and hence helps to counteract buoyancy effects. The configuration of the components is also made to ensure that turbulent flow near the sample is reduced. Cylindrical graphite resistor furnaces are used in this device, with an operating temperature range of 20 °C to 1700 °C. Tubular alumina shields form the inner wall

and act as an insulator, and the graphite resistor is protected from oxidation by enveloping it with argon gas during operation.

A high sensitivity electromagnetic-optical balance is used, which works on the principle of the null position [163]. At the null position, an equal amount of light is shone on photodiodes placed on either side of the balance. When there is mass gain, the balance moves out of the null position, which results in an unequal amount of light on the photodiodes. A compensation current is applied, which acts as a restoring force to bring it back to the null position. The amount of current applied is proportional to the mass gain, which is calibrated and recorded in the data acquisition system.

The TGA setup is connected to a humidifier WETSYS from Setaram [162], which can be used to add a controlled amount of water vapour to the gas used for oxidation, which enables us to perform oxidation tests in humid air. The gas temperature range is from 20 °C to 80 °C and the relative humidity (RH) range is from 5-80% RH at 50 °C.

Fig. 4.2: Cross-sectional schematic of a symmetrical TGA setup, showing the microbalance on top with two identical furnace chambers below, one for the reference sample and one for the sample to be oxidized [164].

The MAX phase samples were isothermally oxidized at temperatures of 1000 and 1200 °C in synthetic air with 70% relative humidity (at 25 °C). They were heated at a rate of 10 K/min in argon atmosphere, with two slower ramps of 5 K/min and 2 K/min used in the end to not overshoot the set temperature, following which the humid synthetic air was introduced. At each temperature one short oxidation test for 40 min was performed to study the microstructure after the initial stage of oxidation. Long

oxidation tests were performed for 48 h at 1000 °C and for 20 h at 1200 °C. After the exposure was completed, the heating chambers were flushed with argon and cooled in three temperature ramps of 40 K/min, 20 K/min and 10 K/min. For the W-Cr and W-Cr-Y samples, the same procedure was followed, but oxidation was done only at 1000 °C for 20 h, in synthetic air with 70% relative humidity at 25 °C.

4.2.2 ^{18}O isotope tracer experiment

A horizontal resistance-heated tube furnace was used to perform two-step oxidation experiments using ^{18}O as a tracer on W-Cr and W-Cr-Y samples. The furnace has an integrated air-tight silica tube, long enough to have well-defined hot and cold zones. The gas flow and composition is controlled using two mass flow controllers (MFC) and a pressure gauge. For the tracer experiment, oxidation is done in two stages. Before starting the experiment, the samples are placed in a long boat-shaped alumina crucible in the cold zone of the furnace. In the first stage, after evacuation, a mixture of Ar-20%$^{16}O_2$ was introduced into the furnace and heated to 1000 °C, after which the samples were moved from the cold to hot zone, and kept there for 4 h. While the samples are still inside, the furnace was evacuated again and then filled with a gas mixture of Ar-20%$^{18}O_2$. The purity of $^{18}O_2$ gas used here is 97%. The samples are oxidized in this atmosphere for another 4 h, and then moved to the cold zone and allowed to cool down.

4.3 Material characterization

4.3.1 Surface roughness

Using profilometry, a two-dimensional trace of the surface topography of a sample is obtained through contact with a moving stylus, which enables one to calculate parameters such as the surface roughness, waviness and curvature. The surface roughness of the samples before oxidation was measured using the Dektak 6M profilometer from Bruker to account for the possible effects of polishing quality on the oxidation behaviour. This device has a maximum scanning length of 3 cm, a height range of 10 nm to 655 μm, and a vertical resolution of 10 nm. The scan length used to calculate the roughness of the cuboidal samples was 2 mm. Each roughness measurement was repeated five times at different locations on the samples, and the final result was taken as the average of these measurements.

4.3.2 Density

According to Archimedes' principle, the upward buoyant force acting on a body immersed in a fluid is equal to the weight of the displaced fluid. The buoyant force is

the difference in weight of the body in air (W_{air}) and when immersed in a fluid (W_{fluid}). When this quantity is divided by the density of the fluid (ρ_{fluid}), the volume of the body is obtained. Through this method, the volume of a sample can be accurately calculated, following which the density can be determined by dividing the weight of the sample by the calculated volume. Hence, the following formula for the calculation of density ρ based on Archimedes' principle is obtained:

$$\rho = \left(\frac{W_{air}}{W_{air} - W_{fluid}}\right)\rho_{fluid} \qquad \text{(Equation 4. 1)}$$

A Sartorius Cubis laboratory balance, along with the included density determination kit, was used to measure the density according to this principle. The fluid used for the measurement is high purity ethanol.

4.3.3 X-ray diffraction (XRD)

X-ray diffraction (XRD) is a commonly used characterisation technique to identify the different phases present in a sample, based on the diffraction pattern generated. The setup consists of an X-ray tube, sample holder and X-ray detector. The X-ray tube is used to generate characteristic X-ray radiation. Cu Kα radiation with a wavelength of 1.54 Å is typically used. When these X-rays hit the sample, they are diffracted by the crystalline phases present. The angle at which it is diffracted (θ) depends on the phase and crystal orientation, and is given by Bragg condition:

$$n\lambda = 2d\ sin\theta \qquad \text{(Equation 4. 2)}$$

Here n denotes the order of diffraction, d is the lattice spacing and λ is the wavelength of the X-ray. The diffracted X-rays are then detected by the X-ray detector. Most X-ray diffractometers use the Bragg-Brentano arrangement [165]. The incident beam from the X-ray source is usually kept fixed, while the sample holder and detector are rotated (by the specified range of θ and 2θ, respectively) to change the incident angle. Alternatively, the sample holder can be fixed while the source and detector are rotated by $-\theta$ and θ respectively. The diffraction pattern generated is a fingerprint of the phase.

XRD was used to determine the phases present in the as-sintered samples, as well as the phases formed after oxidation. XRD was performed using the D8 Discover and the D4 Endeavor from Bruker AXS GmbH, using Cu Kα radiation, with a step size of 0.02° and 2 s as the time per step.

4.3.4 Focused ion beam – scanning electron microscope (FIB-SEM)

Scanning electron microscopy (SEM) is used to image samples by using a focused beam of electrons that scans the surface of the specimen. Since it has a large depth of

field, the images appear three-dimensional, and is useful for microstructural characterisation and to study surface morphology. In a scanning electron microscope with focused ion beam (FIB-SEM), in addition to the electron beam column there is a focused ion beam (FIB) column at a specific angle to the electron beam column. The schematic of a FIB-SEM is shown in **Fig. 4.3**. The FIB column contains a liquid metal ion source (LMIS), which produces a focused beam of ions, typically Ga^+. Plasma FIBs or PFIBs use plasma ion sources, where a beam of ionised noble gas such as Xe or Ar is produced. The ion beam can be used to mill the sample to investigate the cross-section or to prepare lamellae or needles from the sample for TEM or APT analysis, for example.

FIB-SEMs are also usually equipped with a gas injection system (GIS), which can be used to deposit layers of materials such as Pt, W and C, as well as a manipulator. The deposition of Pt on the surface is commonly used to protect the top layer of the sample during ion milling. The sample is mounted on a 5-axis stage, i.e., it can be moved in X, Y and Z-directions, as well as rotated and tilted. The combination of a FIB and SEM in one instrument makes it more convenient to use the functions of both the ion and electron beam, which makes this an indispensable tool for both sample preparation and characterisation.

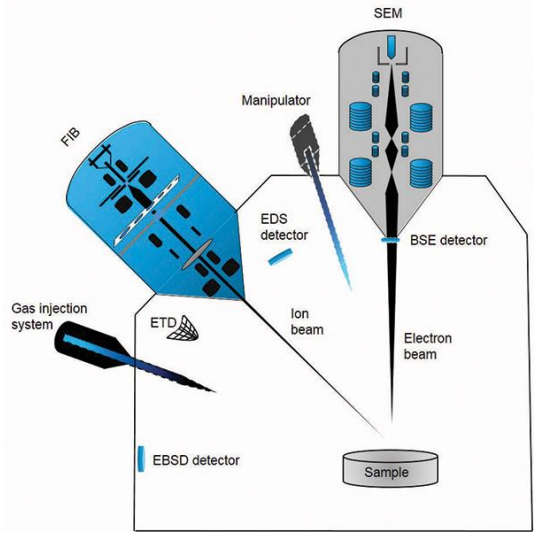

Fig. 4.3: Schematic of a FIB-SEM with various detectors, GIS and manipulator [166].

The surface and cross-sectional microstructure of the samples before and after oxidation was characterized using the ZEISS Crossbeam XB 540 FIB-SEM manufactured by Carl Zeiss Microscopy GmbH, where the FIB was used to mill the cross-section of the oxide layer and the SEM was used to image the microstructure.

The average thicknesses of different layers in the oxidized microstructure were calculated as the mean of ten measurements across a cross-section.

4.3.5 Transmission electron microscopy (TEM)

Transmission electron microscopy (TEM) uses a high-energy electron beam transmitted through a thin section of the material (generally < 150 nm thick) to produce a high-magnification image. The schematic of the instrumentation used in a TEM is shown in **Fig. 4.4**. TEM has a higher spatial resolution as compared to SEM, and is hence used to characterize the nanostructural features of the material, such as grain boundaries and presence of nano-sized precipitates. However, since it uses electrons transmitted through the material for imaging, the image produced is a two-dimensional projection of the sample.

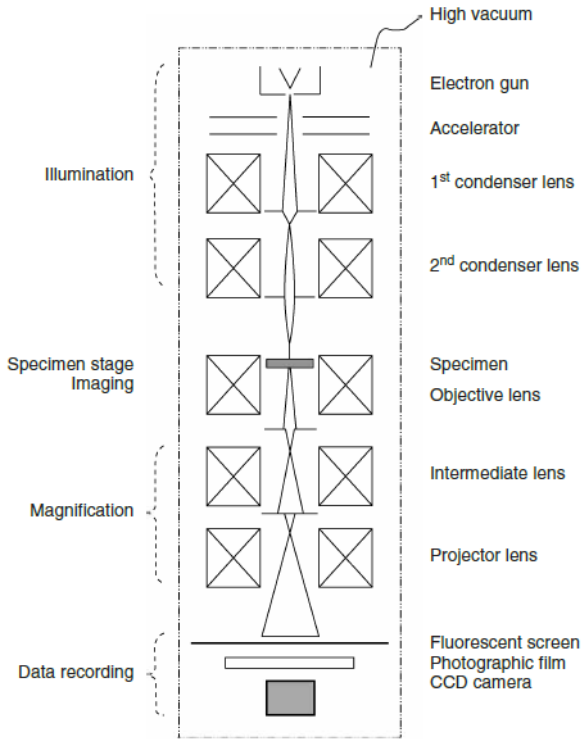

Fig. 4.4: Instrumentation of a transmission electron microscope [167].

TEM characterization of the oxidised MAX phase samples was done on a lamella of thickness close to 100 nm prepared from the bulk sample using a Helios NanoLab 460 F1 dual-beam FIB-SEM equipped with Ga^+ ion source. A step-by-step procedure for preparing a damage-free lamella can be found elsewhere [168]. High-angle annular dark-field (HAADF) STEM imaging was performed using an FEI Titan G2 80–200

ChemiSTEM microscope at 200 kV, equipped with a high-brightness field-emission gun and a probe Cs corrector [169]. The convergence semi-angle for STEM imaging was 25 mrad, and the collection semi-angle was 80-200 mrad.

4.3.6 Energy-dispersive X-ray spectroscopy (EDX)

When a material is exposed to a high-energy beam, which is able to kick electrons off inner shells of atoms, outer shell electrons fill these vacant spots and result in the emission of characteristic X-rays. The X-rays produced can be used to identify the elements present, and this technique is known as X-ray spectroscopy. When the characteristic X-rays are identified based on their energy, this is known as energy-dispersive X-ray spectroscopy (EDX). In electron microscopes, this technique can be used to determine the composition of specific region of interest by exposing the area to the primary electron beam and identifying the distribution and quantity of elements present through the characteristic X-rays generated in the process. An EDX detector such as a silicon drift detector (SDD) is used to collect the X-ray photons and generate an EDX spectrum, which can be used for elemental analysis.

Along with microstructural analysis of the Cr_2AlC and W-Cr-Y samples, a corresponding elemental analysis was performed in the ZEISS Crossbeam XB 540 FIB-SEM tool using an EDX detector from Oxford Instruments, using an accelerating voltage of 12 kV. EDX chemical mappings were also obtained using the FEI Titan G2 80–200 ChemiSTEM microscope which is equipped with a super-X energy-dispersive X-ray spectroscopy system.

4.3.7 Atom probe tomography (APT)

Atom probe tomography (APT) is three-dimensional characterisation technique that provides compositional information with sub-nanometre spatial resolution, i.e., at the atomic scale. The first steps in the development of this technique were taken in 1935 with the invention of the field emission electron microscope by Edwin Müller. The first 1D atom probe was invented by Müller, Panitz, and McLane in 1967 at the Pennsylvania State University [170], followed 21 years later by the first 3D instrument developed by Cerezo, Godfrey, and Smith in 1988 [171]. With the development of the local electrode atom probe (LEAP) in 1993, along with advancements in FIB-based specimen preparation techniques, APT became more accessible and started to be applied to a wide array of materials [172].

The basic principle of APT, which originates from field ion microscopy, is the field evaporation of specimen atoms in the form of ions under a high voltage. This requires the creation of intense electrostatic fields in the range of 10-50 V/nm, for which the

specimen must be needle-shaped with a very sharp tip [173]. The sharper the tip, the stronger is the electrostatic field generated when it is exposed to a high voltage.

Single sharp-tipped specimens can be prepared by electrochemical polishing of a wire-shaped sample. However, it is difficult to prepare specimens from specific regions of the microstructure using this method. With the development of the FIB-SEM, it became possible to prepare multiple site-specific needle-shaped specimens from a sample at once, the standard procedure for which is shown in **Fig. 4.5**. A wedge in the form of a triangular prism, typically 15-20 μm long and 2 μm thick, is milled from the sample surface using the FIB. The wedge is attached to the micromanipulator using the in-situ gas injection system, which can deposit a material like Pt at a specific region. The wedge is cut free from the sample, lifted out and attached to a support. A micro-tip coupon made of Si is commonly used, which contains an array of circular posts where slices of the wedge can be mounted. After mounting part of the wedge to a micro-tip post, this part is then cut. This step is repeated on the remaining part of the wedge until no more material is left. Lastly, each of these mounted pieces of the wedge is shaped into needle-like specimens using a series of annular milling patterns in the FIB. A final low-kV clean-up is performed to refine the shape of the tip and to remove the Ga contamination caused due to the higher ion beam voltage used during annular milling [174].

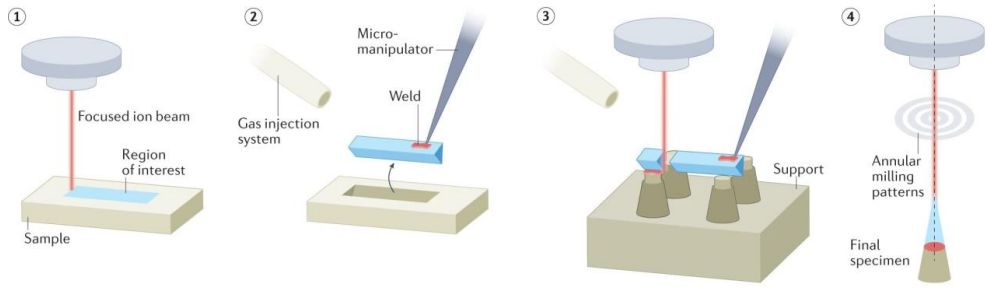

Fig. 4.5: Standard procedure for the preparation of APT specimens using a FIB-SEM [173].

To measure a sample in an atom probe, a single needle-shaped specimen or micro-tip coupon is placed inside an ultra-high vacuum (UHV) chamber (10^{-10} to 10^{-11} mbar pressure) at cryogenic temperatures (20-80 K), as shown in **Fig. 4.6**. In front of the tip is a counter electrode, which is connected to a high-voltage DC power supply, and can apply voltages of up to 15 kV. In a LEAP, the counter electrode is called a local electrode, which is located much closer to the specimen tip, usually a few tens of microns away, which helps us select a specific specimen to measure when a micro-tip coupon is used. When a voltage is applied, this ensures that only the chosen tip undergoes field evaporation. The close proximity of the local electrode has the added advantage of reducing the voltage required to produce the electric field for field

evaporation to occur [175]. The field evaporation of specimen atoms is triggered either by a voltage pulse, which varies the electric field, or a laser pulse, which varies the specimen temperature. The latter is a better method for the measurement of non-conductive specimens such as oxides and carbides in the atom probe [176]. At the other end is a position-sensitive delay-line detector, where the trajectory of the evaporated ions ends. The impact position is used to determine the x-y coordinates of the ions, while the z-coordinate is determined based on the evaporation sequence [177,178]. The time of flight of the ion is used to calculate the mass-to-charge ratio (M), using a formula derived by equating the potential and kinetic energies of the evaporated ion:

$$M = \frac{m}{n} = 2eV\left(\frac{t_{flight}}{L_{flight}}\right)^2 \qquad \text{(Equation 4. 3)}$$

Here, m is the mass of the ion, n is the charge state of the ion, e is the elementary charge of the electron, V is the voltage applied, t_{flight} is the time of flight, and L_{flight} is the flight distance. A histogram of M for the detected ions gives us a mass spectrum, based on which the chemical identity of the ions can be determined.

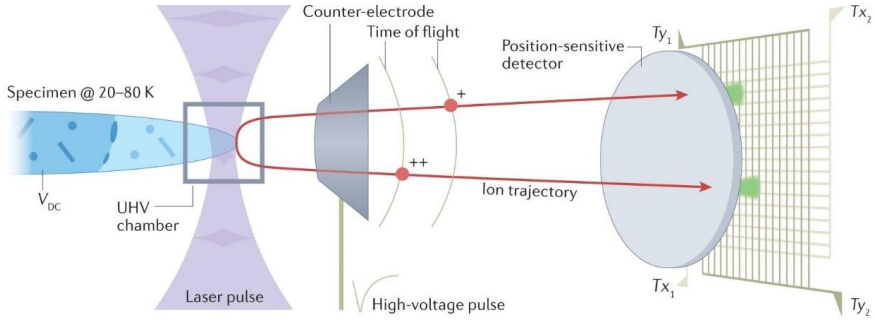

Fig. 4.6: Schematic showing the instrumentation inside the analysis chamber of a straight flight-path atom probe [173].

Using APT, it is possible to detect all elements with equal sensitivity, including distinguishing between isotopes, as well as provide compositional information at the atomic level, with sub-nanometre spatial resolution and a detection limit of ~10 ppm [179]. Additionally, structures such as grain boundaries and phase distribution can be visualised in 3D. This makes it a powerful characterisation tool for the chemical analysis of features at the nanoscale, such as the segregation of elements at GBs and interfaces and the identification of precipitates. With the development and use of the pulsed laser to trigger field evaporation, it became possible to study non-conductive materials like oxides and carbides using this technique, which was earlier restricted to only conductive metals and alloys. APT has since been used to study bulk oxides as well as oxide scales formed on various materials [180–184]. The growth of a passivating oxide scale is a diffusion-controlled process, typically through oxide GBs,

and oxide adherence is determined by the strength of interfaces. With the additional chemical information gleaned from APT studies of GBs and interfaces, it was possible to understand the role played by segregating elements at these regions, which helped explain oxidation mechanisms, such as the reactive element effect.

Specimens for APT studies were prepared using a Helios NanoLab 600i dual-beam FIB (Thermo Fischer Scientific, Waltham, MA, USA) from various regions of interest using conventional as well as backside liftout methods [185]. Six to seven specimens were prepared from each liftout. The APT analysis was performed using a local electrode atom probe, LEAP 4000X HR from Cameca Instruments, in pulsed laser mode. Laser pulses of 355 nm wavelength, 12 ps pulse length, 40-50 pJ pulse energy, and 250 kHz frequency were used. The base temperature of the samples was kept at ~50 K and the detection rate was set to 0.005 ions per pulse. Data reconstruction and analysis was performed using the Integrated Visualization and Analysis Software (IVAS) version 3.6.18.

Chapter 5 Oxidation Mechanism of Cr_2AlC

5.1 Introduction

In this chapter, the study of the oxidation behaviour of the MAX phase Cr_2AlC in a humid atmosphere at temperatures of 1000 °C and 1200 °C is described. The analysis of the micro- and nanoscopic mechanisms and ionic transport during the early stage of the steady-state oxidation is the main focus. Various characterisation techniques such as XRD, FIB-SEM, EDX and TEM are used to analyse the microstructure of the oxide scale. Additionally, a comprehensive APT study, including the optimisation of APT parameters for this material, is performed. The local chemistry of important diffusion pathways such as GBs and interfaces and the influence of impurities or other segregating elements in these regions is examined. Based on these observations, a mechanism for the oxidation of Cr_2AlC is proposed.

5.2 Synthesis of Cr_2AlC

The material studied in this work was synthesized by solid-liquid state reaction to form pure Cr_2AlC, followed by densification by field-assisted sintering technique/spark plasma sintering (FAST/SPS), resulting in high density and purity [76]. Cr_2AlC synthesized using this method has been previously demonstrated to show good long-term oxidation behaviour even under aggressive conditions during exposure using a burner rig [105]. The detailed process is described below.

Chromium (average particle size, APS <10 μm, 99.2% pure), aluminium (APS 7-15 μm, 99.5% pure) and graphite (APS 7-11 μm, 99.0% pure) powders (all from Alfa Aesar, Germany), were mixed in the ratio 2.0:1.1:1.0 by hand and filled in an Al_2O_3 crucible. An excess of 10 at.% Al was added to compensate for the Al loss during heating due to its low melting point. The crucible containing the mixture was covered with porous titanium sheets, which act as an oxygen getter, heated at a rate of 5 K/min to 1350 °C, and kept at this temperature for 3 h in an oven under argon atmosphere. This results in formation of a Cr_2AlC brick through the solid-liquid state reaction, details can be found elsewhere [76]. An image of the formed brick of Cr_2AlC is shown in **Fig. 5.1**.

Since the brick is not fully densified, it was then broken into smaller pieces and wet milled with ethanol in a planetary ball mill (PM400, Retsch, Germany) for 3 h at 250 rpm to obtain powder. ZrO_2 milling balls of 5 mm diameter were used, and the inner walls of the milling jar were made of Al_2O_3. To consolidate the powder, the field-assisted sintering technique/spark plasma sintering (FAST/SPS) facility (FCT-HPD5, FCT Systeme GmbH, Germany) was used. 6 grams of the Cr_2AlC powder were poured into a standard graphite tool of 20 mm inner diameter, followed by heating up at a rate

of 100 K/min up to 1200 °C in vacuum and holding for 10 min at this temperature, while a uniaxial pressure of 50 MPa was applied. The sintered pellet is a cylinder of 20 mm diameter and approximately 4 mm height with a density of 5.12 g/cm^3 measured using the Archimedes principle.

Fig. 5.1: Brick of pure Cr_2AlC obtained after solid-liquid state reaction (Image courtesy: Melina Poll).

Cuboidal samples for oxidation studies were cut from the sintered pellets using a diamond wire saw. The dimensions are approximately 5 × 4.5 × 3 mm, so that the total surface area of the sample is approximately 1 cm^2. **Fig. 5.2** shows such a sample of Cr_2AlC, which looks shiny and reflective like a metal after grinding and polishing.

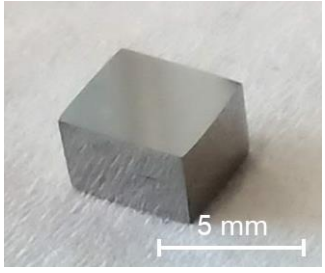

Fig. 5.2: Image of a cuboidal sample cut from a sintered pellet of Cr_2AlC, ground and polished.

5.3 Microstructure of as-sintered Cr_2AlC

Fig. 5.3 shows the surface and cross-sectional microstructure of as-sintered Cr_2AlC. The microstructure consists of a Cr_2AlC matrix in which particles of alumina (dark grey phase) and a few particles of chromium carbide (light grey phase) are present.

The alumina particles are found in varying sizes: while a majority of them are hundreds of nm big or even smaller, a few very large particles that are several μm large are also present. The volume fraction of alumina is about 1.6%, calculated based on image analysis. Assuming that the rest of the sample is pure Cr_2AlC, the theoretical density of the sample would be 5.21 g/cm^3. Since the measured density of the sample is 5.12 g/cm^3, the relative density of the sample is 98.3%, which is a good densification value for bulk MAX phases [76]. Some amount of porosity is also present, which can

be seen in the low-magnification surface image **Fig. 5.3**(a), and aligns with the measured value of the relative density.

EDX maps, shown in **Fig. 5.4**, also show the presence of Zr-containing particles in some regions, which possibly originate from the ZrO_2 balls used in the milling process. The XRD pattern of the as-sintered Cr_2AlC, shown in **Fig. 5.5** confirms the presence of small quantities of α-Al_2O_3, while chromium carbide and Zr-containing phases were not detected in the diffraction pattern due to their low content.

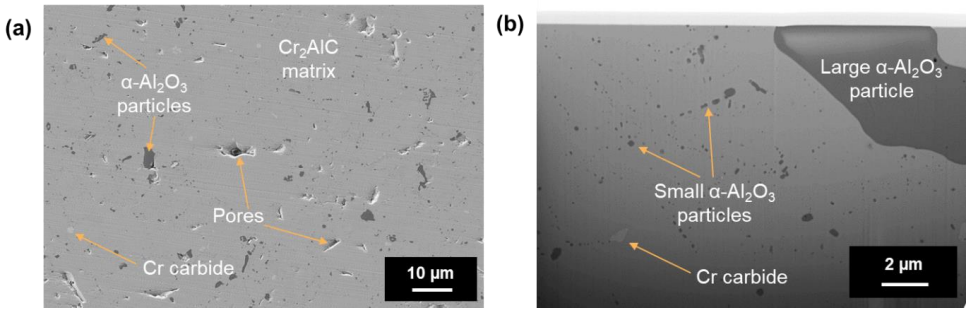

Fig. 5.3: SEM images of (a) surface and (b) cross-section of as-sintered Cr_2AlC. Both small and large alumina particles are present in the Cr_2AlC matrix, along with a few small chromium carbide particles.

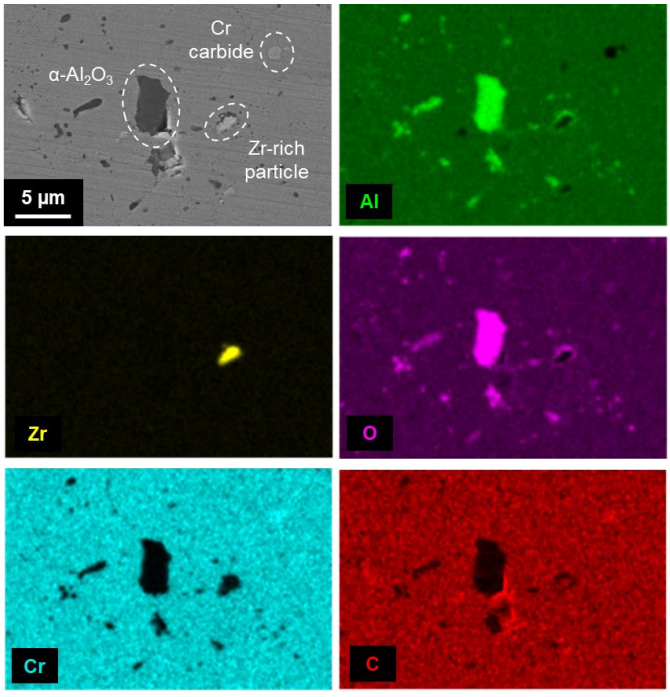

Fig. 5.4: EDX maps of the as-sintered Cr_2AlC sample surface showing the presence of alumina, chromium carbide and Zr-rich particles.

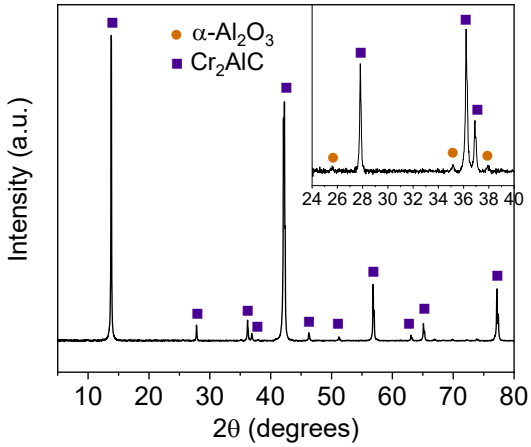

Fig. 5.5: XRD pattern of the as-sintered Cr_2AlC sample confirming the presence of α-Al_2O_3. The inset shows an enlarged view of the 2θ range 24-40° where α-Al_2O_3 peaks can be seen.

5.4 Oxidation behaviour and kinetics

The Cr_2AlC samples were oxidised at 1000 °C for 40 min and 48 h, and at 1200 °C for 40 min and 20 h, in a synthetic air atmosphere with 70% relative humidity at 25 °C. **Fig. 5.7** shows the plots of the thermogravimetric analysis obtained from the isothermal oxidation at both these temperatures. After 20 h the mass gain at 1200 °C is ~0.8 mg/cm², whereas it amounts to only ~0.1 mg/cm² when oxidizing at 1000 °C.

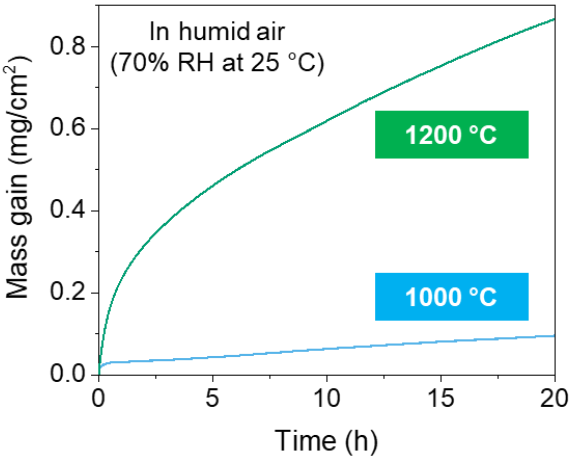

Fig. 5.6: TGA mass gain curves of the Cr_2AlC samples oxidized at 1000 °C and 1200 °C.

To study the oxidation kinetics, the data was fit to a power law equation, as described in Section 2.1.3.1, of the general form

$$\Delta m = k \cdot t^n \qquad \text{(Equation 5. 1)}$$

Here Δm is the mass gain per unit area in mg/cm^2 and t is time in seconds. The scale growth exponent n determines the type of the oxidation kinetics. Although the surface roughness of all samples before oxidation is similar, with an R_a value of around 10 nm as measured by the profilometric analysis, some surface defects like grooves near the sample edges could lead to initial differences in mass gain, but these will not influence the long-term oxidation behaviour. Nevertheless, these initial differences can alter the value of the exponent when trying to fit the data to a power law equation, especially for short oxidation times, so only the part of the curves beyond the first five hours were fitted. In their critical review of oxidation kinetics shown by MAX phases, Tallman *et al.* suggested that up to the first ~10 h could be omitted when fitting the data to the power law equation [26].

The values of the exponent and the accuracy of fitting (R^2 values) are summarized in **Table 5.1**. When the value of n is 0.5, this is equivalent to parabolic kinetics. Here, the value of n at both temperatures is around 0.5, which indicates that it shows parabolic behaviour at both temperatures for the time range studied in this work. The data was also fitted to parabolic and cubic kinetics equations. Based on the R^2 values, the data fits better to the parabolic equation, which again demonstrates a better agreement to parabolic behaviour.

Table 5.1: Fitting of the oxidation kinetics exponent n and the accuracy parameter R^2

Equation	$\Delta m = k \cdot t^n$ **(power law)**		$\Delta m = k \cdot t^{1/2}$ **(parabolic)**	$\Delta m = k \cdot t^{1/3}$ **(cubic)**
Parameter	n	R^2	R^2	R^2
1000 °C	0.59	0.9994	0.9818	0.8399
1200 °C	0.47	0.9989	0.9949	0.9221

Additionally, the analysis of the instantaneous apparent parabolic rate constant over time $k_p(t)$ was performed. The rate constant was calculated according to the following equation:

$$(\Delta m)^2 = k_p \cdot t \qquad \text{(Equation 5. 2)}$$

The calculation was performed based on the procedure described by Quadakkers *et al.* [25], where a plot of $(\Delta m)^2$ vs t is made and the instantaneous slope of this plot at each point gives the value of $k_p(t)$. The k_p values obtained are then plotted as a function of time. At 1200 °C, as seen in **Fig. 5.7**(a), it can be observed that after the first 2.5 h, $k_p(t)$

becomes almost constant, at a value of around 1×10^{-5} $mg^2cm^{-4}s^{-1}$, which indicates that the oxide growth indeed shows parabolic kinetics at the steady state of oxidation. It can therefore be concluded that the oxidation rate is controlled by ionic diffusion through the oxide scale, and hence it is important to study the potential diffusion paths. From **Fig. 5.7**(b), which shows only the first one hour of the plot, it is seen that the transient oxidation lasts ~20 min, after which a protective oxide layer is formed, resulting in the decrease in the oxidation rate constant until it reaches a steady value equal to the parabolic rate constant. A similar plot was also made for the $k_p(t)$ at 1000 °C, shown in **Fig. 5.8**, where the value becomes constant at around 1.5×10^{-7} $mg^2cm^{-4}s^{-1}$ after the first 8 h.

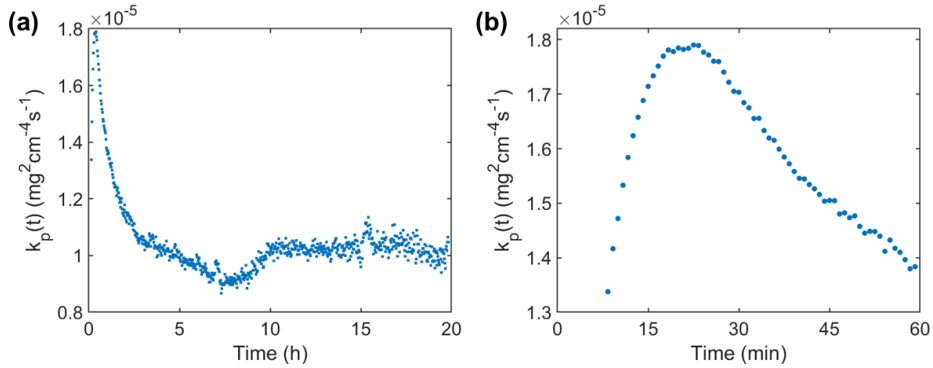

Fig. 5.7: (a) Plot of the instantaneous apparent parabolic rate constant at 1200 °C and (b) the first hour of the plot shown in (a).

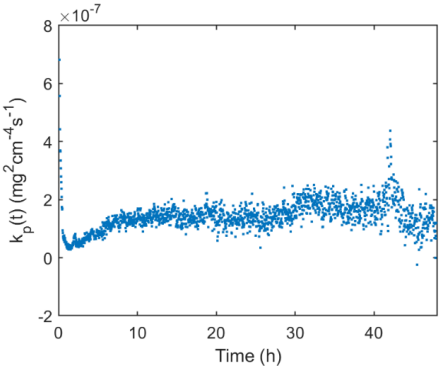

Fig. 5.8: Plot of the instantaneous apparent parabolic rate constant at 1000 °C.

5.5 Microstructure of oxide scale and carbide

5.5.1 Appearance of oxidised samples

Fig. 5.9 shows the Cr_2AlC samples after oxidation for 48 h and 20 h at 1000 °C and 1200 °C respectively. The oxide scale is dense and adherent, however, delamination occurs

in some areas at 1200 °C after oxidation for 20 h, after the sample is cooled down in the furnace. It must be noted that this does not occur during isothermal oxidation, since the TGA curves (**Fig. 5.6**) are smooth. They do not show any sudden drops in mass gain, which could be expected in case delamination of the scale occurs during isothermal oxidation. Delamination is not seen in the samples oxidised for shorter times at both temperatures.

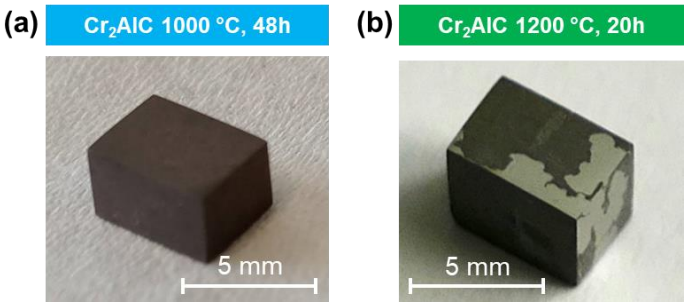

Fig. 5.9: Images of Cr_2AlC samples after oxidation at (a) 1000 °C for 48 h and (b) 1200 °C for 20 h. Delaminated regions can be observed in the sample oxidized at 1200 °C for 20 h after cooling down.

Low magnification SEM images of the oxidized samples at both temperatures are shown in **Fig. 5.10**. No edge effect is seen, i.e., no preferred growth of the oxide at the edges or corners occurs. But it is interesting to note that some regions near the edges of the sample oxidized at 1000 °C for 48 h show some flower-like growths, as seen in **Fig. 5.11**. This is possibly an effect of surface roughness, since the edges usually have a few grooves left even after the final grinding and polishing steps during metallographic preparation. However, the presence of these growths is not expected to affect the oxidation rate, since they are small and scarce.

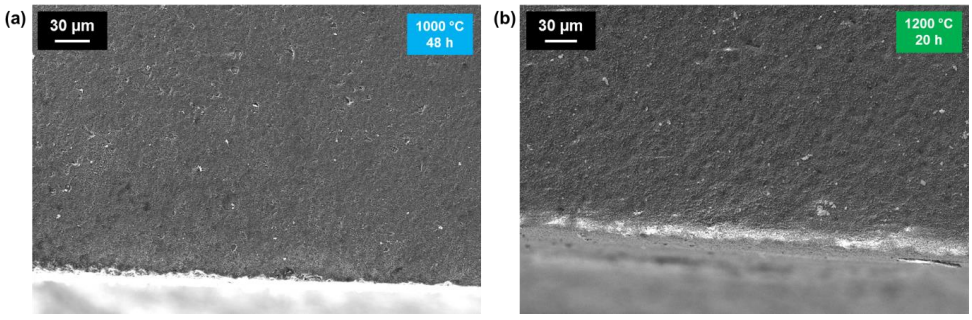

Fig. 5.10: Low magnification images of the edges of Cr_2AlC samples oxidised at (a) 1000 °C for 48 h and (b) 1200 °C for 20 h.

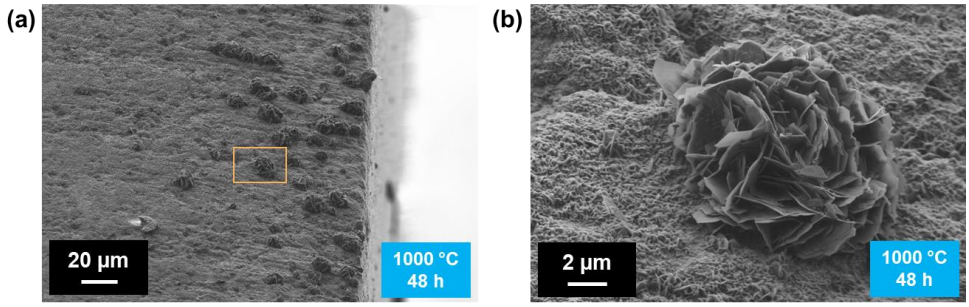

Fig. 5.11: SEM images of flower-like growth seen at some edge regions of the Cr_2AlC sample oxidized at 1000 °C for 48 h: (b) shows a magnified image of one such growth in (a).

5.5.2 Cross-section of oxide scale

Fig. 5.12 and **Fig. 5.13** show the cross-sections of the oxide scale formed at 1000 °C and 1200 °C after 48 h and 20 h respectively. A layer of platinum (Pt) was deposited on the surface for protection during FIB milling. At both temperatures, an alumina scale is formed with a porous carbide layer below it, with both layers being thicker after oxidation at 1200 °C. The carbide layer also contains small alumina particles remaining from the as-sintered material. Large irregularly-shaped pores are observed and contain small alumina particles at the walls. With increase in temperature and oxidation time, the size of the pores increases.

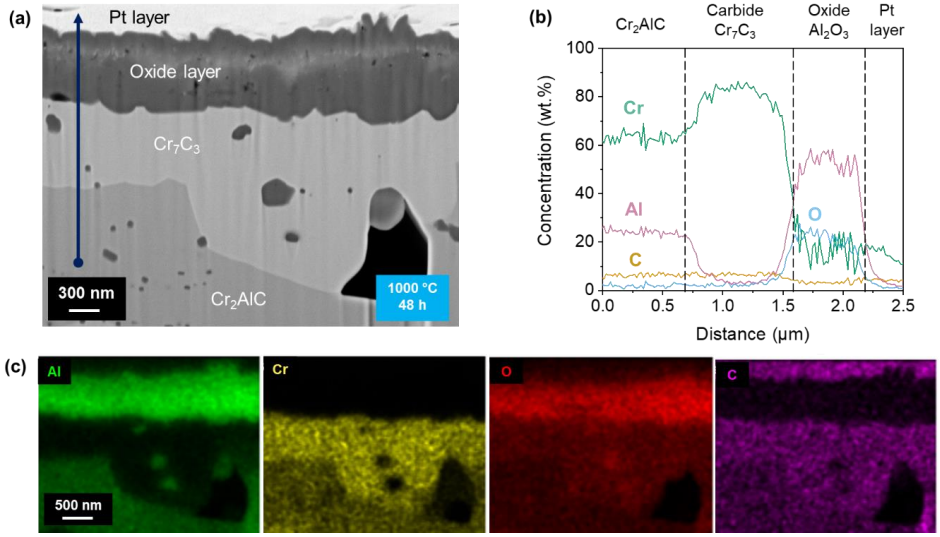

Fig. 5.12: (a) SEM image of the cross-section of the oxide layer formed at 1000 °C after 48 h (b) EDX line scan showing the variation in elemental concentrations along the dark blue arrow in (a) and (c) EDX elemental maps of the region shown in (a).

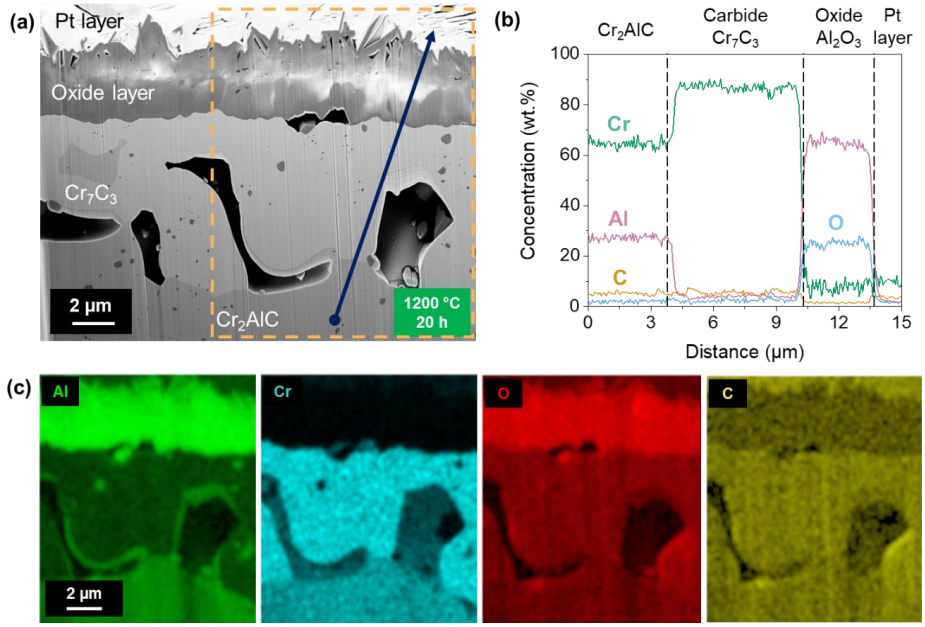

Fig. 5.13: (a) SEM image of the cross-section of the oxide layer formed at 1200 °C after 20 h (b) EDX line scan showing the variation in elemental concentrations along the dark blue arrow in (a) and (c) EDX elemental maps of the region marked with a box in (a).

Microstructures of the samples oxidized for 40 min, shown in **Fig. 5.14**, look similar to the microstructures obtained after oxidising for longer times, with the only difference in thicknesses of all layers. The carbide layer shows a large variation in thickness, while the alumina layer is more uniform. The thickness of the oxide and carbide layers in all samples calculated from SEM image analysis is summarized in **Table 5.2**.

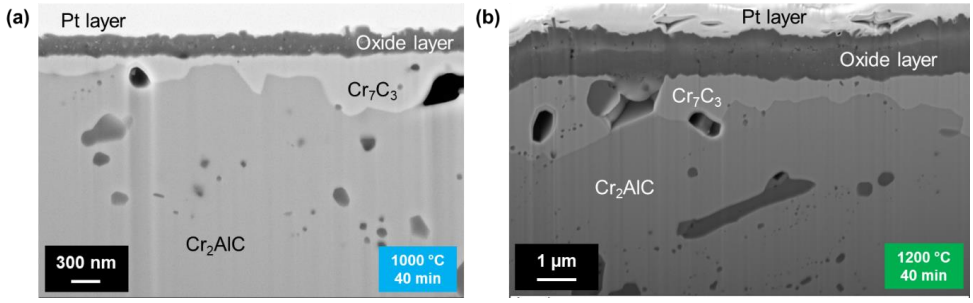

Fig. 5.14: SEM image of cross-section of oxide layer formed for shorter oxidation times: (a) 40 min at 1000 °C and (b) 40 min at 1200 °C.

Table 5.2: Average thicknesses of the alumina and carbide layers after oxidation as derived from the SEM image analysis

Temperature	Time	Al_2O_3 (μm)	Cr_7C_3 (μm)
1000 °C	40 min	0.22 ± 0.03	0.3 ± 0.19
1000 °C	48 h	0.74 ± 0.13	0.62 ± 0.52
1200 °C	40 min	1.10 ± 0.16	1.26 ± 0.71
1200 °C	20 h	3.38 ± 0.49	6.31 ± 1.86

XRD measurements were performed to confirm the phases present. The α-Al_2O_3 and orthorhombic Cr_7C_3 phases are found at both 1000 °C and 1200 °C, as seen in the XRD patterns in **Fig. 5.15**. No metastable alumina phases are detected at either of these temperatures, and the only carbide phase detected is Cr_7C_3.

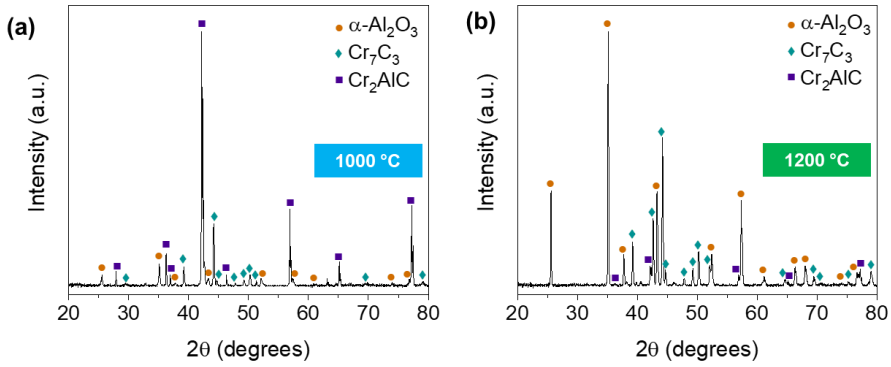

Fig. 5.15: XRD patterns confirming the presence of α-Al_2O_3 phase and Cr_7C_3 at (a) 1000 °C and (b) 1200 °C.

5.5.3 Morphology of oxide scale and carbide

The surface morphology of the oxide scale evolves with oxidation time and temperature, as seen in **Fig. 5.16**. After 40 min at 1000 °C, the formation of small alumina grains as well as small platelet-like structures in some regions is observed, as shown in **Fig. 5.16**(a). At 1200 °C, after 40 min of oxidation, small grains and platelets can still be seen, but the formation of needle-like structures can also be observed as shown in **Fig. 5.16**(b). After 20 h the surface is mostly covered with large blade-like structures with a few long needle-like grains, see **Fig. 5.16**(c) and **Fig. 5.17**. The blades are about 200-500 nm wide and grow up to 800 nm long, while the thin needles grow up to 2 μm long.

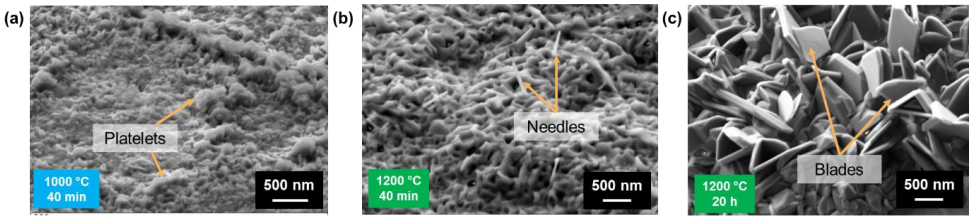

Fig. 5.16: Evolution of surface morphology of oxide scale with oxidation time and temperature: (a) platelets seen after oxidation at 1000 °C for 40 min, (b) needle-like structures seen after oxidation at 1200 °C for 40 min and (c) blade-like structures seen after oxidation at 1200 °C for 20 h.

While the outer part of the oxide scale consists of small platelets as well as needle-like and blade-like grains, the inner part of the alumina scale has a significantly different morphology. The inner oxide consists of large contiguous grains, as observed from the fractured cross-section of the oxide scale in **Fig. 5.17**. They are up to 800 nm in size after 20 h of oxidation at 1200 °C.

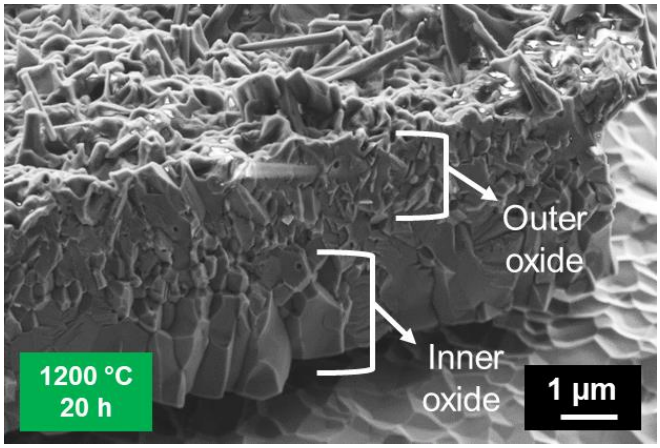

Fig. 5.17: Fractured surface of the alumina scale after oxidation at 1200 °C for 20 h after its partial delamination, showing the difference in morphology of the inner and outer parts of the oxide scale.

The partial delamination of the oxide scale in the sample oxidised for 20 h at 1200 °C also reveals the top surface of the carbide layer underneath, shown in **Fig. 5.18**. The concave pattern seen closely resembles the grain structure of the inner oxide layer, suggesting that there is good adherence between the oxide and carbide. The carbide seems to be softer than the oxide, which leads to the imprint of the oxide grains being left on the carbide to form these concave patterns. Some regions, such as in **Fig. 5.18**(b), contain small alumina particles from the as-sintered material, which are also seen within the pores in **Fig. 5.13**(a).

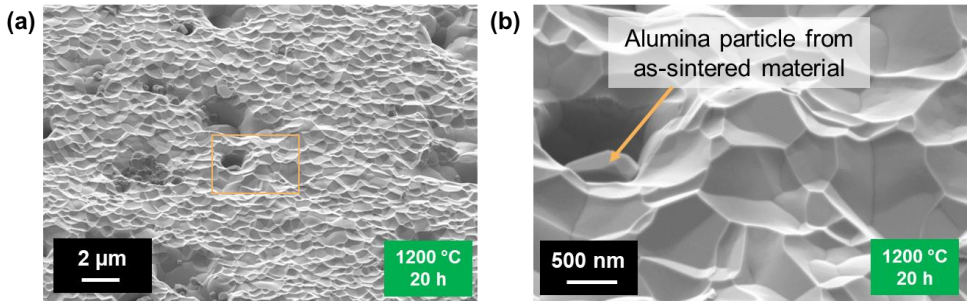

Fig. 5.18: (a) Top surface of the carbide layer revealed after partial delamination of the oxide on the sample oxidized at 1200 °C for 20 h (b) Magnified view of the region marked in (a).

5.5.4 Oxide growth direction

In order to determine oxide growth direction, attempts to use microscopic noble metal markers such as Au or Pd have been made in some studies of alumina formers [186,187]. Implanted markers are found to be more accurate than surface deposited markers. However, in cases where the element used as a marker interferes with oxide growth, it can lead to misinterpretation of the growth mechanisms [188]. In Cr_2AlC, the large alumina precipitates which are already present in the as-sintered material can be used as a marker of the original surface of the sample, since they do not get oxidized further, and can help to determine the growth direction of the oxide scale.

Fig. 5.19 shows FIB cross-sections done across such an alumina precipitate for the samples in the as-sintered and oxidized states. It is clearly distinguishable that small platelet and needle-like grains comprising the top part of the alumina scale form above the level of the original surface. At the same time, the lower large-grained layer is found below this level. This indicates that the platelet and needle-like alumina subscale grows outwards, while the large-grained subscale grows inwards, i.e., in the direction towards the bulk material. It should be noted that the thicknesses of the subscales are comparable, which suggests that the active diffusion of both Al and O ions occurs through the oxide.

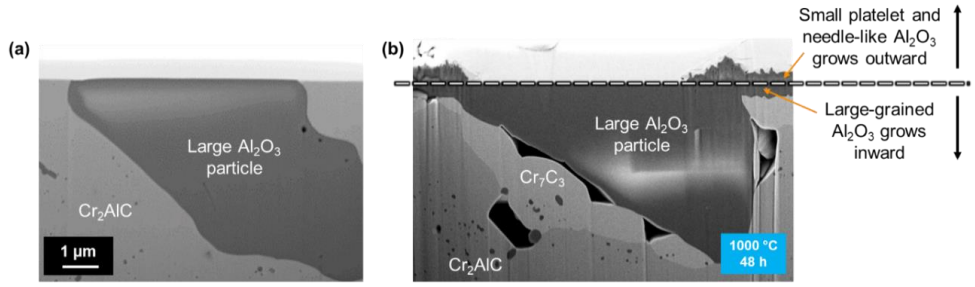

Fig. 5.19: Cross section across a large alumina particle in (a) the as-sintered sample (b) the sample oxidized at 1000 °C for 48 h. The alumina particle serves as a marker of the original surface.

5.5.5 TEM analysis of grain structure and Cr distribution

To study the grain structure of oxide scale and carbide at a larger magnification, STEM imaging using both STEM-in-SEM (with a maximum accelerating voltage of 30 kV) as well as a dedicated TEM (at an accelerating voltage of 200 kV) were used.

Fig. 5.20 shows the dark-field STEM images obtained at the maximum accelerating voltage of 30 kV of the sample oxidised at 1000 °C for 48 h. Although the grain structure of the oxide and MAX phase can be discerned here, this voltage is not high enough to resolve the grain structure of the carbide phase. A few bright spots in the oxide layer were identified, as seen in **Fig. 5.20**(b), but the resolution was not good enough to ascertain the chemical composition using EDX.

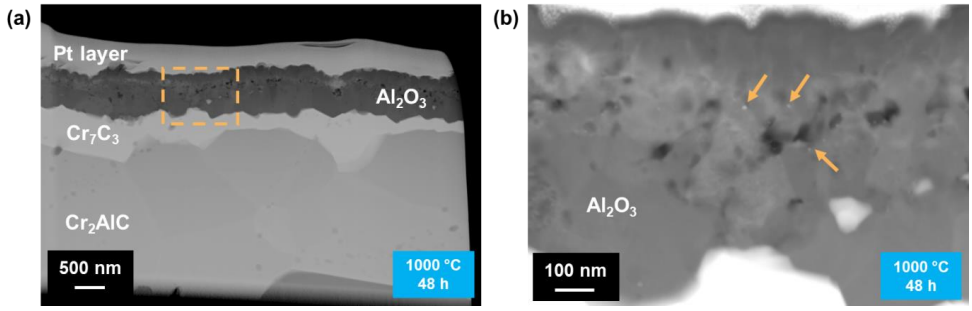

Fig. 5.20: (a) Dark-field STEM image (obtained using a STEM detector in SEM at accelerating voltage 30 kV) of the sample oxidized at 1000 °C for 48 h; (b) Magnified image of the region marked in (a), where the arrows point to bright spots seen in the oxide layer.

Fig. 5.21(a) shows the STEM-HAADF image (taken using a dedicated TEM at an accelerating voltage of 200 kV) of the sample oxidized at 1200 °C for 40 min. Due to the smaller scale thickness, all layers down to Cr_2AlC could be captured and imaged within a single TEM lamella. At this accelerating voltage, the grains of Cr_7C_3 could also be resolved. Both Cr_2AlC and Cr_7C_3 phases consist of relatively large grains, with Cr_2AlC grains being several microns in size, while the Cr_7C_3 grains are ≤ 1 μm large. **Fig. 5.21**(b) shows a magnified image from the oxide scale, where elongated larger grains of the inner subscale as well as the small-grained outer subscale can be distinguished. The inner alumina grains are, however, much smaller than the carbide grains, being ~200 nm wide. Between these two distinct morphologies, an intermediate region with fine bright GB precipitates can be seen, which partially penetrates both morphologies. An EDX map of Cr in **Fig. 5.21**(c) shows that these precipitates are Cr-rich, and the entire intermediate region is enriched in Cr, which could be remnant from the transient oxide formation.

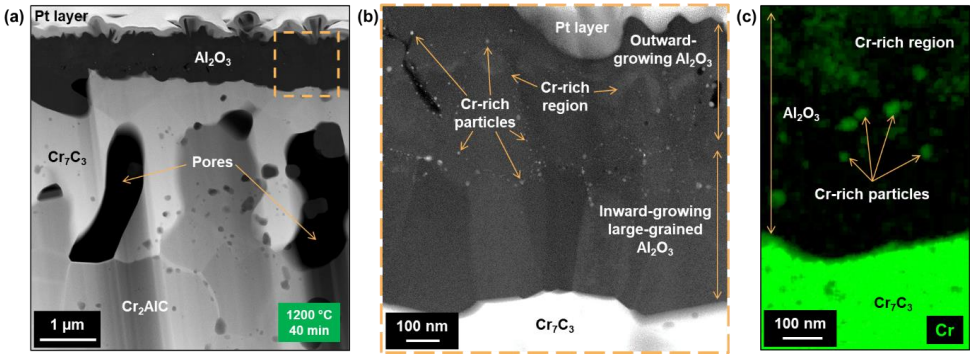

Fig. 5.21: (a) STEM-HAADF image of the sample oxidized at 1200 °C for 40 min; (b) a magnified STEM-HAADF image of the alumina scale marked with a dashed frame in (a); (c) EDX map of Cr, showing the presence of a Cr-rich intermediate region with Cr-rich precipitates in the alumina layer.

5.6 Need for APT

The overall microstructure and chemical composition of the oxide scale and carbide could be characterised to a large extent using conventional characterisation tools, as described in the previous section. However, one of the shortcomings of electron microscopy techniques is that they provide very scarce chemical information for low-dimensional objects such as GBs, especially when it comes to low elemental concentrations and light elements. Since the TGA results indicate that the oxidation rate is parabolic, i.e., controlled by ionic diffusion, it is also important to study the local chemistry of key diffusion pathways such as GBs, especially of Al_2O_3 scale, since it has been established that diffusion through alumina proceeds exclusively through GBs [32].

In order to address questions pertaining to the diffusion pathways of elements to build the oxide scale, APT was used to map and quantify three-dimensional elemental distributions, specifically at GBs and interfaces, with sub-nanometre resolution. For example, it is assumed that Al diffuses through GBs in Cr_2AlC [115] and in Cr_7C_3, but this has not been proven experimentally.

Additionally, APT helps to reveal the distribution and influence of impurities, which may segregate at GBs and interfaces, thereby greatly affecting diffusion processes and eventually the oxidation rate. Such impurities may originate from raw materials of insufficient purity or from production routes. These impurities could be a reason for the inconsistencies seen in various published results, such as different rates of oxidation under similar conditions, as well as differences in the oxidation products formed, as previously described in Section 2.2.7. Therefore, this is an important aspect to be addressed to avoid misinterpretations of the experimental results.

5.7 Parameter optimization for APT study of Cr_2AlC

Since the only existing APT studies on Cr_2AlC are done on thin films [189,190], the ideal parameters for the study of bulk Cr_2AlC specimens in the atom probe were not known. Hence, a parameter optimisation study was performed on specimens prepared from the as-sintered Cr_2AlC sample. The parameters studied were the pulse rate measured in kHz, the laser pulse energy (LPE) measured in pJ, the detection rate (DR) in % and specimen temperature in K.

5.7.1 Effect of pulse rate

The best pulse rate is the maximum rate that is able to capture the entire range of the mass-to-charge ratio (M) of the ions produced by a given material. If the pulse rate is too high, ions with a long time of flight, i.e., higher mass-to-charge ratio, are only detected in the next pulse window, which results in a wrap-around effect. This manifests as a broad peak at the lower end of the mass spectrum, and can result in ions with higher M values not being assigned the element they belong to, which leads to under detection of these elements. This is typically seen in materials with heavier elements such as W, or that have poor thermal diffusivity [176].

For the as-sintered Cr_2AlC sample, the highest pulse rate of 250 kHz was used, with the other parameters being 40 pJ pulse energy, 0.5% detection rate and a temperature of 50 K, as a starting point. Even at this pulse rate, no wrap around effect was seen, even at lower voltages. Hence, the pulse rate was fixed at the maximum rate of 250 kHz for subsequent measurements.

5.7.2 Effect of laser pulse energy (LPE)

The laser pulse energy (LPE) denotes the total energy carried by each laser pulse, which heats up the specimen tip and results in a lowering of the field required for the evaporation of ions from the specimen surface. Since a lower field is necessary, this reduces the stress on the specimen, which leads to a lower chance of specimen fracture and increases the analysis yield. Hence, it is preferable to use a high LPE. However, when the LPE is too high it can also have negative effects such as increased surface migration, complex ion formation and non-uniform heating of the tip, which can lead to non-uniform evaporation. This is more pronounced for non-conductive materials like oxides, carbides and nitrides, and can negatively affect the compositional accuracy as well [176]. Hence, it is important to find the highest LPE that is still able to give a reasonably accurate composition.

With the pulse rate fixed at 250 kHz, 0.5% detection rate and temperature of 50 K, the LPE was varied from 100 pJ to 70 pJ, 50 pJ and then decreased in steps of ten to 10 pJ.

The uniformity of evaporation can be seen through the detector event histogram, which shows the distribution of ions over the detector area. **Fig. 5.22** shows how the detector event histogram becomes less uniform as the LPE is increased from 40 pJ to 100 pJ. The variation in the uniformity of evaporation, composition and mass spectrum background is summarised in **Table 5.3**. When the LPE is greater than 50 pJ, the evaporation is not uniform anymore, hence it is advisable to not use an LPE greater than this value. The composition is also negatively affected with increase in LPE, primarily leading to an under-detection of the amount of C, which occurs due to the increased formation of molecular ions and multiple hit events [191]. However, the drawback of using a lower value of LPE is the increase in background level. Considering these factors, 40 pJ seems to be the optimal value of LPE, since it results in uniform evaporation, a low background of ~15 ppm/ns and has a relatively low amount of C under-detection.

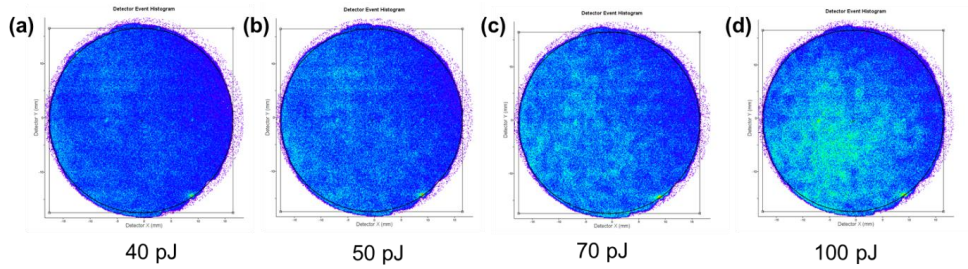

Fig. 5.22: Variation in uniformity of detector event histogram with increase in LPE from (a) 40 pJ, (b) 50 pJ, (c) 70 pJ to (d) 100 pJ.

Table 5.3: Summary of effect of changing LPE on uniformity of evaporation, composition and mass spectrum background

LPE (pJ)	Uniformity of evaporation	Composition (at.%)				Background (ppm/ns)
		Cr	Al	C		
100	Hot spots	59.4	29.4	11	C content underestimated	10-15
70	Non-uniform	56.6	27.7	15.6		10-15
50	Uniform	54.5	26.5	19		10-15
40	Uniform	53	26	20.9	C content slightly less than nominal value	~15
30	Uniform	52.4	26	21.6		~20
20	Uniform	51.5	26.2	22.2	C content close to nominal value	20-25
10	Uniform	49.9	26.5	23.5		35

5.7.3 Effect of detection rate (DR)

The detection rate (DR) is the number of ions detected per pulse. It is typically in the range of 0.005 to 0.01 ions per pulse, or 0.5 to 1% in terms of percentage. The DR is kept at such low values so that the number of multiple evaporation events is also reduced, since the position sensitive detector can sometimes not properly detect multiple hits [176]. Despite this, the data collection rate is still quite high since very high pulse rates can be used, especially in the laser-pulsed mode. For example, with a DR of 0.5% and a pulse rate of 250 kHz, it takes about 13.5 minutes to collect data of 1 million ions.

In general, a larger DR leads to an increase in data quality and minimises the total time for data collection. However, to increase the DR it is also necessary to increase the applied voltage, which can decrease specimen yield. In materials containing carbon and boron, an increased DR also resulted in decreased efficiency due to a higher proportion of multiple-hit events [176].

To study the effect of DR, the pulse rate was fixed at 250 kHz, an LPE of 40 pJ was used and the specimen temperature was kept at 50 K. The DR was varied from 0.2, 0.3, 0.5 to 1%. The summary of the effect of DR variation is shown in **Table 5.4**. Changing the DR does not have an effect on the uniformity of evaporation. However, a lower DR causes an increase in background, while a higher DR increases the percentage of multiple-hit events. Therefore, a DR of 0.5% is a reasonable rate for data collection.

Table 5.4: Summary of effect of changing DR on uniformity of evaporation, mass spectrum background and multiple-hit events

DR (%)	Uniformity of evaporation	Background (ppm/ns)	Multiple-hit events (%)
0.2	Uniform	20-25	20
0.3	Uniform	15-20	22
0.5	Uniform	~15	25
1.0	Uniform	5-10	>25

5.7.4 Effect of specimen temperature

APT specimens are usually kept at cryogenic temperatures in the range of 20-80 K to minimise surface diffusion during the measurement. A lower temperature is generally better since it is found to decrease the background due to the decreased mobility of residual gases and provide higher quality data [176]. However, lower temperatures can also have a negative impact on the specimen yield.

For Cr_2AlC, the effect of lowering the specimen temperature to 20 K from 50 K was analysed. The other parameters were fixed at 250 kHz pulse rate, 40 pJ LPE and 0.5% DR. The background decreases from 15 ppm/ns at 50 K to 10-15 ppm/ns at 20 K,

however this is not a significant advantage since the background is already reasonably low at 50 K. Since a lower temperature can decrease the specimen yield, the optimal temperature was chosen as 50 K. Based on previous studies, a similar set of parameters (pulse rate of 250 kHz, 50 pJ LPE, 0.5% DR and a temperature of 50 K) is also suitable for the measurement of alumina [192].

5.8 APT analysis of different regions after oxidation

The sample oxidized at 1200 °C for 40 min was used for the APT analysis, since the oxide layer is less porous and is ~1 μm thick, which is good for APT specimen preparation. Specimens were prepared both in the standard lift-out method (normal orientation) as well as using the backside lift-out method (180° rotated with respect to normal orientation), illustrated in **Fig. 5.23**. The latter method was primarily used to access the deeper parts such as the carbide and underlying Cr_2AlC, and to have a more stable configuration of having the low-field evaporating carbide on top of the high-field evaporating oxide, which made it possible to study the oxide-carbide interface. The results are presented in this section starting from the underlying Cr_2AlC, followed by the carbide, then the inner oxide as well as the transient oxide region. The interfaces between the three phases are also analyzed sequentially.

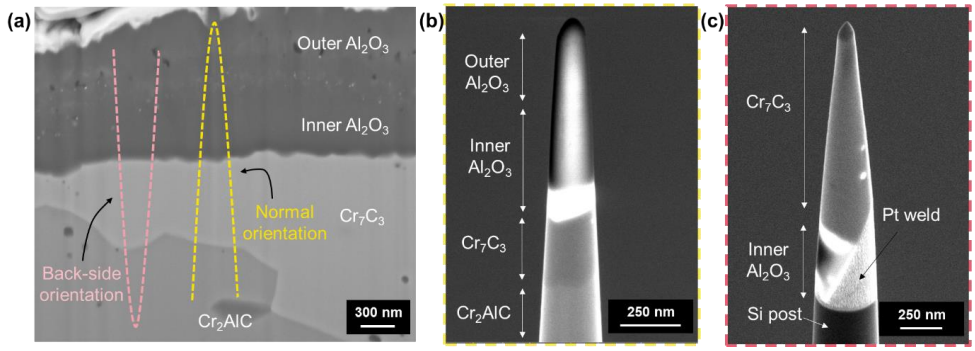

Fig. 5.23: (a) Orientations of a standard lift-out specimen (normal orientation) and back-side lift-out specimen (180° rotated with respect to the sample); SEM images of APT specimens prepared using (b) standard lift-out procedure and (c) back-side lift-out procedure.

5.8.1 Cr_2AlC and interface with Cr_7C_3

Fig. 5.24(a) shows APT elemental maps from the Cr_2AlC-Cr_7C_3 interface and the adjacent volumes of these phases. This region of the microstructure is marked in **Fig. 5.24**(b). The data was obtained using a back-side lift-out specimen. Minor impurities such as Fe, Si, P and B were detected, which likely originate from the raw materials. The proximity histogram in **Fig. 5.25**(a) shows no pile-up of any element at the

interface as well as no Al gradient on the Cr_2AlC side near the interface. There is a minor segregation of Fe, Si and P at the interface.

In order to quantify the amount of GB segregation, the calculation of Gibbsian interfacial excess values was performed [193]. Being a thermodynamic variable, this provides a more representative measure of GB segregation as compared to the peak concentration of elements at the GB, which is more affected by factors such as the spatial resolution of the analysis technique used [194]. Gibbsian interfacial excess values of ~0.5 atoms/nm^2 for Fe and 0.3 atoms/nm^2 for Si were obtained for the Cr_2AlC-Cr_7C_3 interface. The total segregation amount does not exceed 1/10 of a monolayer coverage at the interface, so no notable effect of these impurities on the interface structure or properties is expected.

Based on the segregation of Si and Fe in the elemental maps, a GB in Cr_2AlC close to the interface can be identified. The concentration profile across this GB in **Fig. 5.25**(b) shows a clear enrichment of Al, being in agreement with the earlier conclusions about the predominant GB character of Al diffusion through Cr_2AlC [115]. The total segregation level of impurities (~0.7 atoms/nm^2 for Fe) is again far below a monolayer coverage and hence is not expected to notably affect GB diffusion.

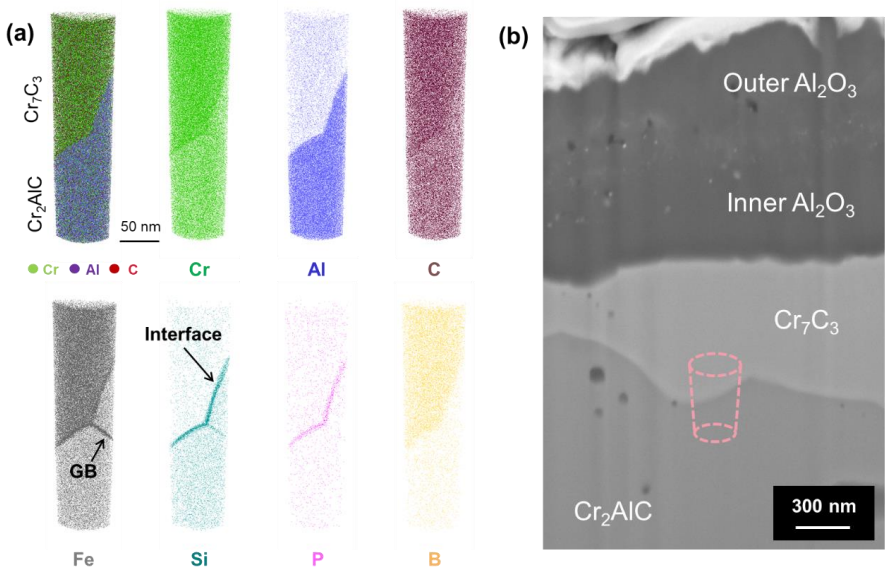

Fig. 5.24: (a) APT elemental maps from the Cr_2AlC and Cr_7C_3 phases and their interface. The region of the microstructure being referred to is marked in the SEM image of the cross-section in (b).

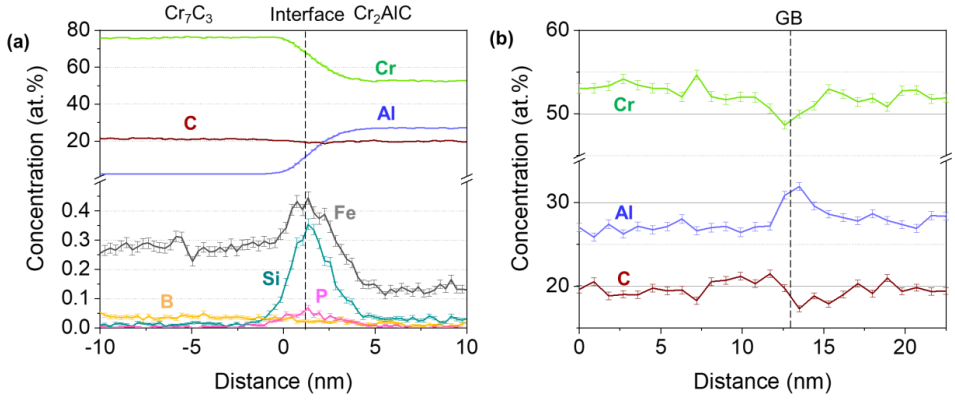

Fig. 5.25: (a) Proximity histogram showing variation in concentrations of the main elements and impurities across the interface and (b) concentration profiles across the GB in Cr_2AlC.

The bulk compositions of the as-sintered Cr_2AlC as well as of the carbide and Cr_2AlC in the oxidized sample are shown in **Table 5.5**. Note that the amount of C is under-detected by about 1/5, which is a common artefact in the APT analysis of carbides [191]. A slight decrease in Al in Cr_2AlC after oxidation is observed due to its consumption by the growing alumina layer.

Table 5.5: Bulk compositions of Cr_2AlC and Cr_7C_3 phases (in at.%) obtained by the APT analysis

Concentration (at.%)	**Cr_2AlC as-sintered**	**Cr_2AlC after oxidation, just below the carbide**	**Cr_7C_3**
Cr	53.5	54.3	77.4
Al	26.0	25.0	0.6
C	20.3	20.4	21.6

5.8.2 Cr_7C_3

Fig. 5.26(a) shows APT elemental maps from the Cr_7C_3 carbide layer. This region of the microstructure is marked in **Fig. 5.26**(b). The data was again obtained using a back-side lift-out specimen. Based on the planar segregation of Si and P, a GB can be recognized. Two small alumina precipitates present in the carbide can also be seen.

Fig. 5.27 shows concentration profiles across the carbide GB, where only a negligible Al enrichment at the GB is observed. However, the absolute concentration is not accurate in this profile due to the peak overlap in the APT mass spectrum. Therefore, peak deconvolution analysis was performed in thin identical sub-volumes including the GB, close to the GB and distant from the GB (grain interior). The results shown in

Table 5.6 demonstrate that the maximum GB enrichment of Al does not exceed 0.3 at.%. Given a notable bulk concentration of Al detected in Cr_7C_3, this may be an indication of active bulk Al diffusion through the carbide layer.

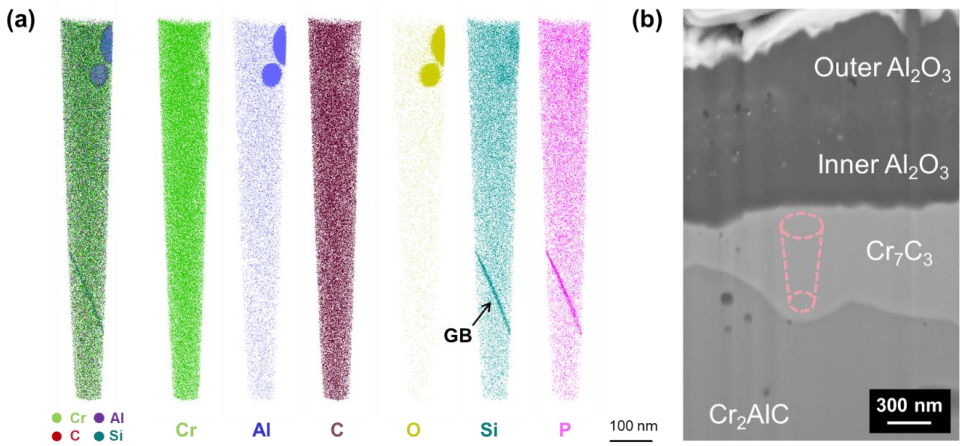

Fig. 5.26: (a) APT elemental maps from the Cr_7C_3 phase, containing a GB and small Al_2O_3 precipitates. The region of the microstructure being referred to is marked in the SEM image of the cross-section in (b).

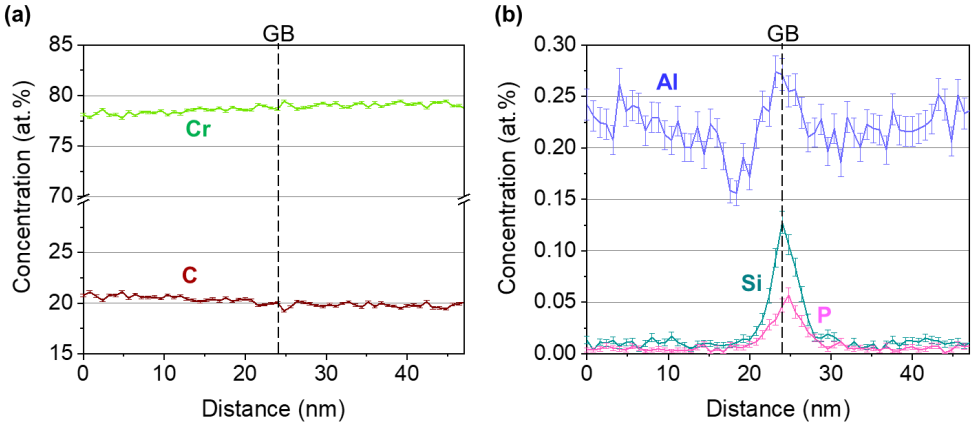

Fig. 5.27: Concentration profiles across the GB in Cr_7C_3 (a) of Cr and C (b) of Al, Si and P.

Table 5.6: Elemental concentrations (in at.%) in Cr_7C_3 at the GB, near the GB and in the grain interior after the APT peak deconvolution procedure

Concentration (at.%)	Carbide GB	Close to GB	Grain interior
Cr	78.6	78.8	79.0
Al	0.7	0.4	0.5
C	20.0	20.3	19.9

5.8.3 Al_2O_3 and interface with Cr_7C_3

The APT analysis of the inner Al_2O_3 subscale with the interface to the adjacent Cr_7C_3 layer can be seen in **Fig. 5.28**(a). **Fig. 5.28**(b) indicates this region in the cross-section. In this case too, a back-side lift-out specimen was used so that the low-field evaporating carbide is on top of the high-field evaporating alumina during the APT measurement.

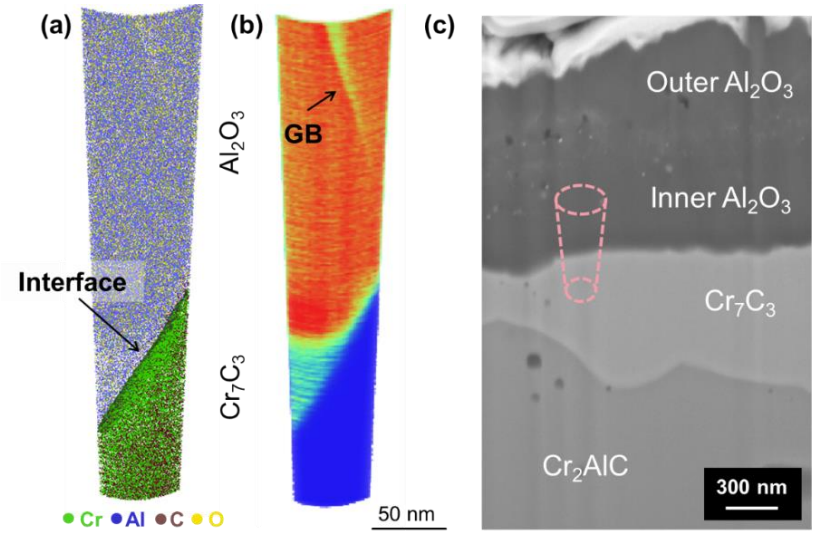

Fig. 5.28: (a) A combined APT elemental map of the carbide-oxide region, (b) ionic density map showing the presence of a GB in the inner alumina. The region of the microstructure being referred to is marked in the SEM image of the cross-section in (c).

From all impurities, only Fe segregation was detected at the interface at a level of ~1 atom/nm^2, which is again far below a monolayer interfacial coverage and hence is not expected to affect interfacial properties such as adhesion of the oxide scale. An interesting point to note from the proximity histogram in **Fig. 5.29** is that the local C concentration in Cr_7C_3 drops by a factor of two next to the interface, indicating that this region of the carbide is strongly non-stoichiometric, which may help to accommodate growth stresses between the layers.

Due to the known APT artefact of small variations in the apparent ionic density between grains [195], an alumina GB could be identified in the dataset as shown in **Fig. 5.28**(b). However, no segregating elements such as Cr, C or any impurities were detected at the GB, and no elements except Al and O were found by APT within the alumina grains. This indicates that the inner alumina scale is pure.

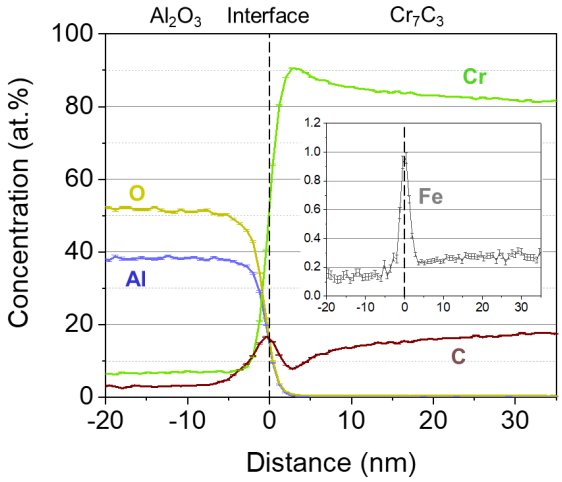

Fig. 5.29: Proximity histogram for elemental concentrations across the carbide-oxide interface.

Fig. 5.30(a) shows the APT analysis of the outer part of the oxide scale. The part of the oxide scale analysed is indicated in **Fig. 5.30**(b). Here, the APT measurement was done on a standard lift-out specimen.

Unlike the inner alumina scale, the analysed region of the outer alumina contains 3-4 at.% of dissolved Cr. This could be correlated with the Cr-enriched region seen in the TEM-EDX map in **Fig. 5.21**(c). Enrichment of Cr at the GB was also observed, as seen in the concentration profile in **Fig. 5.30**(b).

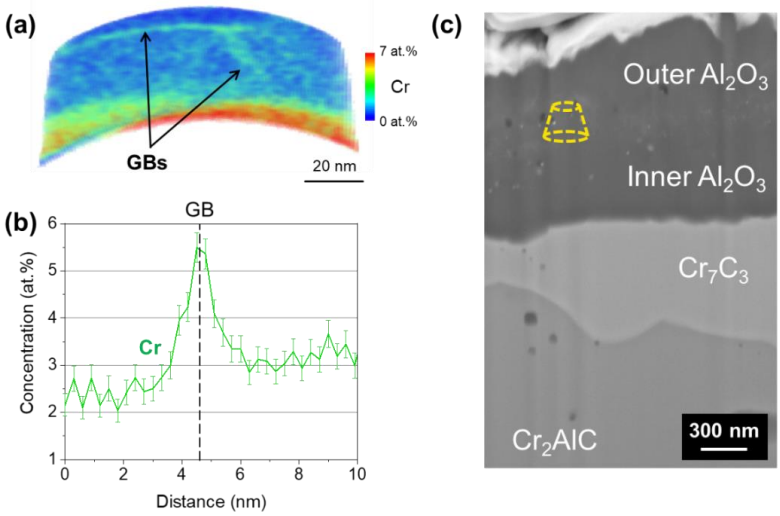

Fig. 5.30: APT analysis of the outer part of the oxide scale: (a) concentration map of Cr, enrichment shows the presence of GBs and (b) a concentration profile of Cr across the GB. The region of the microstructure being referred to is marked in the SEM image of the cross-section in (c).

5.9 Diffusion and oxide growth processes

5.9.1 Simultaneous formation and growth of carbide and oxide

The experimental results show that the alumina scale growth is accompanied by the continuous formation of the carbide layer from early oxidation times (≤ 40 min). It has been suggested that the oxidation of Cr_2AlC takes place by the following reaction [108,109]:

$$28Cr_2AlC + 25O_2 \rightarrow 14Al_2O_3 + 8Cr_7C_3 + 4CO_2 \qquad \text{(Equation 5.3)}$$

This equation is used as the basis for the calculations made in the following sub-sections.

5.9.1.1 Void formation in carbide

As the oxide starts to form, a depletion of Al in Cr_2AlC occurs, resulting in the appearance of a Cr_7C_3 layer below the oxide. During this transformation, almost all the Al atoms diffuse out of the MAX phase, which is ~1/4 of the total number of atoms. In addition, the volume of the pre-transformed Cr_2AlC does not match the volume of the newly formed carbide. In fact, the volume of Cr_7C_3 expected to be formed based on Equation 5.3 is only 58% of the volume of Cr_2AlC that it is formed from. This value was calculated using the theoretical densities of the two phases, i.e., 5.23 g/cm^3 for Cr_2AlC and 7.2 g/cm^3 for orthorhombic Cr_7C_3 [196]. The formation of carbide goes on continuously during oxidation, under the existing continuous alumina scale, so the Al loss must be accompanied by void formation, which explains the large porosity observed in the carbide layer.

The porosity could also be correlated to the formation of CO or CO_2 gas in previous studies [110]. The equation was balanced assuming formation of only CO_2, but formation of CO is also possible. Lin *et al.* analysed the gas formed during oxidation by mass spectrometry and confirmed the formation of CO_2 but could not conclude about the formation of CO since it has the molecular weight identical to N_2 [108]. Another reason for shifting the carbon balance in this process may be the carbon deficit (i.e. non-stoichiometry) in the Cr_7C_3 phase. Nevertheless, these issues do not shift the balance between Cr and Al.

5.9.1.2 Sources of Al for oxide formation

Al necessary for oxide scale formation comes from the decomposition of Cr_2AlC into Cr_7C_3 (according to Equation 5.3) as well as from depletion of Al in Cr_2AlC below the carbide layer, as observed from APT. By analysing the SEM cross-sections, the relative volumes of the carbide and alumina formed can be determined, and given the known

densities of the phases, the molar amounts of Al released from the formation of Cr_7C_3 and consumed by the formation of the alumina scale can be estimated and compared.

From Equation 5.3, one mole of Al_2O_3 requires decomposition of two moles of Cr_2AlC and results in formation of ~0.57 moles of Cr_7C_3. Hence, if 0.57 moles of Cr_7C_3 forms per mole of Al_2O_3, all Al for the formation of the oxide layer comes solely from the decomposition of Cr_2AlC. However, if less than 0.57 moles of Cr_7C_3 emerges, the decomposition of Cr_2AlC alone cannot provide all necessary Al, and some Al must diffuse from the unreacted Cr_2AlC to complete the oxide scale formation.

The approximate balance of carbide and oxide phases estimated from the SEM cross-sections is summarized in **Table 5.7**. It should be noted that the carbide layer contains large pores, whose total area in an SEM image may not accurately represent the average porosity, and the estimated volume of the carbide may be slightly biased.

For the sample oxidized at 1000 °C for 40 min, all Al needed to form the oxide layer comes entirely from the decomposition of Cr_2AlC. However, in case of a longer oxidation or at 1200 °C, decomposition of Cr_2AlC provides less Al than required to form the oxide. This suggests that when the stable oxide layer starts to form, all alumina is formed from the decomposition of Cr_2AlC, but further growth involves additional Al from the unreacted Cr_2AlC, which must diffuse through the carbide layer.

Table 5.7: Molar balance of Al for the formation of the Al_2O_3 scale

Temperature	Time	Cr_7C_3/Al_2O_3 molar ratio	% of Al obtained due to formation of Cr_7C_3
1000 °C	40 min	0.59	~100%
1000 °C	48 h	0.36	63%
1200 °C	40 min	0.41	72%
1200 °C	20 h	0.44	77%

APT analysis shows only ~1 at.% depletion of Al in Cr_2AlC close to the carbide layer. This behaviour is different from typical depletion patterns under high-temperature oxidation of alloys and could be explained by the very stoichiometric nature of Cr_2AlC as established from ab initio calculations [197]. A stoichiometry with excess Al, i.e., where Al replaces some Cr sites in Cr_2AlC, was also shown to be metastable. Since ~1/4 of Al at long oxidation times is sourced from depleting but still not decomposing Cr_2AlC (**Table 5.7**), the depth of the depleted layer is expected to be large, and Al diffusion through Cr_2AlC should also be considered.

5.9.2 Structure and composition of oxide scale

5.9.2.1 Possible role of water vapour on oxide scale morphology

All studied oxidation conditions resulted in formation of a continuous α-Al_2O_3 scale consisting of two distinct sublayers – the outward-growing platelet and needle-like grains and the inward-growing large grains. An oxide layer growing in both outward and inward directions has been observed in some alumina-forming alloys, such as FeCrAlY and NiAl. Typically, the outer layer consists of small grains growing on top of larger columnar alumina grains [32,198,199].

Emergence of needle-like alumina grains is quite an unusual phenomenon in oxidation processes and is usually attributed to the formation of metastable forms of Al_2O_3. For example, the cubic θ-Al_2O_3 phase has such a needle-like or blade-like morphology, predominantly grows due to outward diffusion of Al [200] and can transform into the stable α-Al_2O_3 at higher temperatures [32]. But in Cr_2AlC, no θ-Al_2O_3 phase has been detected through XRD, even at intermediate temperatures [109]. Hence, the formation of metastable forms of alumina does not seem to be the reason for the formation of these needle-like structures in Cr_2AlC.

Since this particular morphology of the oxide surface is typically not observed in dry oxidation conditions above 1100 °C [109,112], the presence of water vapour could also play a role. During the oxidation of TiAl, needle-like rutile was formed in the presence of water vapor, which is attributed to the preferential adsorption of water on certain crystallographic planes of rutile, and the resulting changes in defect chemistry [201].

A similar effect might be the reason for needle and blade-like alumina growth in the presence of water vapor. It has been theoretically shown that the surface energy of different crystallographic planes of α-Al_2O_3 changes with the chemical or physical adsorption of water, resulting in a different growth morphology as compared to an unhydrated crystal [202]. Hence, the enhanced stability of certain crystallographic planes in the presence of water could be a reason for the formation of the needle and blade-like structures of alumina in Cr_2AlC.

5.9.2.2 Formation of Cr-enriched region in oxide

The middle part of the oxide scale is enriched with Cr, both as a solute in the Al_2O_3 bulk and as copious Cr-rich precipitates at GBs. This enrichment likely stems from the initial transient stage, when Cr and Al could oxidize in parallel to form a mixed oxide, and later this region is buried between two oppositely growing alumina sublayers. A similar mixed oxide has also been observed in other studies [97,110].

APT analysis shows that the transient oxide contains about 3-4 at.% Cr dissolved in the bulk. The large width of the Cr-containing layer indicates that the initial

concentration of Cr in the alumina grains was apparently higher, and later Cr started to diffuse out of the transient layer. Cr-rich nanoparticles seen at GBs in Fig. 6(b) could be formed due to this Cr diffusion to GBs with subsequent nucleation of chromia or a mixed oxide.

Some initial chromium loss during the transient oxidation stage could also occur since the chromia formed can react with water vapour and form volatile species such as the oxyhydroxides $CrO_2(OH)$ and $CrO_2(OH)_2$, as well as CrO_3, especially at temperatures ≥ 1000 °C [34,203]. However, this is not expected to affect the ionic transport processes, especially after a stable alumina layer is formed, since the Cr-enriched region is completely contained between the two alumina sublayers.

5.9.3 Diffusion of Al and O ions and effect of impurities

5.9.3.1 Diffusion through oxide scale

It has been concluded earlier that oxygen ion transport through alumina GBs controls the growth of the oxide scale and eventually the oxidation rate [32], and in particular in alumina-forming MAX phases [113]. In the bilayer α-Al_2O_3 structure seen in the present work, the total diffusion flux through the large-grained inner layer must be generally slower due to the lower density of the GB network compared to the outer layer, where porosity can further increase the mass transport. Hence, the diffusion through the inner alumina sublayer is expected to be rate-controlling for the entire oxidation process.

Despite the presence of small amounts of impurities such as Fe, Si, P and B in the initial MAX phase material, these elements neither segregate at GBs of the large-grained inner alumina nor dissolve in the bulk of that region. More importantly, no Cr or C is found in the inner alumina as well, within the detection limit of APT (~10 ppm). Therefore, the inner oxide sublayer consists of pure alumina, similar to oxide scales growing on alumina-forming alloys with no reactive element added.

It is known that many elements, either intentionally added or incorporated as processing impurities, can substantially affect the ionic diffusion rate through alumina GBs [204]. Controlling the impurity level and specifically confirming their absence in the rate-controlling region is thereby important, since it renders the experimental results as reliably representative of the oxidation of a pure material. If impurities are occasionally introduced and not properly controlled, biases in the oxidation behaviour may occur, which may be responsible for discrepancies in the results reported in other studies.

Unlike the inner subscale, the outer part of the alumina scale contains Cr as a bulk solute, GB segregation and Cr-rich precipitates. Dissolved Cr is not expected to slow

down the ionic diffusion through Al_2O_3 and could rather accelerate it, and the presence of Cr-rich nanoparticles will not have a significant effect either, since they occupy a small fraction of the total GB area. Given the smaller grain size and hence larger GB network density, the overall mass transport through the outer scale must be faster and eventually not limit the oxidation rate.

5.9.3.2 Diffusion through carbide layer

Diffusion through the Cr_7C_3 layer is not expected to be rate-limiting as well. From APT, the carbide contains ~0.6 at.% Al with no significant Al enrichment at the GBs, indicating that Al may actively diffuse through the carbide bulk and does not seem to preferably diffuse via GBs. Since carbides are often quite defective, i.e., with a lot of vacancies, this could greatly accelerate diffusion compared to an ideal stoichiometric compound. Additionally, the available diffusion area through the bulk is much larger than the total GB area, so a large amount of Al can be transported through the bulk. An important consequence from this finding is that any changes in the grain size of the carbide will not affect the oxidation rate of Cr_2AlC.

The porosity in the carbide layer could provide additional transport paths, but such transport would proceed through the pore walls for metallic cations, hence the large pores present in the carbide cannot provide many transport paths. Therefore, these large pores seem to be only a minor factor in the total mass transport, and the diffusion of Al primarily occurs through the bulk of the carbide.

5.9.3.3 Diffusion through Cr_2AlC

When it comes to Al supply from the depletion of the Cr_2AlC phase without decomposition, APT shows Al enrichment at grain boundaries, suggesting that diffusion through Cr_2AlC predominantly occurs via GBs. However, the decomposition of Cr_2AlC remains the main source of Al (> 70%) for the oxide scale growth, and the depleted Cr_2AlC contains numerous vacancies at Al sites which may facilitate bulk diffusion of Al from deeper regions. This also renders GB diffusion through Cr_2AlC as not rate-limiting, and explains the earlier observed absence of the dependence of oxidation rate on the Cr_2AlC grain size [111].

It should be noted that the APT data obtained in this study is not sufficient to directly visualize or assess the Al diffusional flux through the carbide and MAX phase. An approach such as the one used by Boll *et al.* in their study of alumina formation in NiAl would be required here, where the material is first oxidized, then the top layer of alumina is mechanically removed, followed by another short step of oxidation. The outward Al flux can then be visualized and quantified based on the volume of the new oxide formed during the second oxidation step [205].

5.9.4 Mechanism of oxide formation

Based on the above observations, a mechanism of oxide formation in Cr_2AlC is proposed (**Fig. 5.31**):

i. In the transient stage of oxidation, a mixed oxide of alumina with dissolved Cr is formed, since both Al and Cr on the surface of the material react with oxygen from the atmosphere.

ii. A stable α-Al_2O_3 layer starts to form, with both outward and inward components growing in parallel. The outward-growing alumina shows up in the form of small grains and platelets, while the inward-growing alumina is in the form of large grains. Al diffuses from the Cr_2AlC to form the oxide scale, and since Cr_2AlC can only tolerate ~1 at.% of Al depletion, it quickly transforms into the carbide Cr_7C_3 underneath. In the initial stage of stable oxide formation, all Al required can be obtained from Cr_2AlC decomposition.

iii. Meanwhile, Cr ions from the thin transient oxide region diffuse into the neighbouring alumina, creating a thick Cr-enriched layer with 3-4 at.% Cr dissolved in Al_2O_3 and nucleated Cr-rich oxide nanoparticles at GBs.

iv. With increase in oxidation time, as the oxide layer continues to grow in thickness, outward-growing needle-like structures of α-Al_2O_3 start to form, eventually resulting in the formation of blade-like structures as well, which could be due to the preferred growth of certain crystallographic planes of alumina in the presence of water vapour.

v. As oxidation proceeds, up to ~1/4 of the Al required to grow the oxide layer is also obtained from depleting the bulk Cr_2AlC below the carbide, in addition to that obtained from the decomposition reaction. The GB diffusion of O ions through the large-grained inner alumina is the slowest and hence rate-controlling step, resulting in the observed parabolic kinetics of oxidation.

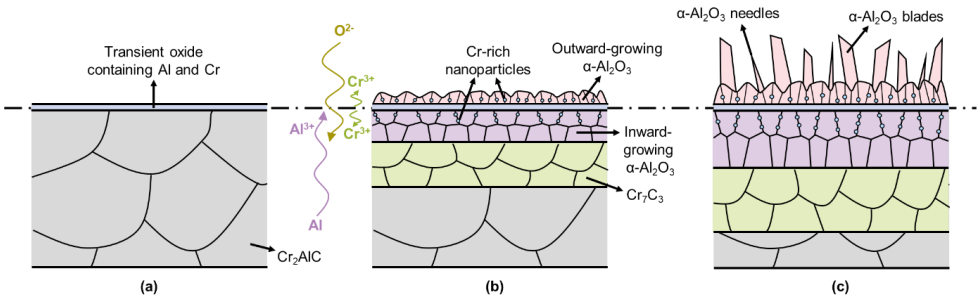

Fig. 5.31: Proposed mechanism of the oxide scale formation on Cr_2AlC: (a) initial formation of transient oxide enriched in Cr, (b) formation of a stable α-Al_2O_3 layer with both inward and outward-growing components and (c) formation of α-Al_2O_3 needles and blades on the surface with increase in oxidation time.

5.10 Summary

In this work, the oxidation behaviour of Cr_2AlC at 1000 °C and 1200 °C in a humid atmosphere was studied and a possible oxidation mechanism is proposed. At both these temperatures, the steady state oxidation shows parabolic behaviour, which indicates that the rate of oxide formation is controlled by the diffusion of Al and O ions. Although it has been shown in other studies that the oxidation behaviour of Cr_2AlC is better described by cubic kinetics [26], it should be noted that the oxidation times in the present study (up to 48 h) are quite short compared to typical long-term oxidation studies, which could be up to thousands of hours long. Hence, this is still in the active part of the oxidation process, and at longer times alumina grain growth may come into play and decelerate the kinetics.

A continuous bilayer α-Al_2O_3 scale is formed in the oxidation process, which consists of an outward-growing layer consisting of small, platelet-like grains, and an inward-growing large-grained layer. There is also a transient oxide region between these two layers rich in Cr. Needle-like and blade-like structures grow on the surface of the oxide with increase in oxidation time. Below the oxide a porous Cr_7C_3 layer forms due to decomposition of Cr_2AlC. All the layers emerge at the initial stage of oxidation and only grow in thickness with oxidation time without qualitative changes.

The formation of the oxide and carbide occurs simultaneously. Al needed to form the alumina layer comes primarily from the decomposition of Cr_2AlC into Cr_7C_3, with up to ~1/4 obtained from the depletion of Al from the bulk Cr_2AlC underneath. However, Cr_2AlC only tolerates up to ~1 at.% of Al depletion before decomposing. This behaviour is different from classical alloy oxidation, where the formation of pronounced depletion zones below the oxide are typically seen. The formation of voids in the carbide can be explained based on the mismatch in the volumes of carbide formed and the Cr_2AlC it is formed from.

Al diffuses preferentially via GBs in Cr_2AlC to form the oxide, and through the bulk in Cr_7C_3. Factors that affect GB diffusion, such as segregating elements or evolution in grain size, may affect the diffusion of Al through the Cr_2AlC but not through the carbide. However, both these processes do not seem to influence the oxidation rate. The GB diffusion of O through the inner large-grained alumina subscale is assumed to be the rate-controlling step of oxidation. This alumina subscale is free from Cr, C or any impurities both at GBs and in the bulk as evidenced by APT, so the results of this work can be considered as characteristic of pure Cr_2AlC oxidation.

There are also still some open questions regarding the proposed oxidation mechanism, such as the processes responsible for the needle and blade-like alumina formation or

the influence of porosity. These aspects do not however seem important for the oxidation kinetics, but can help to give a more complete picture. In addition, the precise effect of humidity on the rate and mechanism of oxidation is not clear from this study. In the future, a similar analysis of the oxidation of Cr_2AlC in a dry atmosphere could also be performed as a comparative study. Isotope tracer experiments performed in an ^{18}O-labelled water vapour ($H_2{}^{18}O$) atmosphere combined with APT could also provide more clarity on the possible diffusion pathways and oxidation mechanisms in a humid atmosphere, not only for Cr_2AlC but also for oxidation-resistant materials in general.

Chapter 6 Oxidation Mechanism of W-Cr-Y

6.1 Introduction

In this chapter, the effect of Y addition on the oxidation behaviour of W-Cr alloys is analysed. Firstly, the different aspects in which the oxidation resistance is improved in the ternary W-11.4Cr-0.6Y (in wt.%) alloy as compared to the same alloy without Y (W-11.4Cr) are investigated. Secondly, the reasons for these effects are examined by performing a two-step oxidation experiment using ^{18}O as a tracer, combined with the use of APT to look into the distribution of oxygen and yttrium in the oxide scale at the nanoscale. APT is also used to look at the distribution of Y in the mechanically alloyed powder, to clarify at which stage of the synthesis process oxygen uptake occurs, which can influence the distribution of yttria in the sintered alloy, which can in turn affect the oxidation behaviour.

6.2 Synthesis of W-Cr and W-Cr-Y

The procedure and parameters for the synthesis of standard bulk W-11.4Cr-0.6Y alloys were optimized by Klein *et al.* [44], which are followed in this study as well. The same process parameters were used for the synthesis of the binary alloy W-11.4Cr so that the only differing factor in both these alloys is the addition of 0.6 wt.% Y. The manufacturing process first involves the mechanical alloying of elemental powders, followed by consolidation using field-assisted sintering technique/spark plasma sintering (FAST/SPS). The procedure is described in detail below.

Elemental powders of tungsten (average particle size, APS 4 μm, 99.9% pure), chromium (APS 45 μm, 99.7% pure) and yttrium (APS 500 μm, 99.9% pure) were mixed in the desired ratio (68.9W-31.1Cr in at.% for the binary and 67.9W-31.1Cr-1.0Y in at.% for the ternary). The powder mixtures were milled in a planetary ball mill (Retsch PM400 MA, Retsch GmbH, Germany) for 60 h at 198 rpm under Ar atmosphere. Tungsten carbide milling balls were used, and the inner wall of the milling jar was coated with tungsten carbide as well. The ball to powder ratio was 5:1. **Fig. 6.1** shows an SEM image of the milled W-Cr-Y powder.

After ball milling, 25 g of the mechanically alloyed powder was placed into a graphite mold with diameter 20 mm and a hydraulic press was used to create a green compact. This was then consolidated using the FAST/SPS facility (FCT-HPD5, FCT Systeme GmbH, Germany) under vacuum and the application of a uniaxial pressure of 50 MPa throughout the process. It was heated up at a rate of 200 K/min until a maximum temperature of 1460 °C with no isothermal holding time at this temperature. The

resulting ingots are well densified, having a relative density of over 98%, which is measured using the Archimedes principle.

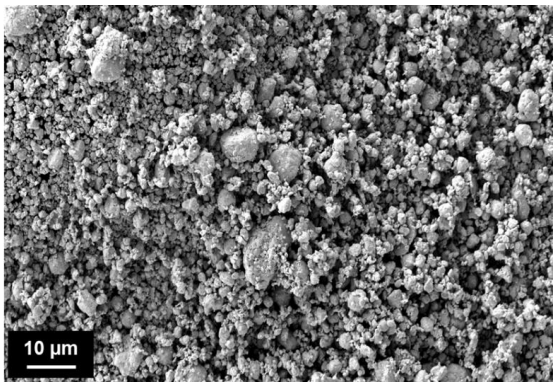

Fig. 6.1: SEM image of mechanically alloyed powder of W, Cr and Y which is then sintered to produce W-11.4Cr-0.6Y.

6.3 Microstructure of as-sintered alloys

The W-Cr binary phase diagram in **Fig. 6.2** shows that when 11.4 wt.% Cr is added to W and sintered at a maximum temperature of 1460 °C, it remains in the miscibility gap, i.e., both the Cr-rich solid solution (αCr, W) and W-rich solid solution (αW, Cr) phases can be formed. Based on the lever rule, the predominant phase formed is the W-rich (αW, Cr) phase. Modelling studies have shown that the addition of up to 2 at.% Y to W-11.4Cr does not significantly alter the enthalpy of mixing of the system [206], hence the phase formation in the ternary alloy is expected to be similar to the binary system.

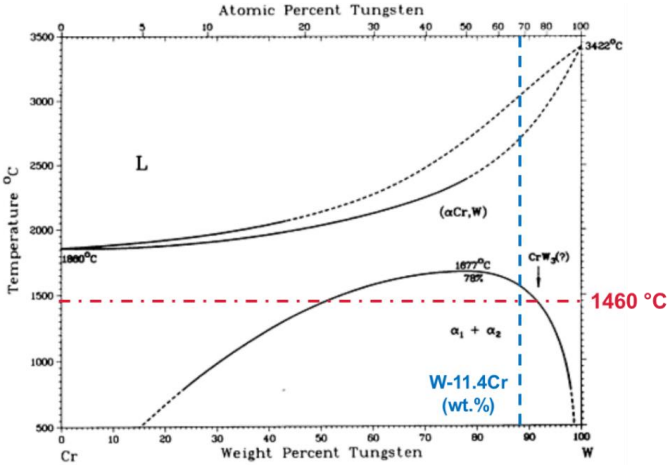

Fig. 6.2: W-Cr phase diagram [207] with the composition of the alloy and sintering temperature indicated.

In the as-sintered state, as shown in **Fig. 6.3** and **Fig. 6.4**, both the binary and the ternary alloys consist primarily of the W-rich phase (αW, Cr). In both alloys the GBs are decorated with oxide particles. In the binary alloy, these are Cr-O particles, as seen in the EDX maps in **Fig. 6.3**(b). A STEM-EDX study on the ternary alloy has shown that the particles present in this alloy are Y-O particles [208].

The areal density of these particles also varies: the density of Cr-O particles in the binary W-Cr system is ~9 particles/μm^2, being much lower than that of the Y-O particles in the ternary W-Cr-Y, which is ~29 particles/μm^2. Another key difference in the microstructure is the grain size, which is 300-400 nm in the binary but only ~180 nm big in the ternary alloy.

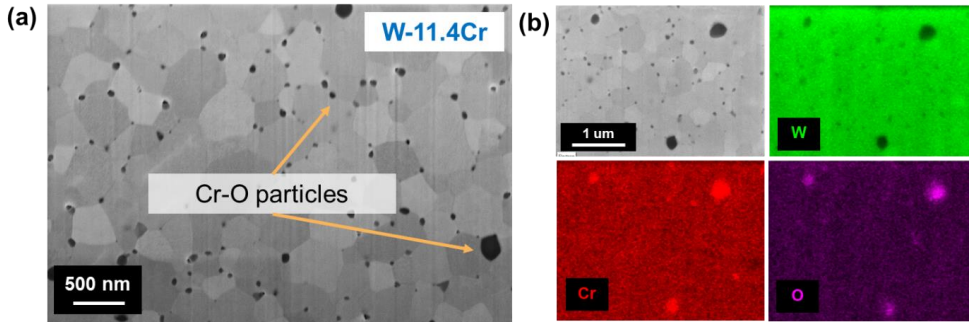

Fig. 6.3: (a) SEM image of the as-sintered microstructure and (b) EDX maps of the binary alloy W-11.4Cr.

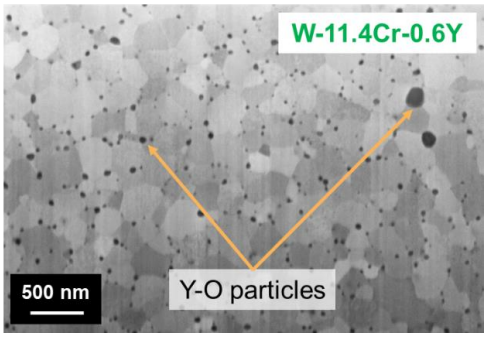

Fig. 6.4: (a) SEM image of the as-sintered microstructure of the ternary alloy W-11.4Cr-0.6Y.

The formation of oxygen-rich particles at the GBs raises the question of how and why oxygen is found in this system to begin with, since the synthesis process starts with elemental powders of W, Cr and Y. Some amount of oxygen uptake could possibly happen during milling (if trace amounts of oxygen are present), transport of milled powders or during sintering. To investigate this further, APT analysis of the mechanically alloyed powder was performed.

6.4 APT analysis of mechanically alloyed powder of W-Cr-Y

APT specimens were prepared from mechanically alloyed powder particles of W-Cr-Y. Particles ~2 μm big, such as the one marked in **Fig. 6.5**, were chosen so that they can be easily mounted on the posts of the micro-tip coupon, which also have a standard diameter of 2 μm. Measurement parameters of 200 kHz pulse rate, 100 pJ LPE, 0.5% DR and specimen temperature of 50 K were used, which are the same parameters used previously for the APT analysis of as-sintered W-Cr-Y samples. However, since specimens made from powder particles are more susceptible to fracture during the measurement, the LPE was increased to 150 pJ to reduce the stress on the specimen and increase specimen yield. LPEs higher than this value resulted in overheating of the specimen tip and produced a non-uniform detector event histogram.

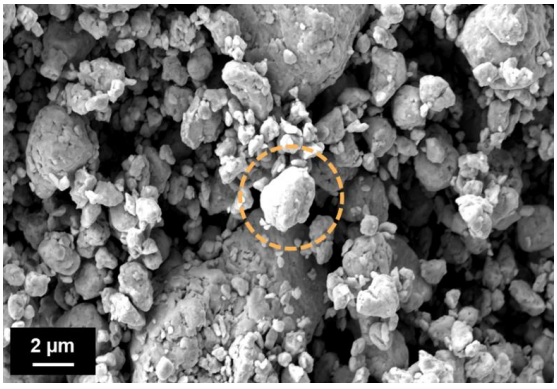

Fig. 6.5: A representative powder particle of size ~2 μm that was used for APT analysis.

The elemental map obtained from the powder particle is shown in **Fig. 6.6**(a). The formation of Y-O rich clusters can be seen, indicating that there is already an uptake of oxygen at this stage, which starts to bond with Y since it has a high affinity for O. The bulk composition of the powder particle analysed using APT in **Table 6.1**, shows the presence of 1.7 at.% O, even more than the amount of Y which is measured to be 0.8 at.%. Hence, it may be more accurate to consider the alloy to be a quaternary system rather than ternary since it has a non-negligible amount of O, which could be an important point when it comes to modelling studies. However, in this thesis this system containing Y is still referred to as the ternary alloy.

Fig. 6.6(b) shows the concentrations of various elements in the matrix and the Y-O clusters. Since the field required for the evaporation of these clusters is different from that of the surrounding matrix, this gives rise to an APT artefact known as the local magnification effect. During reconstruction, this leads to the matrix ions being calculated to have originated from the region belonging to the clusters instead of their original positions. The smaller the clusters are, the larger this effect is, and the chemical

composition of these clusters cannot be accurately measured as a result. The presence of W and Cr within the clusters in **Fig. 6.6**(b) can be a result of this artefact. However, the ratio of Y and O within the clusters is close to equal. This indicates that yttrium is not fully oxidised into the stable oxide Y_2O_3 at this stage.

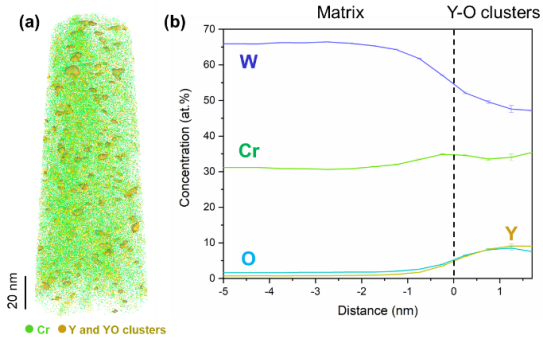

Fig. 6.6: (a) APT elemental map from a powder particle after mechanical alloying used for the synthesis of W-11.4Cr-0.6Y (b) proximity histograms showing variation in concentrations of W, Cr, Y and O across the interface of the Y-O clusters and the matrix.

Table 6.1: Bulk composition of W-11.4Cr-0.6Y powder particle (in at.%) obtained by APT analysis

Element	Concentration (at.%)
W	64.9
Cr	32.0
Y	0.8
O	1.7

6.5 Effect of Y on oxidation behaviour

The main focus of this section is to investigate how the addition of Y influences the oxidation resistance of W-Cr alloys. Since the amount of Cr as well as the preparation route of both the binary and ternary alloys are kept the same, with the only difference being the addition of 0.6 wt.% of Y in the ternary alloy, the effect of any other factors on oxidation behavior could be eliminated. The two alloys were oxidized under the same conditions and the differences in oxidation kinetics and behavior at the microstructural scale were analyzed, through which the effect of Y on oxidation behavior could be inferred.

6.5.1 Oxidation behaviour and kinetics

Fig. 6.7 shows thermogravimetric analysis plots obtained from the isothermal oxidation of the binary and ternary alloys at 1000 °C in a synthetic air atmosphere with 70% relative humidity at 25 °C. The mass gain of the binary alloy rapidly increases

with time, whereas the ternary alloy shows a much slower rate of oxidation, with the mass gain being ~0.8 mg/cm^2 even after 20 h. By having a much slower rate of oxidation and no indication of spallation, the ternary alloy seems to show a better oxidation resistance behavior.

In order to quantify the rate of oxidation, the data was first fit to a power law equation (as described in Section 2.1.3.1) of the general form

$$\Delta m = k \cdot t^n \qquad \text{(Equation 6. 1)}$$

Here, Δm is the mass gain per unit area in mg/cm^2 and t is the time in seconds. The scale growth exponent n determines the type of the oxidation kinetics. The value of the growth exponent n is 1.27 for the binary and 0.92 for the ternary, indicating that in this time scale, both the alloys show close to linear oxidation kinetics, with the binary showing even faster than linear kinetics.

The linear growth rate of the binary alloy is 5.64 × 10^{-4} mg·cm^{-2}·s^{-1} and is 1.1 × 10^{-5} mg·cm^{-2}·s^{-1} for the ternary alloy. Hence, the addition of Y results in an apparent 50-fold decrease in the oxide growth rate as compared to the binary alloy.

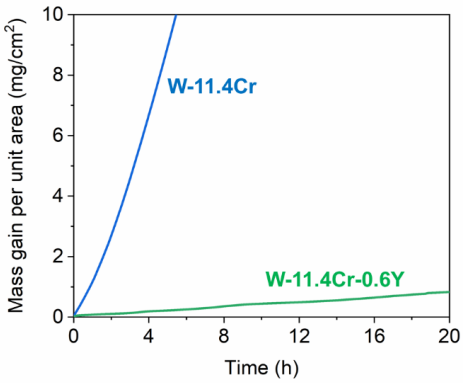

Fig. 6.7: Mass gain curves of the binary (blue) and ternary (green) alloys oxidized at 1000 °C.

6.5.2 Morphology and microstructure of oxide scale

6.5.2.1 Appearance of samples after oxidation

In addition to the TGA curves, the improved oxidation resistance with the addition of Cr and Y to tungsten is also quite evident when looking at the morphology of bulk samples after they are oxidized under the same conditions. **Fig. 6.8** shows the comparison between cuboidal samples of pure W, W-Cr and W-Cr-Y, all oxidized at 1000 °C. The oxide scale formed on W, having a Pilling-Bedworth ratio of 3.4 [29] cannot serve a protective function since the oxide rapidly grows and expands into a volume more than three times that of the metal it is formed from. The binary alloy

shows an improvement over pure W, but the amount of oxide formed is still large, especially at the sample edges, and shows there a tendency for spallation. On the other hand, the ternary alloy still retains the original cuboidal geometry after oxidation, indicating that the formed oxide layer is slow-growing and dense.

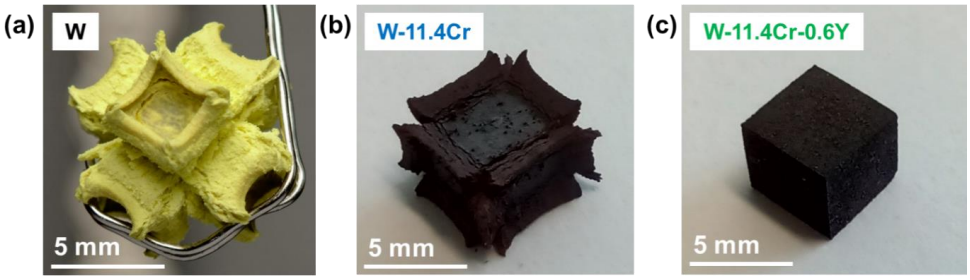

Fig. 6.8: Cuboidal samples oxidized at 1000 °C of (a) pure W for 10 h (Reprinted from [209] with permission from Elsevier), (b) W-Cr for 20 h and (c) W-Cr-Y for 20 h.

6.5.2.2 Microstructure of surface and cross-section

After 8 h of isothermal oxidation at 1000 °C in dry air, a complex oxide scale is formed in both cases and consists of various phases including chromia, WO_3 and the mixed oxides Cr_2WO_6 and $CrWO_4$, which were determined based on XRD patterns shown in **Fig. 6.9**. Although similar phases are formed, there are several differences in the microstructure of the oxide scales and the distribution of these phases in the binary and ternary alloys, which is determined based on the elemental distribution obtained using EDX.

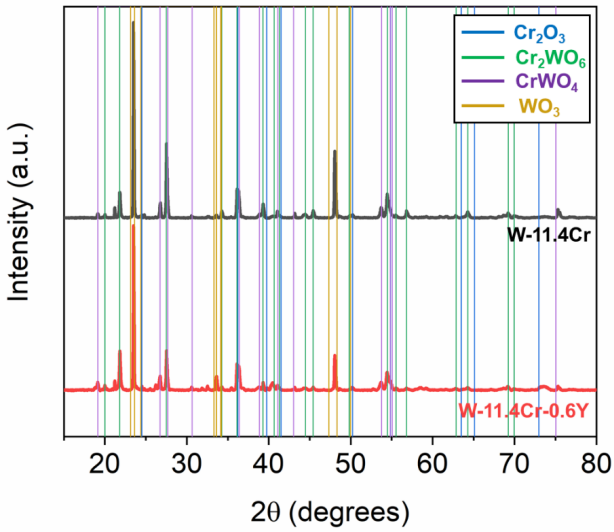

Fig. 6.9: XRD patterns of the binary W-Cr and ternary W-Cr-Y alloys oxidized for 8 h at 1000 °C in dry air. The overlay lines show the major peak positions of chromia, mixed oxides and tungsten oxide, based on [210–213].

Fig. 6.10 shows the surface and cross-sectional microstructures of the oxide scale formed on the binary W-11.4Cr alloy after 8 h of isothermal oxidation at 1000 °C in dry air. A magnified image of the oxide scale cross-section is shown in **Fig. 6.11**(a), and the different oxide phases present are labelled using the EDX line scan in **Fig. 6.11**(b). The surface consists of the mixed Cr_2WO_6 oxide, about 1 µm thick, containing some scattered, small inclusions of Cr_2O_3. Below the outermost layer of Cr_2WO_6, the oxide scale consists of a layer of $CrWO_4$, a porous WO_3 region with some mixed W-Cr-O inclusions, and a Cr-enriched oxide region close to the interface with the alloy. Internal oxidation occurs in the alloy close to the alloy-oxide interface, as shown in **Fig. 6.10**(b).

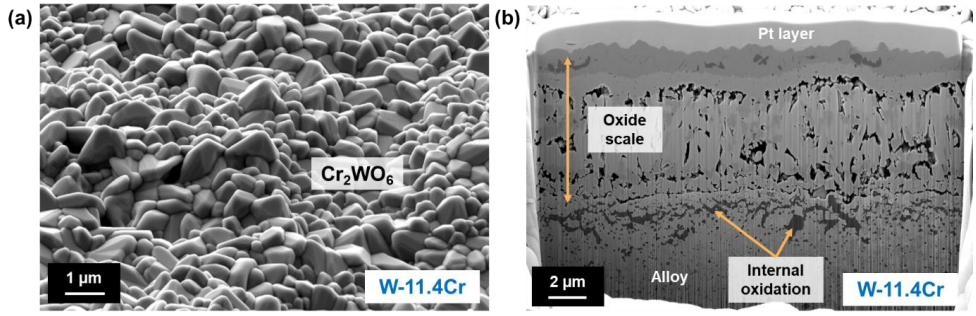

Fig. 6.10: SEM images of (a) the surface and (b) cross-section of the binary W-11.4Cr alloy oxidized for 8 h at 1000 °C.

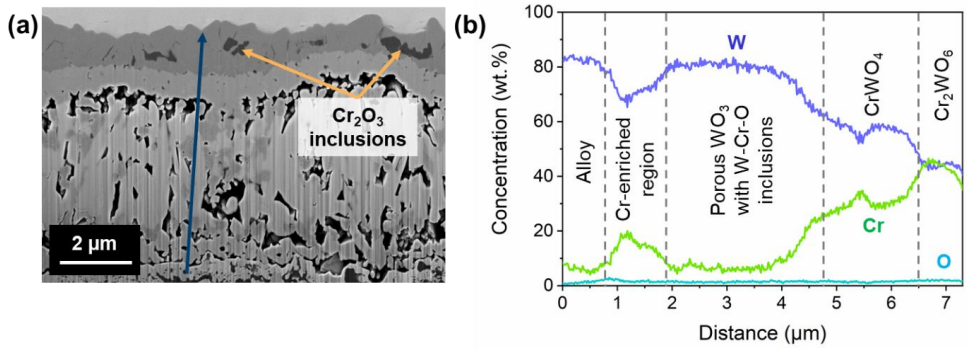

Fig. 6.11: (a) SEM image of the cross-section of the oxide scale of the oxidized binary alloy and (b) EDX line scan showing the elemental concentrations along the dark blue arrow in (a).

In contrast, under the same oxidation conditions, a continuous protective Cr_2O_3 layer of ~400 nm thickness is formed on the ternary alloy, along with large particles of a mixed W and Y-containing oxide present on the surface, as seen in **Fig. 6.12**. The oxide scale in the ternary alloy has more layers than in the binary alloy but follows a similar pattern – below the continuous chromia layer, Cr_2WO_6 and $CrWO_4$ layers, WO_3 containing mixed oxide inclusions, and again a Cr-enriched oxide region are present, as shown in **Fig. 6.13**. In general, in both alloys, starting from the outermost layer, the Cr-content gradually decreases from layer to layer, before rising once again near the

oxide-alloy interface. However, the mixed oxide region here is less porous than in the binary alloy. Regions of internal oxidation, resulting in the formation of chromia within the alloy, are also found in the ternary alloy as seen in **Fig. 6.12**(b).

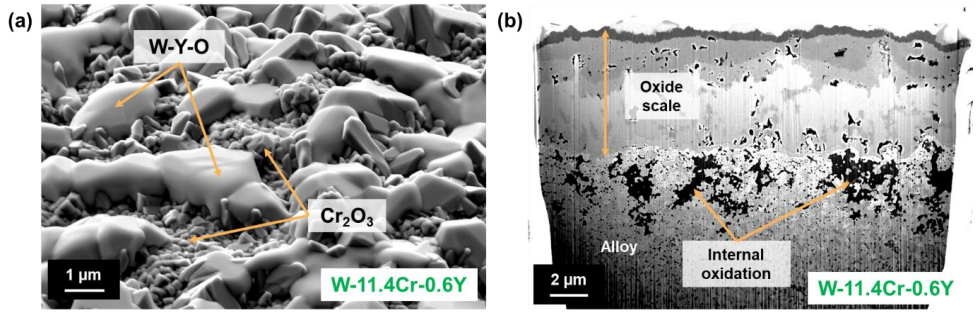

Fig. 6.12: SEM images of (a) the surface and (b) cross-section of the ternary W-11.4Cr-0.6Y alloy oxidized for 8 h at 1000 °C.

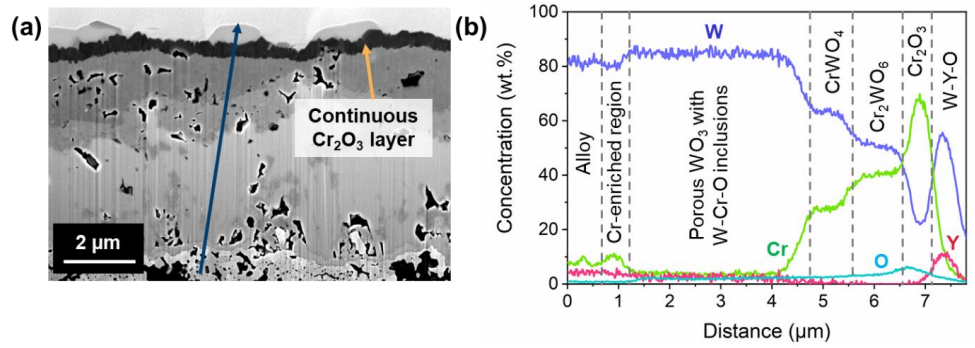

Fig. 6.13: (a) SEM image of the cross-section of the oxide scale of the oxidized ternary alloy and (b) EDX line scan showing the elemental concentrations along the dark blue arrow in (a).

6.5.3 Discussion

6.5.3.1 Effect on grain growth

In the as-sintered state of the ternary W-Cr-Y alloy, Y is found in the form of oxide particles decorating the alloy GBs. The areal particle density of the Y-O particles is ~3 times that of the corresponding Cr-O particles in the binary alloy. Due to the GB pinning effect [214] of the large number of Y-O particles, the grain growth is restricted, which results in a finer grain size as compared to the binary W-Cr alloy. A finer grain size corresponds to a larger available GB area, and is a beneficial aspect for oxidation resistance when the Cr diffusion needed to form the protective oxide layer proceeds primarily via alloy GBs. Improved oxidation performance with smaller grain size has been observed before in the W-Cr-Y system, attributed to an enhancement in overall Cr transport via the alloy GBs to form the protective Cr_2O_3 layer [44].

6.5.3.2 Effect on mixed oxide scale formation

After oxidation, the current study shows that the formation of a complex mixed oxide scale occurs in both the binary and the ternary alloys. In previously published studies of the bulk ternary alloy W-11.4Cr-0.6Y, with a grain size of ~200 nm and less, oxidation was shown to result in the formation of a continuous chromia layer, along with internal oxidation, with no mixed oxide formation even after oxidation times of up to 44 h [44].

However, after analyzing six different batches of the ternary W-Cr-Y alloy having the identical composition, it was observed that mixed oxide formation indeed occurs in samples from all those batches, both in dry and wet atmosphere, as shown in **Table 6.2**. Formation of a complex scale with mixed oxides is much more common than formation of a single-layer Cr_2O_3 scale, which was observed only in a few early experiments in two batches and could not be reproduced even with the identical composition, similar grain size, Y-O particle distribution and Cr-content in the as-sintered state (as measured by EDX). Therefore, the former microstructure showing mixed oxides seems to be a typical scenario for the oxidation of W-11.4Cr-0.6Y alloy.

Some possible reasons for the formation of a single-layer chromia scale observed in previous studies have been proposed. These include the use of purer elemental powders in early studies, a different ball milling device, and differences in the settings of the TGA during oxidation. However, this issue is being investigated and the real reason for this behavior has not been determined yet.

Table 6.2: Summary of microstructures of oxidized ternary W-11.4Cr-0.6Y samples from different batches. Mixed oxide microstructures are marked with a blue background.

	Ingot number, as-sintered microstructure	Temperature	Time	Atmosphere	Sample number, cross-section
1	FAST2060 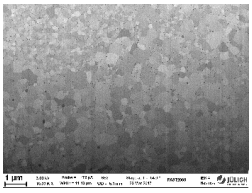 (bimodal grain structure)	1000 °C	44 h	Synthetic air, 70% RH	03 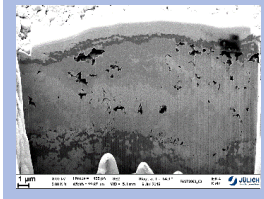
2	FAST2061 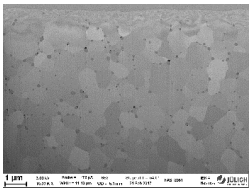 (large (~1 μm) grain size)	1000 °C	44 h	Ar-O_2, dry	04 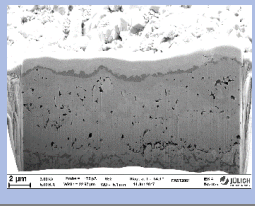

		1000 °C	20 h	Synthetic air, 70% RH	07 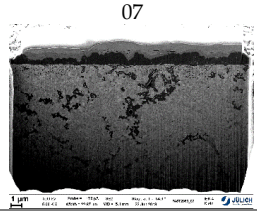
3	FAST2063 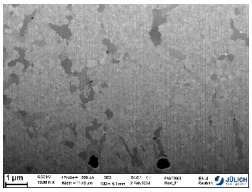	1000 °C	20 h	Ar-O_2, dry	09 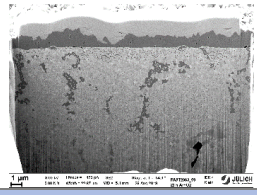
		1000 °C	8 h	Ar-O_2, dry	Rest-01 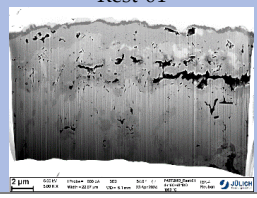
4	FAST2064 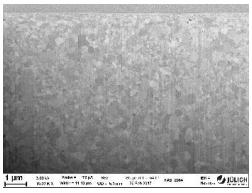	1000 °C	44 h	Ar-O_2, dry	01 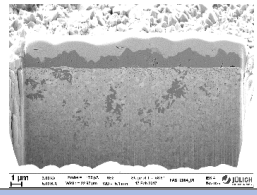
		1000 °C	3 h	Ar-O_2, dry	05 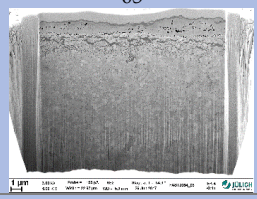
5	FAST4043 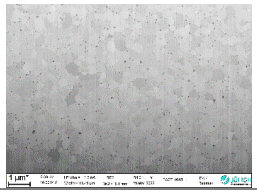	1000 °C	8 h	Ar-O_2, dry	Flat-01 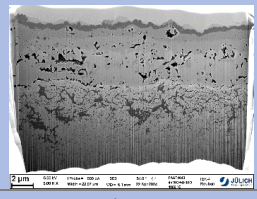
6	FAST4608 (this work) 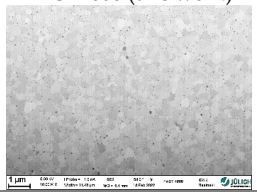	1000 °C	8 h	Ar-O_2, dry	Flat-01 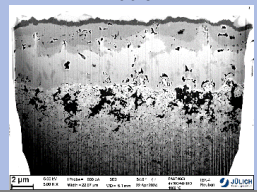

	1000 °C	20h	Synthetic air, 70% RH	05 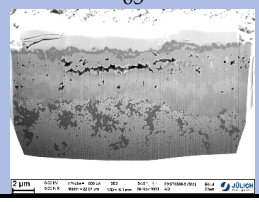

6.5.3.3 Effect on chromia formation

Although a complex oxide scale with mixed oxides is formed, the presence of Y seems to play a crucial role in enabling the formation of a continuous, thin chromia scale in the ternary alloy, which can then act as a protective, passivating oxide layer, reducing the rapid formation of mixed oxides and preventing the possible sublimation of the underlying tungsten oxide. In the case of the binary W-Cr alloy, the presence of small chromia inclusions in the outermost oxide layer suggests that some chromia does start to form, but is unable to form a continuous layer and eventually the formation of a much thicker Cr_2WO_6 layer dominates. From the TGA data of the binary alloy it can be seen that such a mixed oxide configuration grows rapidly, and does not show a passivating behavior.

6.5.3.4 Elimination of the edge effect

The predominant growth of the oxide in the binary alloy emerges at the edges and corners, i.e., in the regions with high local curvature, potentially due to higher local stresses in these regions. This behavior is also typically seen in the oxidation of pure W. It should be noted that the thickness of the entire oxide scale in the flat surface of the binary sample is only slightly more than that in the ternary alloy, as seen in **Fig. 6.13**(b) and (e). Although the Cr_2WO_6 layer formed is relatively stable up to 1100 °C [215] and can provide some protection against the sublimation of the tungsten oxide below [140], any parts of the material with high local curvature seem to be potential weak regions, where the oxide can easily spall off and expose the underlying tungsten oxide to the atmosphere. Due to the significant edge effect seen in the oxidation of the binary alloy, the oxidation rate can also be expected to be different from the measured value of 5.64×10^{-4} mg·cm^{-2}·s^{-1} in this study if a larger sample or a different geometry is used. The addition of Y also seems to eliminate this edge effect by enabling the formation of a continuous chromia layer.

6.5.3.5 Effect on sublimation of oxides

Apart from the sublimation of tungsten oxide, which should be avoided, it is also well known that at temperatures ≥ 1000 °C, in the presence of water vapor, chromia can form volatile hydroxides [34,203]. Y addition could have an effect on this as well, since

it results in the formation of large W-Y-O oxide particles on the surface, even after 8 h of oxidation, which could suppress this volatilization of chromia and increase the stability of the chromia layer. However, the suppression of chromia sublimation will be effective only if the W-Y-O oxide is more stable than chromia above 1000°C in a humid atmosphere. Although the composition of this phase could not be determined in this work, the possible phases in the Y_2O_3-WO_3 system, such as $Y_2W_3O_{12}$ and Y_2WO_6 have melting points greater than 1000 °C [216], hence it is expected to be thermally stable during oxidation.

6.5.3.6 Effect on adherence of oxide scale

The stability of the inner layers of the oxide scale is also important to consider when looking at the adherence of the oxide scale to the underlying material. A porous tungsten oxide layer is formed in both cases, but with the addition of Y the oxide scale shows lower porosity, which could be beneficial for the adherence of the oxide scale to the underlying alloy. Therefore, the addition of Y seems to have a positive effect on increasing the adherence of the oxide scale.

6.6 Mechanism of the reactive element effect of Y

The benefits of adding Y to the W-Cr system, as described in the preceding section, seem to align with the proposed mechanisms of the reactive element effect of Y on chromia scales, such as the increased adherence of the oxide scale due to a reduction in porosity, and a marked reduction in the oxide growth rate and thickness, enabling the growth of chromia to dominate and form a protective layer. Based on studies on other chromia-forming alloy systems, these beneficial effects have been determined to be likely due to the segregation of Y at oxide GBs [49]. However, in order to study the exact mechanism of this effect in the W-Cr system, nanoscale analysis of the oxide and alloy GBs and interfaces is necessary. Hence, a two-step oxidation experiment using ^{18}O isotope was performed, followed by the analysis of Y and O isotope distribution using APT, described in detail below.

6.6.1 Two-step oxidation experiment using ^{18}O isotope

As described earlier in Section 2.1.6, one of the primary ways by which a reactive element like Y improves the oxidation resistance of chromia formers is by segregating at chromia GBs, thus affecting ionic diffusion and altering the overall mass transport. This results in a change in the predominant growth direction of the oxide, which normally grows in the outward direction, to the inward direction. One of the best ways to study the oxide growth direction is by using ^{18}O as a tracer to track oxide growth in a two-step oxidation experiment [217].

Fig. 6.14 shows the schematic of this experiment. In the first stage of oxidation, the material is oxidized in an atmosphere containing standard oxygen, i.e., the primary isotope (99.8%) is ^{16}O. Here, an atmosphere of Ar with 20% standard oxygen was used. The oxide formed in this stage will be rich in ^{16}O. In the second stage, oxidation is done in an atmosphere containing ^{18}O as the major isotope of oxygen (with a purity of 97%) i.e. in Ar-20%$^{18}O_2$. The new oxide formed in this stage will be rich in the ^{18}O isotope. If the new ^{18}O-rich oxide grows on top of the previously grown oxide, this indicates that the oxide grows in the outward direction. On the other hand, if the ^{18}O-rich oxide is found below the existing oxide, this indicates that the oxide grows in the inward direction. In case of an oxide scale where growth is both in the inward and outward directions, the new oxide will be found both on top of and below the existing oxide, and the thickness of new oxide in these regions can indicate which of the two is more dominant.

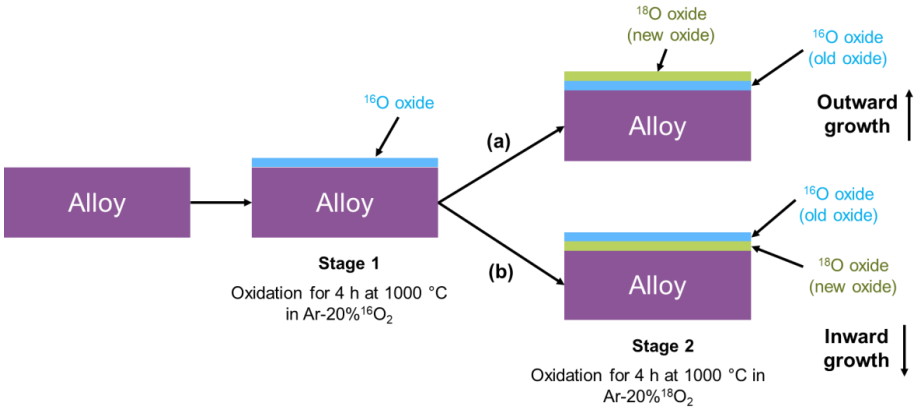

Fig. 6.14: Schematic of the two-step oxidation experiment using ^{18}O isotope as a tracer, showing the formation of ^{16}O and ^{18}O-rich oxides in case of (a) outward growth and (b) inward growth.

The two-step oxidation experiment was performed on both the W-Cr and W-Cr-Y alloys, the experimental procedure for which was described in Section 4.2.2. APT analysis was performed on the chromia scale and the mixed W-Cr oxide layer formed in the ternary alloy after two-step oxidation to study the chemical distribution of Y and the oxygen isotopes at the nanoscale.

6.6.2 APT analysis of ^{18}O distribution

The sample used for APT analysis following two-step oxidation had previously been oxidised for 20 h in standard Ar-20%O_2. This oxidised sample was ground to remove the oxide layer, with the removal of ~50 µm of material from all sides of the sample to make sure any regions with internal oxidation were fully removed. **Fig. 6.15** shows the cross-section of the oxide scale formed on this sample after the two-step oxidation

experiment. After a total oxidation time of 8 h, the thickness of the entire oxide scale is ~6 μm. The APT specimens were prepared using the standard lift-out procedure from the surface, i.e., they only contained material from the first ~2 μm of the sample. This part of the oxide layer contains ~400 nm of chromia and the rest is Cr_2WO_6, as seen in the figure, with the occasional presence of W-Y oxide on the surface. Therefore, only the chromia layer and Cr_2WO_6 could be analysed using APT, marked in **Fig. 6.15**.

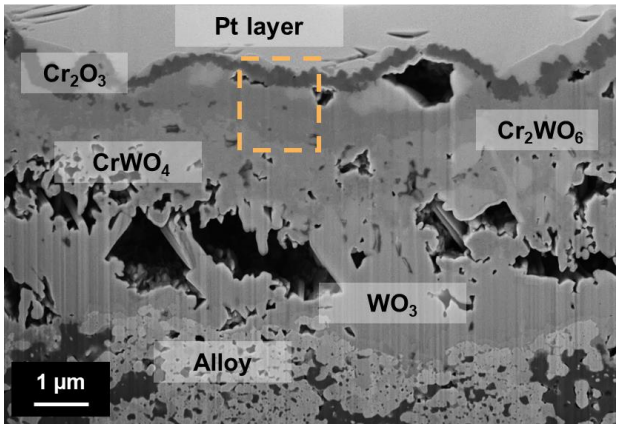

Fig. 6.15: SEM image of cross-section of W-11.4Cr-0.6Y sample after two-step oxidation experiment. The box indicates the region which could be analyzed using APT using standard lift-out specimens.

The parameters used for the measurement were 250 kHz pulse rate, 50 pJ LPE, 0.5% DR and a specimen temperature of 50 K. This is based on studies previously done on oxidised W-Cr-Y. When measuring the mixed oxide region, the pulse rate was lowered down to 125 kHz to avoid the wrap-around effect.

6.6.2.1 Mass spectrum analysis

Care must be taken when identifying ^{18}O in the mass spectrum after an APT measurement since some peaks which may be formed due to ^{18}O ion evaporation could also have a contribution from ^{16}O-containing ions. As a simple example, consider the peak at 18 Da. Although this peak is formed from the evaporation of $^{18}O^+$ ions, there is also a considerable contribution to this peak from the evaporation of the $H_2{}^{16}O^+$ molecular ion. The latter is usually formed during the APT analysis of oxides due to the presence of residual H_2 molecules in the analysis chamber, which is present even under ultra high vacuum and low temperatures [218]. Therefore, this peak cannot be used for the determination of ^{18}O concentration, since it also has a large contribution from ^{16}O present in the water molecule, which could lead to misleading results.

Based on an evaluation of the possible ^{16}O and ^{18}O-containing ions that can be formed during the measurement of chromia and Cr_2WO_6, including complex ions formed with Cr and W, a set of peaks which form solely or predominantly from the evaporation of

^{16}O or ^{18}O-containing ions could be identified. These peaks were used for the labelling of ^{16}O and ^{18}O-rich regions in the elemental maps and composition analysis.

For example, **Fig. 6.16** shows a comparison of the mass spectrum of chromia where CrO^+ peaks are present. **Fig. 6.16**(a) shows the peaks present when oxidation is performed in normal air. The intensities of these four peaks correspond to the relative abundancies of the four stable isotopes of Cr. Since ^{52}Cr is the isotope of Cr with the highest abundance, the intensity of the peak at 68 Da is the highest. **Fig. 6.16**(b) shows the peaks present after a two-step oxidation experiment. Here, the peak at 70 Da is formed with a predominant contribution from $^{52}Cr^{18}O^+$, and two new peaks at 71 and 72 Da are also present, which are also formed due to ^{18}O-containing ions. Additionally, H has not been found bind to the complex metal-oxygen ions, hence these ions can be used to deconvolute ^{16}O from ^{18}O.

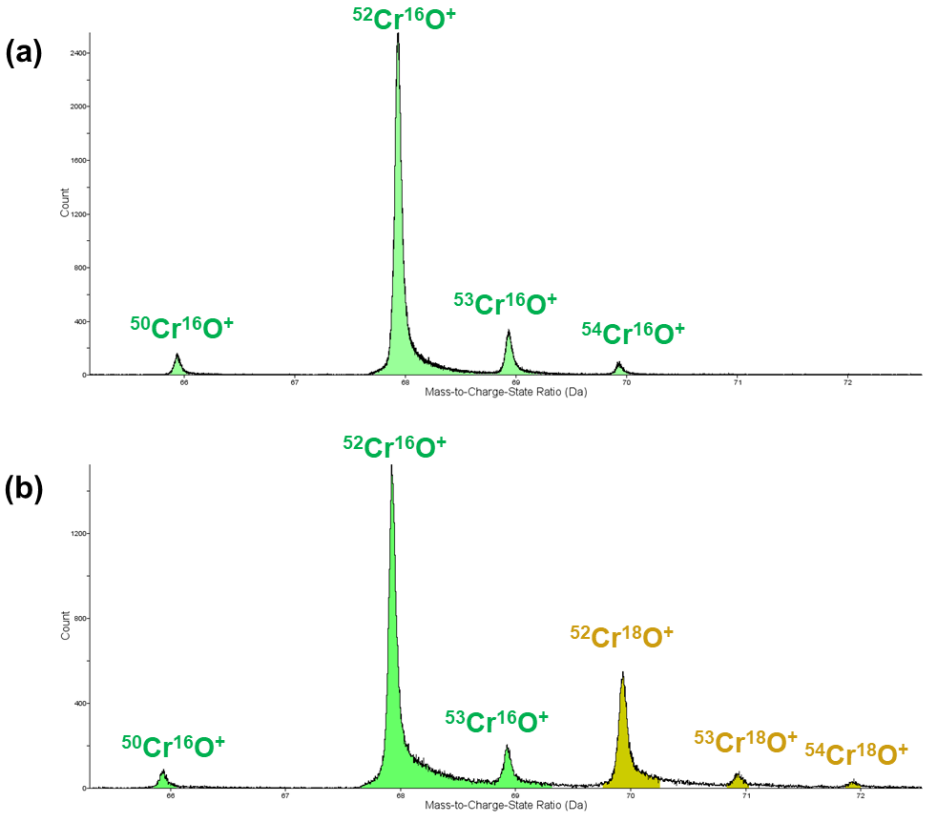

Fig. 6.16: Part of the mass spectrum after analysis of (a) chromia scale formed after oxidation in normal air and (b) chromia scale formed after two-step oxidation in ^{16}O and ^{18}O showing the formation of ^{18}O-containing ions.

6.6.2.2 Cr_2O_3 scale

Fig. 6.17(a) shows the APT elemental maps from the top part of the chromia scale. Multiple grains can be seen even in this relatively short dataset, indicating that the chromia grains are quite small, ~50 nm big in this part of the scale after 8 h of oxidation. **Fig. 6.17**(b) shows concentration profiles across a chromia GB. Y is found to segregate at chromia GBs, as is typically seen in oxide scales formed on alloys containing Y. The oxide is primarily made of ^{16}O, while ^{18}O is only present at the GBs, which indicates that the top part of the chromia layer grew during the first stage of oxidation.

The presence of ^{18}O at the GBs could be an indication of oxygen diffusion via oxide GBs during the second stage of oxidation. The bulk composition within a grain of chromia is shown in **Table 6.3**. About 2.7 at.% of ^{18}O is found inside the grain. However, this value may be overestimated due to the limitations in ranging the mass spectrum as described earlier.

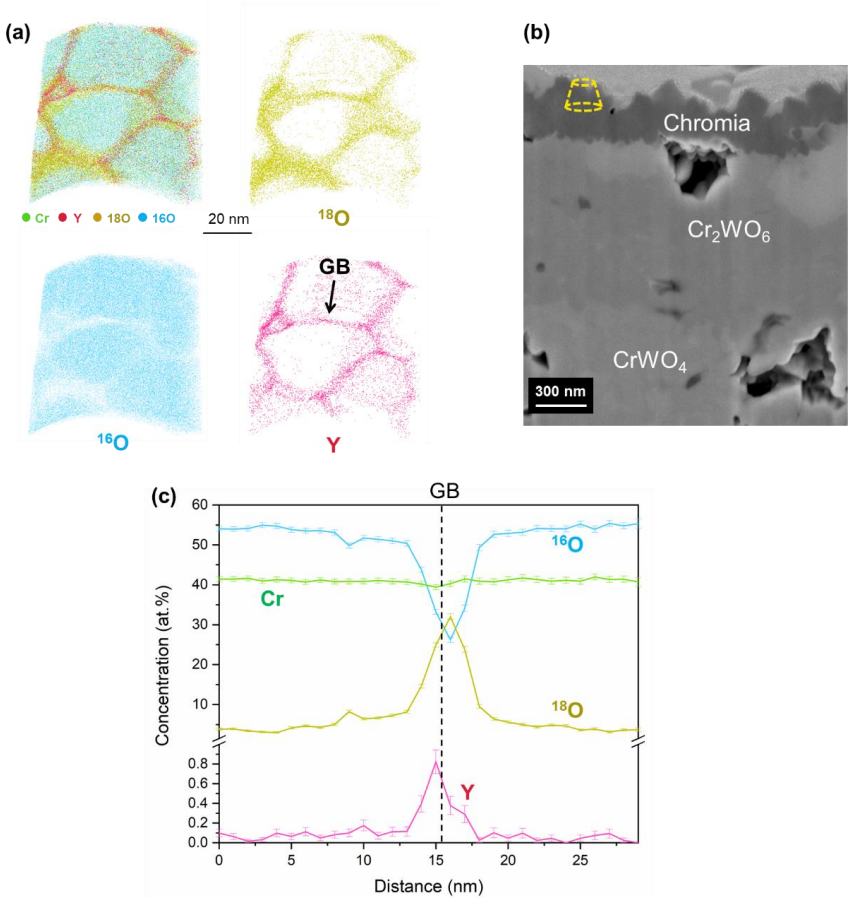

Fig. 6.17: (a) APT elemental maps from the top part of Cr_2O_3, as indicated in (b), (c) concentration profiles across the GB shown in (a).

Table 6.3: Bulk composition of grain interior of Cr_2O_3 (in at.%) obtained by the APT analysis

Element	Concentration (at.%)
Cr	42.0
^{16}O	55.1
^{18}O	2.7

6.6.2.3 Mixed oxide Cr_2WO_6

Fig. 6.18(a) shows APT elemental maps from the region of the mixed oxide Cr_2WO_6 very close to the chromia layer. Y segregation is seen at the oxide GBs here as well, and the mixed oxide grains are rich in ^{16}O. An interesting phenomenon of the nucleation of ^{18}O-rich grains of chromia at the GBs of the mixed oxide is observed.

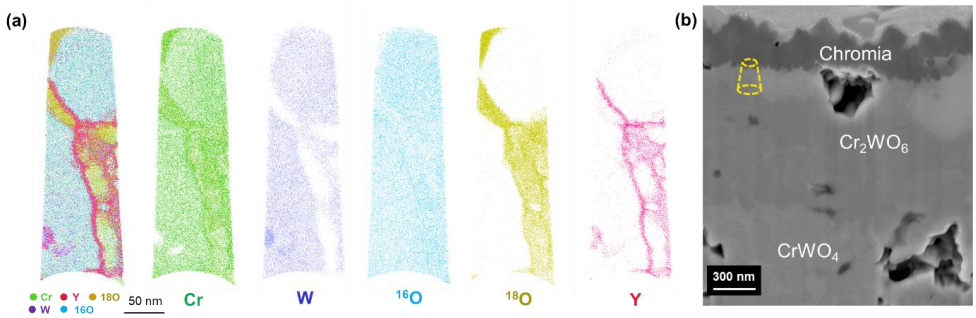

Fig. 6.18: (a) APT elemental maps from the part of the mixed oxide Cr_2WO_6 very close to Cr_2O_3, as indicated in (b).

Fig. 6.19(a), shows the APT elemental maps from the top of the Cr_2WO_6 layer. The grains are more equiaxed in some regions but columnar in others. Y segregation is seen at the GBs. Concentration profiles across a GB are shown in **Fig. 6.19**(b). The oxygen isotope distribution is similar to that of the top part of the chromia scale, where the grains are rich in ^{16}O, while ^{18}O segregates at the GBs. **Table 6.4** shows the bulk composition within a grain of the oxide, where it can be observe that the ratio of Cr to W is 2.2, indicating that the oxide could be non-stoichiometric due to the slightly increased amount of Cr.

The amount of ^{18}O is about 4 at.%, which is slightly more than that of the amount of ^{18}O found within a chromia grain. Although this value could also be an overestimate, this can still give an idea about the relative amounts of ^{18}O present in Cr_2WO_6 and chromia. Since the mixed oxide has a relatively higher amount of ^{18}O, this indicates that Cr_2WO_6 may be less impervious to bulk diffusion of oxygen than chromia.

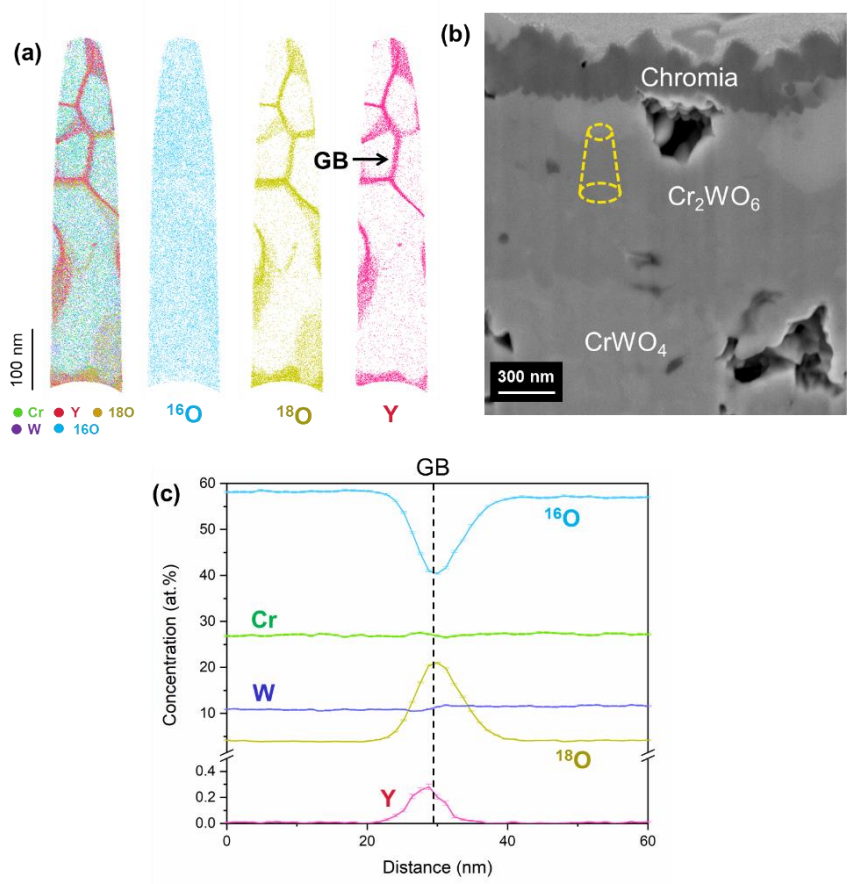

Fig. 6.19: (a) APT elemental maps from the top part of the mixed oxide Cr_2WO_6, indicated in (b), (c) concentration profiles across the GB shown in (a).

Table 6.4: Bulk composition of grain interior of Cr_2WO_6 (in at.%) obtained by the APT analysis

Element	Concentration (at.%)
Cr	26.0
W	11.7
^{16}O	58.1
^{18}O	4.1

The data for the lower part of the Cr_2WO_6 layer, whose elemental maps are shown in **Fig. 6.20**(a), was obtained by continuing the APT measurement on the same specimen as in **Fig. 6.19**. Here, many regions of the oxide rich in ^{18}O can be seen. This indicates that the lower part of the Cr_2WO_6 layer grew in the second stage of oxidation. In the concentration profiles across a GB shown in **Fig. 6.20**(b), only see the segregation of Y at GBs is present and no oxygen segregation is seen.

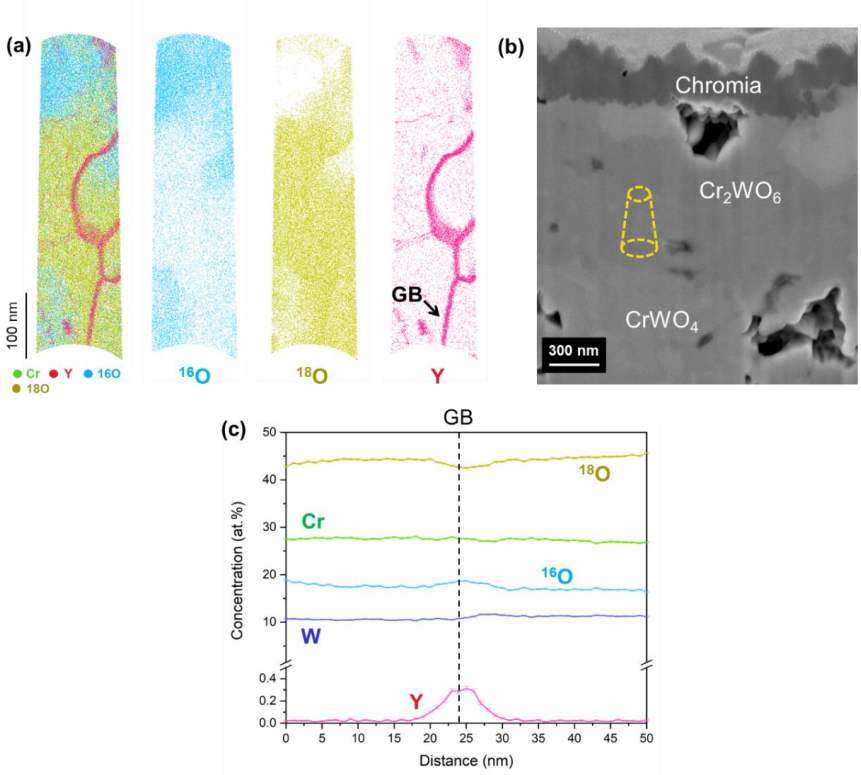

Fig. 6.20: (a) APT elemental maps from the lower part of the mixed oxide Cr_2WO_6, indicated in (b), (c) concentration profiles across the GB shown in (a).

6.6.3 Influence of Y on oxide growth direction

From the APT analysis of the oxide layer the upper regions of both oxides are rich in ^{16}O, i.e., it grew in the first stage of oxidation, while the lower region is rich in ^{18}O, i.e., it grew in the second stage of oxidation. This pattern of oxide growth is similar to that shown in **Fig. 6.14**(b), hence it can be concluded that both the chromia and mixed oxide grow in the inward direction in the ternary alloy containing Y.

^{18}O is present in the GBs of the ^{16}O-rich oxide, while no such oxygen isotope segregation is seen in the ^{18}O-rich oxide GBs. Additionally, no segregation of Cr or W at oxide GBs is seen. This is an indication that the growth of the oxide is oxygen ion diffusion controlled – oxygen diffuses via GBs of the existing oxide to form new oxide below the existing oxide. There is also a minor amount of ^{18}O present within grains in the top part of chromia and mixed oxide, which could be an overestimate. However, there is relatively more ^{18}O present within the grains of the top part of the mixed oxide as compared to that of chromia, which indicates that the mixed oxide is less

impervious to bulk diffusion of oxygen than chromia. Increased bulk diffusion could also be related to the non-stoichiometry of the mixed oxide.

The effect of Y on the increased oxidation resistance of the ternary alloy seems to be due to its observed segregation at oxide GBs, suppressing the outward cationic diffusion and resulting in the dominance of inward oxygen ion diffusion.

6.7 Summary

In this chapter, the effect of Y addition on the microstructure and oxidation resistance of W-Cr at 1000 °C was analyzed. The addition of Y results in a great improvement in oxidation resistance. The rate of oxidation of the ternary W-11.4Cr-0.6Y alloy is reduced 50-fold as compared to the binary W-11.4Cr, with no indication of spalling off. The oxide formed does not show a large volume expansion, which results in the material being able to retain its geometric integrity even after oxidation for 20 h.

The formation of a complex oxide scale with various mixed oxides occurs in both cases. However, only the ternary alloy shows the formation of a continuous, thin chromia scale above the mixed oxide, which plays the role of a protective, passivating oxide layer. In the case of the binary alloy, the formation of a much thicker Cr_2WO_6 layer dominates, which grows rapidly, mainly at the regions of high local curvature, such as sample edges and corners, and does not become passivating. Although a tungsten oxide layer is formed in both alloys, the oxide scale in the ternary alloy is less porous and is more adherent to the alloy, making it more effective at preventing the possible sublimation of the underlying tungsten oxide by making the oxide scale more resistant to spallation.

In order to explain the mechanism by which Y acts to improve the oxidation resistance, a two-step oxidation experiment using ^{18}O isotope as a tracer was performed, followed by APT analysis. It is found that both chromia and the mixed oxide Cr_2WO_6 in the ternary alloy grow in the inward direction, as seen by the distribution of oxygen isotopes in the upper and lower parts of the oxide through APT. This aligns with the theory that Y addition results in an inward-growing oxide scale, which reduces the chance of void formation at the oxide-alloy interface and increases its adherence with the alloy.

APT also revealed that Y segregates at oxide GBs, as is commonly observed in oxide scales grown on Y-containing alloys. The segregation of Y seems to affect cationic diffusion and results in the dominance of inward oxygen diffusion, leading to inward growth of the oxide. The GB segregation of ^{18}O in the ^{16}O-rich part of the oxide suggests that oxygen diffusion through the oxide occurs via GBs both in chromia and Cr_2WO_6. An analysis of the ^{18}O content within the grains of the ^{16}O-rich parts of the oxide

suggests that some amount of bulk diffusion of oxygen could also take place through the non-stoichiometric mixed oxide.

In order to analyze the overall concentration of the isotopes across the oxide scale after performing the two-step oxidation experiment, techniques such as secondary neutral mass spectrometry (SNMS) can be used to get depth profiles. The distribution of oxygen isotopes can provide an additional way to confirm the direction in which the oxide grows. By measuring the depth profiles for the oxide scale formed on both the binary and ternary alloys, the effect of Y on the growth direction can be established unambiguously.

APT was also used to analyse the presence of oxygen in the mechanically alloyed powder of W-Cr-Y. It was found that there is a significant amount of O (1.7 at.%) in the powder, and it may be more accurate to consider it to be a quaternary system, especially for modelling studies.

Chapter 7 Conclusion and Outlook

In this work, a detailed study of the oxidation mechanisms of two potential materials for use in high-temperature applications was performed. The oxidation behaviour of the alumina-forming MAX phase Cr_2AlC was studied at temperatures of 1000 °C and 1200 °C, while the chromia-forming W-based alloy W-11.4Cr-0.6Y was studied at the temperature of 1000 °C. Along with microstructural characterisation techniques, a focus was put on the use of atom probe tomography for the analysis of features such as GBs and interfaces of the oxide scale and bulk material, which are pathways for diffusion via the oxide scale and determine the stability of the oxide scale formed on the material. Important aspects pertaining to the oxidation mechanism and primary diffusion pathways could be identified through this analysis. Experiments such as the use of ^{18}O isotope as a tracer were also performed on the W-based alloy to study the mechanism by which Y acts as a reactive element in this system.

The alumina-forming MAX phase Cr_2AlC shows very good oxidation resistance at temperatures of 1000 °C and 1200 °C, showing parabolic growth kinetics at both temperatures. Along with the formation of a bilayer α-Al_2O_3 scale, there is a simultaneous formation of the porous Cr_7C_3 carbide layer below, due to the decomposition of the MAX phase. Being highly stoichiometric, the depletion of just 1 at.% Al from Cr_2AlC, which is used to form the alumina scale, results in its decomposition into these phases. This behaviour is different from the typical behaviour of alloy oxidation. Al diffuses differently through the MAX phase and carbide: via GBs in Cr_2AlC and through the bulk in Cr_7C_3. Hence, factors that affect GB diffusion, such as segregating elements or evolution in grain size, may affect the diffusion of Al through the Cr_2AlC but not through the carbide. However, the diffusion of Al does not seem to affect the oxidation rate – the GB diffusion of O through the inner large-grained alumina subscale is assumed to be the rate-controlling step of oxidation. Importantly, APT analysis shows that this part of the scale is free from impurities, both in the bulk and GBs, and hence the results of this work can be considered as characteristic of pure Cr_2AlC oxidation.

Such a detailed analysis of the presence of segregating elements and impurities in the GBs and interfaces of the oxide scale has not been done before for bulk Cr_2AlC samples, and has provided new insights into the parts of the microstructure that are important to be considered if one wants to further improve the oxidation resistance. For example, it has now been shown that diffusion through the inner alumina layer GBs is the factor controlling the oxidation rate. One could imagine that diffusion through the carbide layer, which is a unique aspect of this MAX phase, could have an influence, however this does not seem to be the case. Using reactive elements that segregate at inner

alumina GBs can greatly influence the oxidation behaviour – it is reasonable to expect that a reactive element used in the right quantity can result in a purely inward growing oxide scale, as is seen in other alumina forming materials containing reactive elements. The inner alumina grains may also show grain growth with time, which can further slowdown the oxidation rate, which could be the reason for the cubic oxidation kinetics seen in the long-term oxidation behaviour of Cr_2AlC. These findings also provide a starting point for the better understanding of the oxidation mechanism of alumina-forming MAX phases in general.

The chromia-forming W-based alloy W-11.4Cr-0.6Y shows good oxidation resistance at a temperature of 1000 °C. The addition of the reactive element Y shows a drastic improvement in the oxidation resistance, resulting in a 50-fold reduction in oxidation rate and a less porous, more adherent oxide scale. Although the oxide scale formed with and without Y consists of multiple mixed oxide layers, including a WO_3 layer underneath, the presence of Y results in the formation of a continuous, passivating chromia layer, which is slow-growing and suppresses the observed effect of increased oxide growth in the binary alloy at regions of higher curvature such as edges and corners. APT analysis of the oxide scale formed on the ternary alloy after two-step oxidation using ^{18}O revealed that the oxide grows in the inward direction with the addition of Y. Y is found to segregate at oxide GBs, which could affect cationic diffusion and result in the observed inward growth, which also makes the scale more adherent by reducing the probability of void formation at the oxide-alloy interface. Hence, the mechanism of the reactive element effect of Y in this W alloy seems to be due to its segregation at oxide GBs, resulting in inward growth of the oxide. Additionally, APT analysis was also performed on a mechanically alloyed powder particle, which showed that there is already a significant amount of oxygen uptake at this stage and Y forms clusters with O but is not fully oxidised into stable Y_2O_3.

For certain high-temperature applications such as a fusion reactor, where it is not possible to use alumina-forming materials, this study shows how significant and important the use of reactive elements can be to create chromia-forming materials with good oxidation resistance for specific applications. However, for high-temperature applications in general, where no such limitation on elements exists, an alumina former like Cr_2AlC would be a better choice, since it grows more slowly than W-Cr-Y under identical conditions, and can also be used at higher operating temperatures.

The combination of the ^{18}O tracer experiment with APT has been done on this particular alloy system for the first time, and it shows the usefulness of a tool like APT both for identifying the location of the reactive element Y and the distribution of oxygen isotopes within the scale to determine the oxide growth direction.

7.1 Outlook

- One of the mechanisms by which reactive elements work in alumina formers is by segregating at oxide GBs, hence it is expected that the addition of reactive elements at the right amount to Cr_2AlC could segregate at the inner alumina GBs and could result in a slower, purely inward-growing oxide layer. Having a purely inward-growing oxide layer could also result in a reduction in the thickness of the oxide scale, which can reduce stresses on the oxide and could prevent the delamination of the scale which was observed in this study after oxidation at 1200 °C for 20 h.
- The combination of APT with isotopic tracer experiments is a powerful tool, and can be expanded further, along with the use of SNMS to obtain depth profiles across the oxide layer. Although the oxidation experiments in this study were primarily performed in a humid atmosphere, the results of this work on their own cannot fully explain the effect of water vapour on oxidation resistance. Isotope tracer experiments performed in an ^{18}O-labelled water vapour ($H_2{}^{18}O$) atmosphere combined with APT could shed more light on the possible diffusion pathways in a humid atmosphere, specifically those involving the formation of the hydroxyl ion.
- Through APT, it is shown that the mechanically alloyed powder of W-11.4Cr-0.6Y is a quaternary system containing 1.7 at.% O, which is an important point to consider when performing modelling studies on this system.

Bibliography

[1] United Nations, What Is Climate Change? | United Nations, 2024. https://www.un.org/en/climatechange/what-is-climate-change (accessed 5 September 2024).

[2] World Meteorological Organization, 2024 is on track to be hottest year on record as warming temporarily hits 1.5°C, 2024. https://wmo.int/news/media-centre/2024-track-be-hottest-year-record-warming-temporarily-hits-15degc (accessed 22 November 2024).

[3] UNDP Climate Promise, The Climate Dictionary: An everyday guide to climate change | UNDP Climate Promise, 2024. https://climatepromise.undp.org/news-and-stories/climate-dictionary-everyday-guide-climate-change (accessed 5 September 2024).

[4] The Paris Agreement | UNFCCC, 2024. https://unfccc.int/process-and-meetings/the-paris-agreement (accessed 22 November 2024).

[5] Jean-Philippe Ansermet, Sylvain D. Brechet, Heat Engines, in: Principles of Thermodynamics, Cambridge University Press, 2019, pp. 166–202.

[6] O. Coddington, J.L. Lean, P. Pilewskie, M. Snow, D. Lindholm, A Solar Irradiance Climate Data Record, Bulletin of the American Meteorological Society 97 (2016) 1265–1282. https://doi.org/10.1175/BAMS-D-14-00265.1.

[7] D.G. Morris, A. López-Delgado, I. Padilla, M.A. Muñoz-Morris, Selection of high temperature materials for concentrated solar power systems: Property maps and experiments, Solar Energy 112 (2015) 246–258. https://doi.org/10.1016/j.solener.2014.09.050.

[8] O. Behar, A. Khellaf, K. Mohammedi, A review of studies on central receiver solar thermal power plants, Renewable and Sustainable Energy Reviews 23 (2013) 12–39. https://doi.org/10.1016/j.rser.2013.02.017.

[9] K. Vignarooban, X. Xu, A. Arvay, K. Hsu, A.M. Kannan, Heat transfer fluids for concentrating solar power systems – A review, Applied Energy 146 (2015) 383–396. https://doi.org/10.1016/j.apenergy.2015.01.125.

[10] A.H. Alami, A.G. Olabi, A. Mdallal, A. Rezk, A. Radwan, S.M.A. Rahman, S.K. Shah, M.A. Abdelkareem, Concentrating solar power (CSP) technologies: Status and analysis, International Journal of Thermofluids 18 (2023) 100340. https://doi.org/10.1016/j.ijft.2023.100340.

[11] M. Imran Khan, F. Asfand, S.G. Al-Ghamdi, Progress in technology advancements for next generation concentrated solar power using solid particle

receivers, Sustainable Energy Technologies and Assessments 54 (2022) 102813. https://doi.org/10.1016/j.seta.2022.102813.
[12] C. Villada, W. Ding, A. Bonk, T. Bauer, Engineering molten MgCl2–KCl–NaCl salt for high-temperature thermal energy storage: Review on salt properties and corrosion control strategies, Sol. Energ. Mat. Sol. C. 232 (2021) 111344. https://doi.org/10.1016/j.solmat.2021.111344.
[13] J. Sarwar, T. Shrouf, A. Srinivasa, H. Gao, M. Radovic, K. Kakosimos, Characterization of thermal performance, flux transmission performance and optical properties of MAX phase materials under concentrated solar irradiation, Sol. Energ. Mat. Sol. C. 182 (2018) 76–91. https://doi.org/10.1016/j.solmat.2018.03.018.
[14] J.P. Freidberg, Plasma Physics and Fusion Energy, Cambridge University Press, 2008.
[15] IAEA, Fundamentals of Magnetic Fusion Technology, firstst ed., International Atomic Energy Agency, Vienna, 2023.
[16] H. Bolt, V. Barabash, G. Federici, J. Linke, A. Loarte, J. Roth, K. Sato, Plasma facing and high heat flux materials – needs for ITER and beyond, Journal of Nuclear Materials 307-311 (2002) 43–52. https://doi.org/10.1016/S0022-3115(02)01175-3.
[17] F. Koch, H. Bolt, Self passivating W-based alloys as plasma facing material for nuclear fusion, Phys. Scr. T128 (2007) 100–105. https://doi.org/10.1088/0031-8949/2007/T128/020.
[18] J. Cizek, M. Vilemova, F. Lukac, M. Koller, J. Kondas, R. Singh, Cold Sprayed Tungsten Armor for Tokamak First Wall, Coatings 9 (2019) 836. https://doi.org/10.3390/coatings9120836.
[19] D.J. Young, Chapter 1 - The Nature of High Temperature Oxidation, in: D.J. Young (Ed.), High temperature oxidation and corrosion of metals, Elsevier, 2016, pp. 1–30.
[20] D.J. Young (Ed.), High temperature oxidation and corrosion of metals, Elsevier, 2016.
[21] H.J.T. Ellingham, Reducibility of oxides and sulphides in metallurgical processes, Journal of the Society of Chemical Industry 63 (1944) 125–160. https://doi.org/10.1002/jctb.5000630501.
[22] D.J. Young, Chapter 2 - Enabling Theory, in: D.J. Young (Ed.), High temperature oxidation and corrosion of metals, Elsevier, 2016, pp. 31–84.
[23] Neil Birks, Gerald H. Meier, Frederick S. Pettit, Methods of investigation, in: Introduction to the High Temperature Oxidation of Metals, Cambridge University Press, 2006, pp. 1–15.

[24] C. Wagner, Beitrag zur Theorie des Anlaufvorgangs, Zeitschrift für Physikalische Chemie 21B (1933) 25–41. https://doi.org/10.1515/zpch-1933-2105.
[25] W.J. Quadakkers, D. Naumenko, E. Wessel, V. Kochubey, L. Singheiser, Growth Rates of Alumina Scales on Fe–Cr–Al Alloys, Oxid. Met. 61 (2004) 17–37. https://doi.org/10.1023/B:OXID.0000016274.78642.ae.
[26] D.J. Tallman, B. Anasori, M.W. Barsoum, A Critical Review of the Oxidation of Ti2AlC, Ti3AlC2 and Cr2AlC in Air, Mater. Res. Lett. 1 (2013) 115–125. https://doi.org/10.1080/21663831.2013.806364.
[27] E. Lassner, W.-D. Schubert, Important Aspects of Tungsten Chemistry, in: Tungsten: Properties, Chemistry, Technology of the Element, Alloys, and Chemical Compounds, Springer US, Boston, MA, 1999, pp. 85–132.
[28] F. Klein, A. Litnovsky, T. Wegener, X. Tan, J. Gonzalez-Julian, M. Rasinski, J. Schmitz, C. Linsmeier, M. Bram, J.W. Coenen, Sublimation of advanced tungsten alloys under DEMO relevant accidental conditions, Fusion Engineering and Design 146 (2019) 1198–1202. https://doi.org/10.1016/j.fusengdes.2019.02.039.
[29] P. Pedeferri, High Temperature Corrosion, Corrosion Science and Engineering (2018) 589–610. https://doi.org/10.1007/978-3-319-97625-9_26.
[30] D.J. Young, Chapter 7 - Alloy Oxidation III: Multiphase Scales, in: D.J. Young (Ed.), High temperature oxidation and corrosion of metals, Elsevier, 2016, pp. 335–392.
[31] H.E. Evans, A.T. Donaldson, T.C. Gilmour, Mechanisms of Breakaway Oxidation and Application to a Chromia-Forming Steel, Oxid Met 52 (1999) 379–402. https://doi.org/10.1023/A:1018855914737.
[32] A.H. Heuer, D.B. Hovis, J.L. Smialek, B. Gleeson, Alumina Scale Formation: A New Perspective, J. Am. Ceram. Soc. 94 (2011) s146-s153. https://doi.org/10.1111/j.1551-2916.2011.04573.x.
[33] E.J. Opila, N.S. Jacobson, Oxidation and Corrosion of Ceramics, in: R. Riedel, I.-W. Chen (Eds.), Ceramics science and technology, Wiley-VCH, Weinheim, 2013, pp. 1–93.
[34] E.J. Opila, N.S. Jacobson, D.L. Myers, E.H. Copland, Predicting oxide stability in high-temperature water vapor, JOM 58 (2006) 22–28. https://doi.org/10.1007/s11837-006-0063-3.
[35] S. Chevalier, 10 - Formation and growth of protective alumina scales, in: W. Gao, Z. Li (Eds.), Developments in high-temperature corrosion and protection of materials, Woodhead Pub; Maney Pub; CRC Press, Cambridge, England, [England?], Boca Raton, FL, 2008, pp. 290–328.
[36] D.J. Young, Chapter 5 - Oxidation of Alloys I: Single Phase Scales, in: D.J. Young (Ed.), High temperature oxidation and corrosion of metals, Elsevier, 2016, pp. 193–260.

[37] Stainless Steel - Austenitic - 1.4301 (304) Bar and Section, 2024. https://www.aalco.co.uk/datasheets/Stainless-Steel-14301-Bar-and-Section_34.ashx (accessed 22 November 2024).
[38] Neil Birks, Gerald H. Meier, Frederick S. Pettit, Oxidation of alloys, in: Introduction to the High Temperature Oxidation of Metals, Cambridge University Press, 2006, pp. 101–162.
[39] R. Spotorno, D. Paravidino, S. Delsante, P. Piccardo, Volatilization of chromium from AISI 441 stainless steel: Time and temperature dependence, Surf. Coat. Tech. 433 (2022) 128125. https://doi.org/10.1016/j.surfcoat.2022.128125.
[40] P. Kofstad, High temperature corrosion, Elsevier Applied Science; Sole distributor in the USA and Canada, Elsevier Science Pub. Co, London, New York, New York, NY, USA, 1988.
[41] A.C.S. Sabioni, A.M. Huntz, J. Philibert, B. Lesage, C. Monty, Relation between the oxidation growth rate of chromia scales and self-diffusion in Cr2O3, J Mater Sci 27 (1992) 4782–4790. https://doi.org/10.1007/BF01166020.
[42] D.J. Park, Y.I. Jung, H.G. Kim, J.Y. Park, Y.H. Koo, Oxidation behavior of silicon carbide at 1200°C in both air and water–vapor-rich environments, Corros. Sci. 88 (2014) 416–422. https://doi.org/10.1016/j.corsci.2014.07.052.
[43] (WILLIAM THOMAS GRIFFITHS; LEONARD BESSEMER PFEIL) GB459848 (A), 1935.
[44] F. Klein, T. Wegener, A. Litnovsky, M. Rasinski, X.Y. Tan, J. Gonzalez-Julian, J. Schmitz, M. Bram, J.W. Coenen, C. Linsmeier, Oxidation resistance of bulk plasma-facing tungsten alloys, Nuclear Materials and Energy 15 (2018) 226–231. https://doi.org/10.1016/j.nme.2018.05.003.
[45] E. Lang, The Role of Active Elements in the Oxidation Behaviour of High Temperature Metals and Alloys, Springer Netherlands, Dordrecht, 1989.
[46] S. Chevalier, G. Bonnet, J. Larpin, J. Colson, The combined effect of refractory coatings containing reactive elements on high temperature oxidation behavior of chromia-forming alloys, Corros. Sci. 45 (2003) 1661–1673. https://doi.org/10.1016/S0010-938X(03)00017-9.
[47] S. Chevalier, J.P. Larpin, Influence of reactive element oxide coatings on the high temperature cyclic oxidation of chromia-forming steels, Materials Science and Engineering: A 363 (2003) 116–125. https://doi.org/10.1016/S0921-5093(03)00592-6.
[48] J. Stringer, The reactive element effect in high-temperature corrosion, Materials Science and Engineering: A 120-121 (1989) 129–137. https://doi.org/10.1016/0921-5093(89)90730-2.

[49] S. Chevalier, What did we learn on the reactive element effect in chromia scale since Pfeil 's patent?, Materials & Corrosion 65 (2014) 109–115. https://doi.org/10.1002/maco.201307310.
[50] B. Pieraggi, R.A. Rapp, Chromia Scale Growth in Alloy Oxidation and the Reactive Element Effect, J. Electrochem. Soc. 140 (1993) 2844–2850. https://doi.org/10.1149/1.2220920.
[51] A. Vayyala, I. Povstugar, T. Galiullin, D. Naumenko, W.J. Quadakkers, H. Hattendorf, J. Mayer, Effect of Nb Addition on Oxidation Mechanisms of High Cr Ferritic Steel in Ar–H2–H2O, Oxid Met 92 (2019) 471–491. https://doi.org/10.1007/s11085-019-09933-x.
[52] J. Ehlers, D.J. Young, E.J. Smaardijk, A.K. Tyagi, H.J. Penkalla, L. Singheiser, W.J. Quadakkers, Enhanced oxidation of the 9%Cr steel P91 in water vapour containing environments, Corros. Sci. 48 (2006) 3428–3454. https://doi.org/10.1016/j.corsci.2006.02.002.
[53] S. Basu, N. Obando, A. Gowdy, I. Karaman, M. Radovic, Long-Term Oxidation of Ti2AlC in Air and Water Vapor at 1000–1300°C Temperature Range, J. Electrochem. Soc. 159 (2011) C90-C96. https://doi.org/10.1149/2.052202jes.
[54] W.J. Quadakkers, J. Żurek, 1.17 - Oxidation in Steam and Steam/Hydrogen Environments, in: T.J.A. Richardson, L.L. Shreir (Eds.), Shreir's Corrosion, Elsevier Science, Oxford, 2010, pp. 407–456.
[55] D.J. Young, Chapter 11 - Effects of Water Vapour on Oxidation, in: D.J. Young (Ed.), High temperature oxidation and corrosion of metals, Elsevier, 2016, pp. 549–601.
[56] M. Dahlqvist, M.W. Barsoum, J. Rosen, MAX phases – Past, present, and future, Materials Today 72 (2024) 1–24. https://doi.org/10.1016/j.mattod.2023.11.010.
[57] M. Naguib, M. Kurtoglu, V. Presser, J. Lu, J. Niu, M. Heon, L. Hultman, Y. Gogotsi, M.W. Barsoum, Two-dimensional nanocrystals produced by exfoliation of Ti3 AlC2, Advanced Materials 23 (2011) 4248–4253. https://doi.org/10.1002/adma.201102306.
[58] V. NOWOTNY, Strukturchemie einiger Verbindungen der Übergangsmetalle mit den elementen C, Si, Ge, Sn, Progress in Solid State Chemistry 5 (1971) 27–70. https://doi.org/10.1016/0079-6786(71)90016-1.
[59] W. Jeitschko, H. Nowotny, F. Benesovsky, Carbides of formula T2MC, Journal of the Less Common Metals 7 (1964) 133–138. https://doi.org/10.1016/0022-5088(64)90055-4.
[60] V.I. Ivchenko, T.Y. Kosolapova, Abrasive properties of the ternary compounds in the systems Ti-Al-C and Ti-Al-N, Powder Metall Met Ceram 15 (1976) 626–628. https://doi.org/10.1007/BF01159451.

[61] V.I. Ivchenko, M.I. Lesnaya, V.F. Nemchenko, T.Y. Kosolapova, Preparation and some properties of the ternary compound Ti2AlN, Powder Metall Met Ceram 15 (1976) 293–295. https://doi.org/10.1007/BF01178200.
[62] J. Lis, R. Pampuch, J. Piekarczyk, L. Stobierski, New ceramics based on Ti3SiC2, Ceram. Int. 19 (1993) 219–222. https://doi.org/10.1016/0272-8842(93)90052-S.
[63] R. Pampuch, J. Lis, L. Stobierski, M. Tymkiewicz, Solid combustion synthesis of Ti3SiC2, J. Eur. Ceram. Soc. 5 (1989) 283–287. https://doi.org/10.1016/0955-2219(89)90022-8.
[64] M.W. Barsoum, T. El-Raghy, Synthesis and Characterization of a Remarkable Ceramic: Ti 3 SiC 2, J. Am. Ceram. Soc. 79 (1996) 1953–1956. https://doi.org/10.1111/j.1151-2916.1996.tb08018.x.
[65] M.W. Barsoum, D. Brodkin, T. El-Raghy, Layered machinable ceramics for high temperature applications, Scripta Mater. 36 (1997) 535–541. https://doi.org/10.1016/S1359-6462(96)00418-6.
[66] M.W. Barsoum, G. Yaroschuk, S. Tyagi, Fabrication and characterization of M2SnC (M = Ti, Zr, Hf and Nb), Scripta Mater. 37 (1997) 1583–1591. https://doi.org/10.1016/S1359-6462(97)00288-1.
[67] M.W. Barsoum, L. Farber, I. Levin, A. Procopio, T. El-Raghy, A. Berner, High-Resolution Transmission Electron Microscopy of Ti 4 AlN 3 or Ti 3 Al 2 N 2 Revisited, J. Am. Ceram. Soc. 82 (1999) 2545–2547. https://doi.org/10.1111/j.1151-2916.1999.tb02117.x.
[68] M. Barsoum, T. El-Raghy, The MAX Phases: Unique New Carbide and Nitride Materials, Am. Sci. 89 (2001) 334. https://doi.org/10.1511/2001.28.736.
[69] P. Eklund, M. Beckers, U. Jansson, H. Högberg, L. Hultman, The M+1AX phases: Materials science and thin-film processing, Thin Solid Films 518 (2010) 1851–1878. https://doi.org/10.1016/j.tsf.2009.07.184.
[70] M.W. Barsoum, MAX phases: Properties of machinable ternary carbides and nitrides, Wiley-VCH, Weinheim, 2013.
[71] M. Magnuson, M. Mattesini, Chemical bonding and electronic-structure in MAX phases as viewed by X-ray spectroscopy and density functional theory, Thin Solid Films 621 (2017) 108–130. https://doi.org/10.1016/j.tsf.2016.11.005.
[72] N.I. Medvedeva, D.L. Novikov, A.L. Ivanovsky, M.V. Kuznetsov, A.J. Freeman, Electronic properties of Ti3SiC2 -based solid solutions, Phys. Rev. B 58 (1998) 16042–16050. https://doi.org/10.1103/PhysRevB.58.16042.
[73] Z. Sun, S. Li, R. Ahuja, J.M. Schneider, Calculated elastic properties of M2AlC (M=Ti, V, Cr, Nb and Ta), Solid State Communications 129 (2004) 589–592. https://doi.org/10.1016/j.ssc.2003.12.008.

[74] M. Sokol, V. Natu, S. Kota, M.W. Barsoum, On the Chemical Diversity of the MAX Phases, Trends in Chemistry 1 (2019) 210–223. https://doi.org/10.1016/j.trechm.2019.02.016.
[75] W. Jeitschko, H. Nowotny, F. Benesovsky, Die H-Phasen Ti2InC, Zr2InC, Hf2InC und Ti2GeC, Monatshefte für Chemie 94 (1963) 1201–1205. https://doi.org/10.1007/BF00905711.
[76] J. Gonzalez-Julian, S. Onrubia, M. Bram, O. Guillon, Effect of sintering method on the microstructure of pure Cr_2AlC MAX phase ceramics, J. Ceram. Soc. Japan 124 (2016) 415–420. https://doi.org/10.2109/jcersj2.15263.
[77] A. Dash, R. Vaßen, O. Guillon, J. Gonzalez-Julian, Molten salt shielded synthesis of oxidation prone materials in air, Nat. Mater. 18 (2019) 465–470. https://doi.org/10.1038/s41563-019-0328-1.
[78] N. Kubitza, R. Xie, I. Tarasov, C. Shen, H. Zhang, U. Wiedwald, C.S. Birkel, Microwave-Assisted Synthesis of the New Solid-Solution (V 1– x Cr x) 2 GaC (0 ≤ x ≤ 1), a Pauli Paramagnet Almost Matching the Stoner Criterion for x = 0.80, Chem. Mater. 35 (2023) 4427–4434. https://doi.org/10.1021/acs.chemmater.3c00591.
[79] J.M. Schneider, D.P. Sigumonrong, D. Music, C. Walter, J. Emmerlich, R. Iskandar, J. Mayer, Elastic properties of Cr2AlC thin films probed by nanoindentation and ab initio molecular dynamics, Scripta Mater. 57 (2007) 1137–1140. https://doi.org/10.1016/j.scriptamat.2007.08.006.
[80] H. Fakih, S. Jacques, M.-P. Berthet, F. Bosselet, O. Dezellus, J.-C. Viala, The growth of Ti3SiC2 coatings onto SiC by reactive chemical vapor deposition using H2 and TiCl4, Surf. Coat. Tech. 201 (2006) 3748–3755. https://doi.org/10.1016/j.surfcoat.2006.09.040.
[81] B.R. Maier, B.L. Garcia-Diaz, B. Hauch, L.C. Olson, R.L. Sindelar, K. Sridharan, Cold spray deposition of Ti2AlC coatings for improved nuclear fuel cladding, J. Nucl. Mater. 466 (2015) 712–717. https://doi.org/10.1016/j.jnucmat.2015.06.028.
[82] J. Gonzalez-Julian, G. Mauer, D. Sebold, D.E. Mack, R. Vassen, Cr2AlC MAX phase as bond coat for thermal barrier coatings: Processing, testing under thermal gradient loading, and future challenges, J. Am. Ceram. Soc. 103 (2020) 2362–2375. https://doi.org/10.1111/jace.16935.
[83] H. Fashandi, M. Dahlqvist, J. Lu, J. Palisaitis, S.I. Simak, I.A. Abrikosov, J. Rosen, L. Hultman, M. Andersson, A. Lloyd Spetz, P. Eklund, Synthesis of Ti3AuC2, Ti3Au2C2 and Ti3IrC2 by noble metal substitution reaction in Ti3SiC2 for high-temperature-stable Ohmic contacts to SiC, Nat. Mater. 16 (2017) 814–818. https://doi.org/10.1038/nmat4896.
[84] H. Ding, Y. Li, J. Lu, K. Luo, K. Chen, M. Li, P.O.Å. Persson, L. Hultman, P. Eklund, S. Du, Z. Huang, Z. Chai, H. Wang, P. Huang, Q. Huang, Synthesis of

MAX phases Nb 2 CuC and Ti 2 (Al 0.1 Cu 0.9)N by A-site replacement reaction in molten salts, Mater. Res. Lett. 7 (2019) 510–516. https://doi.org/10.1080/21663831.2019.1672822.

[85] M. Li, J. Lu, K. Luo, Y. Li, K. Chang, K. Chen, J. Zhou, J. Rosen, L. Hultman, P. Eklund, P.O.Å. Persson, S. Du, Z. Chai, Z. Huang, Q. Huang, Element Replacement Approach by Reaction with Lewis Acidic Molten Salts to Synthesize Nanolaminated MAX Phases and MXenes, J. Am. Chem. Soc. 141 (2019) 4730–4737. https://doi.org/10.1021/jacs.9b00574.

[86] C.-C. Lai, H. Fashandi, J. Lu, J. Palisaitis, P.O.Å. Persson, L. Hultman, P. Eklund, J. Rosen, Phase formation of nanolaminated Mo2AuC and Mo2(Au1-xGax)2C by a substitutional reaction within Au-capped Mo2GaC and Mo2Ga2C thin films, Nanoscale 9 (2017) 17681–17687. https://doi.org/10.1039/C7NR03663A.

[87] M. Radovic, M.W. Barsoum, MAX phases: bridging the gap between metals and ceramics, Am. Ceram. Soc. Bull. 92 (2013) 20–27.

[88] J. Gonzalez-Julian, Processing of MAX phases: From synthesis to applications, J. Am. Ceram. Soc. 104 (2021) 659–690. https://doi.org/10.1111/jace.17544.

[89] Y. Du, J.C. Schuster, H.J. Seifert, F. Aldinger, Experimental Investigation and Thermodynamic Calculation of the Titanium–Silicon–Carbon System, J. Am. Ceram. Soc. 83 (2000) 197–203. https://doi.org/10.1111/j.1151-2916.2000.tb01170.x.

[90] M. Radovic, M.W. Barsoum, MAX phases: bridging the gap between metals and ceramics, Am. Ceram. Soc. Bull. 92 (2013) 20–27.

[91] M.W. Barsoum, M. Radovic, P. Finkel, T. El-Raghy, Ti 3 SiC 2 and ice, Applied Physics Letters 79 (2001) 479–481. https://doi.org/10.1063/1.1384479.

[92] T. El-Raghy, A. Zavaliangos, M.W. Barsoum, S.R. Kalidindi, Damage Mechanisms around Hardness Indentations in Ti 3 SiC 2, J. Am. Ceram. Soc. 80 (1997) 513–516. https://doi.org/10.1111/j.1151-2916.1997.tb02861.x.

[93] C. Gilbert, D. Bloyer, M. Barsoum, T. El-Raghy, A. Tomsia, R. Ritchie, Fatigue-crack growth and fracture properties of coarse and fine-grained Ti3SiC2, Scripta Mater. 42 (2000) 761–767. https://doi.org/10.1016/S1359-6462(99)00427-3.

[94] M.W. Barsoum, L.H. Ho-Duc, M. Radovic, T. El-Raghy, Long Time Oxidation Study of Ti[sub 3]SiC[sub 2], Ti[sub 3]SiC[sub 2]/SiC, and Ti[sub 3]SiC[sub 2]/TiC Composites in Air, J. Electrochem. Soc. 150 (2003) B166. https://doi.org/10.1149/1.1556035.

[95] J. Zhang, L. Wang, W. Jiang, L. Chen, High temperature oxidation behavior and mechanism of Ti3SiC2–SiC nanocomposites in air, Composites Science and Technology 68 (2008) 1531–1538. https://doi.org/10.1016/j.compscitech.2007.10.029.

[96] S. Gupta, M.W. Barsoum, Synthesis and Oxidation of V[sub 2]AlC and (Ti[sub 0.5],V[sub 0.5])[sub 2]AlC in Air, J. Electrochem. Soc. 151 (2004) D24. https://doi.org/10.1149/1.1639160.
[97] W. Tian, P. Wang, Y. Kan, G. Zhang, Oxidation behavior of Cr2AlC ceramics at 1,100 and 1,250 °C, J. Mater. Sci. 43 (2008) 2785–2791. https://doi.org/10.1007/s10853-008-2516-2.
[98] M. Sundberg, G. Malmqvist, A. Magnusson, T. El-Raghy, Alumina forming high temperature silicides and carbides, Ceram. Int. 30 (2004) 1899–1904. https://doi.org/10.1016/j.ceramint.2003.12.046.
[99] X. Wang, Y. Zhou, Oxidation behavior of Ti3AlC2 at 1000–1400 °C in air, Corros. Sci. 45 (2003) 891–907. https://doi.org/10.1016/S0010-938X(02)00177-4.
[100] X.H. Wang, Y.C. Zhou, Oxidation behavior of TiC-containing Ti 3 AlC 2 based material at 500–900 °C in air, Materials Research Innovations 7 (2003) 381–390. https://doi.org/10.1007/s10019-003-0278-7.
[101] J.L. Smialek, Unusual Oxidative Limitations for Al-MAX Phases, 2017.
[102] X. Li, L. Zheng, Y. Qian, J. Xu, M. Li, Breakaway oxidation of Ti3AlC2 during long-term exposure in air at 1100 °C, Corros. Sci. 104 (2016) 112–122. https://doi.org/10.1016/j.corsci.2015.12.001.
[103] S. Badie, D. Sebold, R. Vaßen, O. Guillon, J. Gonzalez-Julian, Mechanism for breakaway oxidation of the Ti2AlC MAX phase, Acta Mater. 215 (2021) 117025. https://doi.org/10.1016/j.actamat.2021.117025.
[104] A. Zuber, G. Parry, C. Coupeau, P.O. Renault, V. Gauthier-Brunet, S. Dubois, Alumina scale buckling during high temperature oxidation of Cr2AlC MAX Phase, J. Eur. Ceram. Soc. 43 (2023) 7334–7340. https://doi.org/10.1016/j.jeurceramsoc.2023.08.013.
[105] J. Gonzalez-Julian, T. Go, D.E. Mack, R. Vaßen, Environmental resistance of Cr2AlC MAX phase under thermal gradient loading using a burner rig, J. Am. Ceram. Soc. 101 (2018) 1841–1846. https://doi.org/10.1111/jace.15425.
[106] K. van Loo, T. Lapauw, N. Ozalp, E. Ström, K. Lambrinou, J. Vleugels, Compatibility of SiC and MAX phase-based ceramics with a KNO3-NaNO3 molten solar salt, Sol. Energ. Mat. Sol. C. 195 (2019) 228–240. https://doi.org/10.1016/j.solmat.2019.03.007.
[107] C. Azina, S. Badie, A. Litnovsky, L. Silvestroni, E. Sani, J. Gonzalez-Julian, MAX phases as candidates for Concentrated Solar Power receivers, 2022.
[108] Z.J. Lin, M.S. Li, J.Y. Wang, Y.C. Zhou, High-temperature oxidation and hot corrosion of Cr2AlC, Acta Mater. 55 (2007) 6182–6191. https://doi.org/10.1016/j.actamat.2007.07.024.

[109] D.B. Lee, T.D. Nguyen, S.W. Park, Long-Time Oxidation of Cr2AlC Between 700 and 1,000 °C in Air, Oxid. Met. 77 (2012) 275–287. https://doi.org/10.1007/s11085-012-9285-7.
[110] D.E. Hajas, M. to Baben, B. Hallstedt, R. Iskandar, J. Mayer, J.M. Schneider, Oxidation of Cr2AlC coatings in the temperature range of 1230 to 1410°C, Surf. Coat. Tech. 206 (2011) 591–598. https://doi.org/10.1016/j.surfcoat.2011.03.086.
[111] A. Zuber, V. Gauthier-Brunet, J. Roger, J. Gonzalez-Julian, T. Ouisse, S. Dubois, Towards a better understanding of the high-temperature oxidation of MAX phase Cr2AlC, J. Eur. Ceram. Soc. 42 (2022) 2089–2096. https://doi.org/10.1016/j.jeurceramsoc.2021.12.057.
[112] D.B. Lee, T.D. Nguyen, J.H. Han, S.W. Park, Oxidation of Cr2AlC at 1300°C in air, Corros. Sci. 49 (2007) 3926–3934. https://doi.org/10.1016/j.corsci.2007.03.044.
[113] J.L. Smialek, Oxygen diffusivity in alumina scales grown on Al-MAX phases, Corros. Sci. 91 (2015) 281–286. https://doi.org/10.1016/j.corsci.2014.11.030.
[114] A. Shamsipoor, M. Farvizi, M. Razavi, A. Keyvani, B. Mousavi, Comparison of the High-Temperature Oxidation Behavior of Cr2AlC MAX Phase and CoNiCrAlY Compounds, Oxid. Met. 95 (2021) 1–21. https://doi.org/10.1007/s11085-020-10008-5.
[115] S. Li, X. Chen, Y. Zhou, G. Song, Influence of grain size on high temperature oxidation behavior of Cr2AlC ceramics, Ceram. Int. 39 (2013) 2715–2721. https://doi.org/10.1016/j.ceramint.2012.09.039.
[116] X. Li, X. Xie, J. Gonzalez-Julian, J. Malzbender, R. Yang, Mechanical and oxidation behavior of textured Ti2AlC and Ti3AlC2 MAX phase materials, J. Eur. Ceram. Soc. 40 (2020) 5258–5271. https://doi.org/10.1016/j.jeurceramsoc.2020.07.043.
[117] A. Zuber, V. Gauthier-Brunet, J. Roger, J. Gonzalez-Julian, T. Ouisse, S. Dubois, Cr2AlC high temperature oxidation under dry and wet air: Understanding of the oxidation mechanism, J. Eur. Ceram. Soc. (2023). https://doi.org/10.1016/j.jeurceramsoc.2023.05.012.
[118] L. Shang, P. Konda Gokuldoss, S. Sandlöbes, M. to Baben, J.M. Schneider, Effect of Si additions on the Al2O3 grain refinement upon oxidation of Cr2AlC MAX phase, J. Eur. Ceram. Soc. 37 (2017) 1339–1347. https://doi.org/10.1016/j.jeurceramsoc.2016.11.050.
[119] O. Berger, R. Boucher, Crack healing in Y-doped Cr 2 AlC-MAX phase coatings, Surface Engineering 33 (2017) 192–203. https://doi.org/10.1080/02670844.2016.1201366.
[120] T.A. ElMelegy, M. Sokol, M.W. Barsoum, Enhanced yield synthesis of bulk dense (M2/3Y1/3)2AlC (M = Cr, W, Mo) in-plane chemically ordered quaternary atomically laminated i-MAX phases and oxidation of (Cr2/3Y1/3)2AlC and

(Mo2/3Y1/3)2AlC, Journal of Alloys and Compounds 867 (2021) 158930. https://doi.org/10.1016/j.jallcom.2021.158930.
[121] C. Azina, T. Bartsch, D.M. Holzapfel, M. Dahlqvist, J. Rosen, L. Löfler, A.S.J. Mendez, M. Hans, D. Primetzhofer, J.M. Schneider, Yttrium incorporation in Cr 2 AlC: On the metastable phase formation and decomposition of (Cr,Y) 2 AlC MAX phase thin films, J. Am. Ceram. Soc. 106 (2023) 2652–2665. https://doi.org/10.1111/jace.18931.
[122] W.M. Haynes, D.R. Lide, T.J. Bruno, CRC Handbook of Chemistry and Physics, CRC Press, 2016.
[123] E. Lassner, W.-D. Schubert, Tungsten, Springer-Verlag, Boston, MA, 1999.
[124] J.W. Coenen, S. Antusch, M. Aumann, W. Biel, J. Du, J. Engels, S. Heuer, A. Houben, T. Hoeschen, B. Jasper, F. Koch, J. Linke, A. Litnovsky, Y. Mao, R. Neu, G. Pintsuk, J. Riesch, M. Rasinski, J. Reiser, M. Rieth, A. Terra, B. Unterberg, T. Weber, T. Wegener, J.-H. You, C. Linsmeier, Materials for DEMO and reactor applications—boundary conditions and new concepts, Phys. Scr. T167 (2016) 14002. https://doi.org/10.1088/0031-8949/2016/T167/014002.
[125] Y. Igitkhanov, B. Bazylev, I. Landman, R. Fetzer, Design Strategy for the PFC in DEMO Reactor (KIT Scientific Reports ; 7637), KIT Scientific Publishing, 2013.
[126] D. Maisonnier, A conceptual study of commercial fusion power plants, Final Report of the European Fusion Power Plant Conceptual Study (PPCS) (2005).
[127] T. Wegener, F. Klein, A. Litnovsky, M. Rasinski, J. Brinkmann, F. Koch, C. Linsmeier, Development of yttrium-containing self-passivating tungsten alloys for future fusion power plants, Nuclear Materials and Energy 9 (2016) 394–398. https://doi.org/10.1016/j.nme.2016.07.011.
[128] J.E. WHITE, Development of oxidation resistant tungsten- base alloys, AIAA Journal 4 (1966) 307–312. https://doi.org/10.2514/3.3433.
[129] P.E. Blackburn, K.F. Andrew, E.A. Gulbransen, F.A. Brassart, OXIDATION OF TUNGSTEN AND TUNGSTEN BASED ALLOYS, 1961.
[130] V.Y. Ivanov, Y.P. Nechiporenko, L.N. Yefimenko, M.I. Yurchenko, High Temperature Oxidation Protection of Tungsten, National Aeronautics and Space Administration, 1969.
[131] J. Schuster, Al-W Binary Phase Diagram Evaluation, MSI Eureka 34 (2006) 20.15747.1.5. https://doi.org/10.7121/msi-eureka-20.15747.1.5.
[132] M. Stubičar, A. Tonejc, N. Radić, Microhardness characterization of Al–W thin films, Vacuum 61 (2001) 309–316. https://doi.org/10.1016/S0042-207X(01)00135-X.
[133] Y. Ouyang, X. Zhong, W. Wu, Extended solid solubility for Al-W binary system by mechanical alloying, Sci. China Ser. A-Math. 43 (2000) 180–184. https://doi.org/10.1007/BF02876044.

[134] M. Kassabeh, Studies on Aluminium-Containing Tungsten Alloys. Bachelor Thesis, 2020.
[135] N. Bochvar, T. Dobatkina, N. Kolchugina, V. Tomashyk, Si-W Binary Phase Diagram Evaluation, MSI Eureka 60 (2015) 20.19501.1.3. https://doi.org/10.7121/msi-eureka-20.19501.1.3.
[136] W. Liu, J. Di, W. Zhang, L. Xue, Y. Yan, Oxidation resistance behavior of smart W-Si bulk composites, Corros. Sci. 163 (2020) 108222. https://doi.org/10.1016/j.corsci.2019.108222.
[137] G. Yi, W. Liu, C. Ye, L. Xue, Y. Yan, A self-passivating W-Si-Y alloy: Microstructure and oxidation resistance behavior at high temperatures, Corros. Sci. 192 (2021) 109820. https://doi.org/10.1016/j.corsci.2021.109820.
[138] F. Koch, J. Brinkmann, S. Lindig, T.P. Mishra, C. Linsmeier, Oxidation behaviour of silicon-free tungsten alloys for use as the first wall material, Phys. Scr. T145 (2011) 14019. https://doi.org/10.1088/0031-8949/2011/T145/014019.
[139] G. Effenberg, Cr-W Phase Diagrams as Published, MSI, Materials Science International Services GmbH, Stuttgart, 2002. http://docs.msi-eureka.com/full-html/30.24049.1.2/Cr-W_Phase-Diagrams-as-Published.
[140] S. Telu, A. Patra, M. Sankaranarayana, R. Mitra, S.K. Pabi, Microstructure and cyclic oxidation behavior of W–Cr alloys prepared by sintering of mechanically alloyed nanocrystalline powders, International Journal of Refractory Metals and Hard Materials 36 (2013) 191–203. https://doi.org/10.1016/j.ijrmhm.2012.08.015.
[141] S. Telu, R. Mitra, S.K. Pabi, High temperature oxidation behavior of W–Cr–Nb Alloys in the Temperature Range of 800–1200°C, International Journal of Refractory Metals and Hard Materials 38 (2013) 47–59. https://doi.org/10.1016/j.ijrmhm.2012.12.008.
[142] C. García-Rosales, P. López-Ruiz, S. Alvarez-Martín, A. Calvo, N. Ordás, F. Koch, J. Brinkmann, Oxidation behaviour of bulk W-Cr-Ti alloys prepared by mechanical alloying and HIPing, Fusion Engineering and Design 89 (2014) 1611–1616. https://doi.org/10.1016/j.fusengdes.2014.04.057.
[143] T. Wegener, F. Klein, A. Litnovsky, M. Rasinski, J. Brinkmann, F. Koch, C. Linsmeier, Development and analyses of self-passivating tungsten alloys for DEMO accidental conditions, Fusion Engineering and Design 124 (2017) 183–186. https://doi.org/10.1016/j.fusengdes.2017.03.072.
[144] A. Calvo, C. García-Rosales, F. Koch, N. Ordás, I. Iturriza, H. Greuner, G. Pintsuk, C. Sarbu, Manufacturing and testing of self-passivating tungsten alloys of different composition, Nuclear Materials and Energy 9 (2016) 422–429. https://doi.org/10.1016/j.nme.2016.06.002.

[145] S. Telu, R. Mitra, S.K. Pabi, Effect of Y2O3 Addition on Oxidation Behavior of W-Cr Alloys, Metall Mater Trans A 46 (2015) 5909–5919. https://doi.org/10.1007/s11661-015-3166-z.

[146] X.Y. Tan, F. Klein, A. Litnovsky, T. Wegener, J. Schmitz, C. Linsmeier, J.W. Coenen, U. Breuer, M. Rasinski, P. Li, L.M. Luo, Y.C. Wu, Evaluation of the high temperature oxidation of W-Cr-Zr self-passivating alloys, Corrosion Science 147 (2019) 201–211. https://doi.org/10.1016/j.corsci.2018.11.022.

[147] E. Sal, C. García-Rosales, K. Schlueter, K. Hunger, M. Gago, M. Wirtz, A. Calvo, I. Andueza, R. Neu, G. Pintsuk, Microstructure, oxidation behaviour and thermal shock resistance of self-passivating W-Cr-Y-Zr alloys, Nuclear Materials and Energy 24 (2020) 100770. https://doi.org/10.1016/j.nme.2020.100770.

[148] A. Litnovsky, F. Klein, X. Tan, J. Ertmer, J.W. Coenen, C. Linsmeier, J. Gonzalez-Julian, M. Bram, I. Povstugar, T. Morgan, Y.M. Gasparyan, A. Suchkov, D. Bachurina, D. Nguyen-Manh, M. Gilbert, D. Sobieraj, J.S. Wróbel, E. Tejado, J. Matejicek, H. Zoz, H.U. Benz, P. Bittner, A. Reuban, Advanced Self-Passivating Alloys for an Application under Extreme Conditions, Metals 11 (2021) 1255. https://doi.org/10.3390/met11081255.

[149] A. Calvo, C. García-Rosales, N. Ordás, I. Iturriza, K. Schlueter, F. Koch, G. Pintsuk, E. Tejado, J.Y. Pastor, Self-passivating W-Cr-Y alloys: Characterization and testing, Fusion Engineering and Design 124 (2017) 1118–1121. https://doi.org/10.1016/j.fusengdes.2017.03.001.

[150] F. Klein, M.R. Gilbert, A. Litnovsky, J. Gonzalez-Julian, S. Weckauf, T. Wegener, J. Schmitz, C. Linsmeier, M. Bram, J.W. Coenen, Tungsten–chromium–yttrium alloys as first wall armor material: Yttrium concentration, oxygen content and transmutation elements, Fusion Engineering and Design 158 (2020) 111667. https://doi.org/10.1016/j.fusengdes.2020.111667.

[151] Y. Zhang, W.W. Gerberich, D.A. Shores, Plastic deformation of oxide scales at elevated temperatures, Journal of Materials Research 12 (1997) 697–705. https://doi.org/10.1557/JMR.1997.0104.

[152] Di Zhu, J.H. Stout, J.C. Nelson, D.A. Shores, The Influence of Yttrium on the Interfacial Fracture Resistance in Oxide Film/Ni-25Cr Alloy Systems, MSF 251-254 (1997) 437–444. https://doi.org/10.4028/www.scientific.net/MSF.251-254.437.

[153] E.J. Felten, High-Temperature Oxidation of Fe-Cr Base Alloys with Particular Reference to Fe-Cr-Y Alloys, J. Electrochem. Soc. 108 (1961) 490. https://doi.org/10.1149/1.2428122.

[154] K. Przybylski, A.J. Garratt-Reed, G.J. Yurek, Grain Boundary Segregation of Yttrium in Chromia Scales, J. Electrochem. Soc. 135 (1988) 509–517. https://doi.org/10.1149/1.2095646.

[155] P.Y. Hou, J. Stringer, The influence of ion-implanted yttrium on the selective oxidation of chromium in Co-25 wt.% Cr, Oxid Met 29 (1988) 45–73. https://doi.org/10.1007/BF00656349.
[156] F. Klein, T. Wegener, A. Litnovsky, M. Rasinski, X. Tan, J. Schmitz, C. Linsmeier, J. Coenen, H. Du, J. Mayer, U. Breuer, On Oxidation Resistance Mechanisms at 1273 K of Tungsten-Based Alloys Containing Chromium and Yttria, Metals 8 (2018) 488. https://doi.org/10.3390/met8070488.
[157] B.S. Murty, S. Ranganathan, Novel materials synthesis by mechanical alloying/milling, International Materials Reviews 43 (1998) 101–141. https://doi.org/10.1179/imr.1998.43.3.101.
[158] C. Suryanarayana, Mechanical alloying: a critical review, Mater. Res. Lett. 10 (2022) 619–647. https://doi.org/10.1080/21663831.2022.2075243.
[159] J.S. Benjamin, Mechanical Alloying, Scientific American 234 (1976) 40–49.
[160] O. Guillon, J. Gonzalez-Julian, B. Dargatz, T. Kessel, G. Schierning, J. Räthel, M. Herrmann, Field-Assisted Sintering Technology/Spark Plasma Sintering: Mechanisms, Materials, and Technology Developments, Advanced Engineering Materials 16 (2014) 830–849. https://doi.org/10.1002/adem.201300409.
[161] A.M. Laptev, M. Bram, D. Garbiec, J. Räthel, A. van der Laan, Y. Beynet, J. Huber, M. Küster, M. Cologna, O. Guillon, Tooling in Spark Plasma Sintering Technology: Design, Optimization, and Application, Adv Eng Mater 26 (2024) 2301391. https://doi.org/10.1002/adem.202301391.
[162] ThermoLab website. https://tec.ipp.kfa-juelich.de/thermolab/.
[163] P. Le Parlouër, Thermal Analysis and Calorimetry Techniques for Catalytic Investigations, Calorimetry and Thermal Methods in Catalysis 154 (2013) 51–101. https://doi.org/10.1007/978-3-642-11954-5_2.
[164] N. Saadatkhah, A. Carillo Garcia, S. Ackermann, P. Leclerc, M. Latifi, S. Samih, G.S. Patience, J. Chaouki, Experimental methods in chemical engineering: Thermogravimetric analysis—TGA, Can J Chem Eng 98 (2020) 34–43. https://doi.org/10.1002/cjce.23673.
[165] J. Brentano, Focussing method of crystal powder analysis by X-rays, Proc. Phys. Soc. London 37 (1924) 184–193. https://doi.org/10.1088/1478-7814/37/1/326.
[166] Analytical Science Article DO Series, Focused ion beams: An overview of the technology and its capabilities - 2020 - Wiley Analytical Science, 2024. https://analyticalscience.wiley.com/content/article-do/focused-ion-beams-overview-technology-and-its-capabilities (accessed 22 November 2024).
[167] Y. Leng, Materials characterization: Introduction to microscopic and spectroscopic mrthods, secondnd ed., Wiley-VCH Verlag GmbH & Co. KGaA, Weinheim, op. 2013.

[168] J. Mayer, L.A. Giannuzzi, T. Kamino, J. Michael, TEM Sample Preparation and FIB-Induced Damage, MRS Bull. 32 (2007) 400–407. https://doi.org/10.1557/mrs2007.63.
[169] A. Kovács, R. Schierholz, K. Tillmann, FEI Titan G2 80-200 CREWLEY, JLSRF 2 (2016). https://doi.org/10.17815/jlsrf-2-68.
[170] E.W. Müller, J.A. Panitz, S.B. McLane, The Atom-Probe Field Ion Microscope, Rev. Sci. Instrum. 39 (1968) 83–86. https://doi.org/10.1063/1.1683116.
[171] A. Cerezo, T.J. Godfrey, G.D.W. Smith, Application of a position-sensitive detector to atom probe microanalysis, Rev. Sci. Instrum. 59 (1988) 862–866. https://doi.org/10.1063/1.1139794.
[172] T.F. Kelly, D.J. Larson, The second revolution in atom probe tomography, MRS Bull. 37 (2012) 150–158. https://doi.org/10.1557/mrs.2012.3.
[173] B. Gault, A. Chiaramonti, O. Cojocaru-Mirédin, P. Stender, R. Dubosq, C. Freysoldt, S.K. Makineni, T. Li, M. Moody, J.M. Cairney, Atom probe tomography, Nat Rev Methods Primers 1 (2021) 1–30. https://doi.org/10.1038/s43586-021-00047-w.
[174] M.K. Miller, K.F. Russell, K. Thompson, R. Alvis, D.J. Larson, Review of atom probe FIB-based specimen preparation methods, Microanal 13 (2007) 428–436. https://doi.org/10.1017/S1431927607070845.
[175] D.J. Larson, T.J. Prosa, R.M. Ulfig, B.P. Geiser, T.F. Kelly (Eds.), Local Electrode Atom Probe Tomography, Springer New York, New York, NY, 2013.
[176] D.J. Larson, T.J. Prosa, R.M. Ulfig, B.P. Geiser, T.F. Kelly, Data Collection, in: D.J. Larson, T.J. Prosa, R.M. Ulfig, B.P. Geiser, T.F. Kelly (Eds.), Local Electrode Atom Probe Tomography, Springer New York, New York, NY, 2013, pp. 79–108.
[177] P. Bas, A. Bostel, B. Deconihout, D. Blavette, A general protocol for the reconstruction of 3D atom probe data, Applied Surface Science 87-88 (1995) 298–304. https://doi.org/10.1016/0169-4332(94)00561-3.
[178] B. Gault, D. Haley, F. de Geuser, M.P. Moody, E.A. Marquis, D.J. Larson, B.P. Geiser, Advances in the reconstruction of atom probe tomography data, Ultramicroscopy 111 (2011) 448–457. https://doi.org/10.1016/j.ultramic.2010.11.016.
[179] B. Gault, Atom probe microscopy, Springer, New York, 2012.
[180] K. Stiller, L. Viskari, G. Sundell, F. Liu, M. Thuvander, H.-O. Andrén, D.J. Larson, T. Prosa, D. Reinhard, Atom Probe Tomography of Oxide Scales, Oxid. Met. 79 (2013) 227–238. https://doi.org/10.1007/s11085-012-9330-6.
[181] F. Liu, M. Halvarsson, K. Hellström, J.-E. Svensson, L.-G. Johansson, First Three-Dimensional Atomic Resolution Investigation of Thermally Grown Oxide on a FeCrAl Alloy, Oxid. Met. 83 (2015) 441–451. https://doi.org/10.1007/s11085-015-9530-y.

[182] T. Boll, K.A. Unocic, B.A. Pint, K. Stiller, Interfaces in Oxides Formed on NiAlCr Doped with Y, Hf, Ti, and B, Microsc. Microanal. 23 (2017) 396–403. https://doi.org/10.1017/S1431927617000186.

[183] P. Kontis, S. Pedrazzini, Y. Gong, P.A. Bagot, M.P. Moody, R.C. Reed, The effect of boron on oxide scale formation in a new polycrystalline superalloy, Scripta Mater. 127 (2017) 156–159. https://doi.org/10.1016/j.scriptamat.2016.09.013.

[184] A. Devaraj, D.J. Barton, C.-H. Li, S.V. Lambeets, T. Liu, A. Battu, S. Vaithiyalingam, S. Thevuthasan, F. Yang, J. Guo, T. Li, Y. Ren, L. Kovarik, D.E. Perea, M.L. Sushko, Visualizing the Nanoscale Oxygen and Cation Transport Mechanisms during the Early Stages of Oxidation of Fe–Cr–Ni Alloy Using In Situ Atom Probe Tomography, Adv. Mater. Interfaces 9 (2022) 2200134. https://doi.org/10.1002/admi.202200134.

[185] T.J. Prosa, D.J. Larson, Modern Focused-Ion-Beam-Based Site-Specific Specimen Preparation for Atom Probe Tomography, Microsc. Microanal. 23 (2017) 194–209. https://doi.org/10.1017/S1431927616012642.

[186] E.W.A. Young, H.E. Bishop, J.H.W. de Wit, On the use of markers and tracers to establish the growth mechanism of alumina scales during high temperature oxidation, Surface & Interface Analysis 9 (1986) 163–168. https://doi.org/10.1002/sia.740090306.

[187] E. YOUNG, J. DEWIT, The use of a 18O tracer and Rutherford backscattering spectrometry to study the oxidation mechanism of NiAl, Solid State Ionics 16 (1985) 39–46. https://doi.org/10.1016/0167-2738(85)90022-0.

[188] F. Czerwinski, On the use of the micromarker technique for studying the growth mechanism of thin oxide films, Acta Mater. 48 (2000) 721–733. https://doi.org/10.1016/S1359-6454(99)00396-1.

[189] K.G. Pradeep, K. Chang, A. Kovács, S. Sen, A. Marshal, R. de Kloe, R.E. Dunin-Borkowski, J.M. Schneider, Nano-scale Si segregation and precipitation in Cr 2 Al(Si)C MAX phase coatings impeding grain growth during oxidation, Mater. Res. Lett. 7 (2019) 180–187. https://doi.org/10.1080/21663831.2019.1572663.

[190] X. Chen, B. Stelzer, M. Hans, R. Iskandar, J. Mayer, J.M. Schneider, Enhancing the high temperature oxidation behavior of Cr 2 AlC coatings by reducing grain boundary nanoporosity, Mater. Res. Lett. 9 (2021) 127–133. https://doi.org/10.1080/21663831.2020.1854358.

[191] M. Thuvander, J. Weidow, J. Angseryd, L.K.L. Falk, F. Liu, M. Sonestedt, K. Stiller, H.-O. Andrén, Quantitative atom probe analysis of carbides, Ultramicroscopy 111 (2011) 604–608. https://doi.org/10.1016/j.ultramic.2010.12.024.

[192] I. Povstugar, J. Weber, D. Naumenko, T. Huang, M. Klinkenberg, W.J. Quadakkers, Correlative Atom Probe Tomography and Transmission Electron Microscopy Analysis of Grain Boundaries in Thermally Grown Alumina Scale, Microsc. Microanal. 25 (2019) 11–20. https://doi.org/10.1017/S143192761801557X.

[193] B.W. Krakauer, D.N. Seidman, Absolute atomic-scale measurements of the Gibbsian interfacial excess of solute at internal interfaces, Phys. Rev. B Condens. Matter 48 (1993) 6724–6727. https://doi.org/10.1103/PhysRevB.48.6724.

[194] P. Maugis, K. Hoummada, A methodology for the measurement of the interfacial excess of solute at a grain boundary, Scripta Mater. 120 (2016) 90–93. https://doi.org/10.1016/j.scriptamat.2016.04.005.

[195] I.E. McCarroll, A. La Fontaine, T.D. Nguyen, A.F. Smith, J. Zhang, D.J. Young, J.M. Cairney, Performance of an FeCrAl alloy in a high-temperature CO2 environment, Corros. Sci. 139 (2018) 267–274. https://doi.org/10.1016/j.corsci.2018.05.007.

[196] Materials Project for Cr7C3 (mp-19855). https://next-gen.materialsproject.org/materials/mp-19855/ (accessed 21 November 2024).

[197] B. Hallstedt, D. Music, Z. Sun, Thermodynamic evaluation of the Al–Cr–C system, Int. J. Mater. Res. 97 (2006) 539–542. https://doi.org/10.3139/146.101270.

[198] B.A. Pint, K.L. More, I.G. Wright, P.F. Tortorelli, Characterization of thermally cycled alumina scales, Mater. High Temp. 17 (2000) 165–171. https://doi.org/10.1179/mht.2000.024.

[199] B.A. Pint, K.L. More, Characterization of alumina interfaces in TBC systems, J. Mater. Sci. 44 (2009) 1676–1686. https://doi.org/10.1007/s10853-008-3221-x.

[200] B. Pint, The oxidation mechanism of θ-Al2O3 scales, Solid State Ionics 78 (1995) 99–107. https://doi.org/10.1016/0167-2738(95)00013-V.

[201] A. Zeller, F. Dettenwanger, M. Schütze, Influence of water vapour on the oxidation behaviour of titanium aluminides, Intermetallics 10 (2002) 59–72. https://doi.org/10.1016/S0966-9795(01)00104-2.

[202] N.H. Leeuw, S.C. Parker, Effect of Chemisorption and Physisorption of Water on the Surface Structure and Stability of alpha-Alumina, J. Am. Ceram. Soc. 82 (1999) 3209-2316. https://doi.org/10.1111/j.1151-2916.1999.tb02225.x.

[203] E.J. Opila, D.L. Myers, N.S. Jacobson, I.M.B. Nielsen, D.F. Johnson, J.K. Olminsky, M.D. Allendorf, Theoretical and experimental investigation of the thermochemistry of CrO2(OH)2(g), The Journal of Physical Chemistry A 111 (2007) 1971–1980. https://doi.org/10.1021/jp0647380.

[204] P.Y. Hou, Impurity Effects on Alumina Scale Growth, J. Am. Ceram. Soc. 86 (2003) 660–668. https://doi.org/10.1111/j.1151-2916.2003.tb03355.x.

[205] T. Boll, K.A. Unocic, B.A. Pint, A. Mårtensson, K. Stiller, Grain Boundary Chemistry and Transport Through Alumina Scales on NiAl Alloys, Oxid. Met. 88 (2017) 469–479. https://doi.org/10.1007/s11085-016-9697-x.

[206] D. Sobieraj, J.S. Wróbel, M.R. Gilbert, A. Litnovsky, F. Klein, K.J. Kurzydłowski, D. Nguyen-Manh, Composition Stability and Cr-Rich Phase Formation in W-Cr-Y and W-Cr-Ti Smart Alloys, Metals 11 (2021) 743. https://doi.org/10.3390/met11050743.

[207] Cr (Chromium) Binary Alloy Phase Diagrams, in: H. Okamoto, M.E. Schlesinger, E.M. Mueller (Eds.), ASM handbooks online, ASM International, 2002, pp. 281–297.

[208] J. Chen, E. Tejado, M. Rasiński, A. Litnovsky, D. Nguyen-Manh, E. Prestat, T. Whitfield, J.Y. Pastor, M. Bram, J.W. Coenen, C. Linsmeier, J. Gonzalez-Julian, Effect of Yttrium and Yttria Addition in Self-Passivating WCr SMART Material for First-Wall Application in a Fusion Power Plant, Metals 14 (2024) 1092. https://doi.org/10.3390/met14091092.

[209] F. Klein, A. Litnovsky, X. Tan, J. Gonzalez-Julian, M. Rasinski, C. Linsmeier, M. Bram, J.W. Coenen, Smart alloys as armor material for DEMO: Overview of properties and joining to structural materials, Fusion Engineering and Design 166 (2021) 112272. https://doi.org/10.1016/j.fusengdes.2021.112272.

[210] R.E. Newnham, Y.M. de Haan, Refinement of the α Al2O3, Ti2O3, V2O3 and Cr2O3 structures, Zeitschrift für Kristallographie 117 (1962) 235–237. https://doi.org/10.1524/zkri.1962.117.2-3.235.

[211] W. Kunnmann, S. La Placa, L.M. Corliss, J.M. Hastings, E. Banks, Magnetic structures of the ordered trirutiles Cr_2WO_6, Cr_2TeO_6 and Fe_2TeO_6, Journal of Physics and Chemistry of Solids 29 (1968) 1359–1364. https://doi.org/10.1016/0022-3697(68)90187-X.

[212] Y. Shimony, L. Ben-Dor, On the crystal structure of $CrWO_4$, Materials Research Bulletin 18 (1983) 331–335. https://doi.org/10.1016/0025-5408(83)90120-4.

[213] S. Tanisaki, Crystal Structure of Monoclinic Tungsten Trioxide at Room Temperature, J. Phys. Soc. Jpn. 15 (1960) 573–581. https://doi.org/10.1143/JPSJ.15.573.

[214] P.R. Rios, A theory for grain boundary pinning by particles, Acta Metallurgica 35 (1987) 2805–2814. https://doi.org/10.1016/0001-6160(87)90280-X.

[215] G. Bayer, Cr_2WO_6, a New Trirutile Compound, Journal of the American Ceramic Society 43 (1960) 495–496. https://doi.org/10.1111/j.1151-2916.1960.tb13705.x.

[216] J.-H. Koh, E. Sorge, T.-C. Wen, D.K. Shetty, Thermal expansion behaviors of yttrium tungstates in the WO3–Y2O3 system, Ceram. Int. 39 (2013) 8421–8427. https://doi.org/10.1016/j.ceramint.2013.04.024.
[217] T. Akermark, The Use of Oxygen Isotopic Labeling to Understand Oxidation Mechanisms, Oxid Met 50 (1998) 167–188. https://doi.org/10.1023/A:1018832103466.
[218] S.-H. Yoo, S.-H. Kim, E. Woods, B. Gault, M. Todorova, J. Neugebauer, Origins of the hydrogen signal in atom probe tomography: case studies of alkali and noble metals, New J. Phys. 24 (2022) 13008. https://doi.org/10.1088/1367-2630/ac40cd.

List of Abbreviations

1D	One Dimensional
2D	Two Dimensional
3D	Three Dimensional
APS	Average Particle Size
APT	Atom Probe Tomography
CSP	Concentrated Solar Power
CTE	Coefficient Of Thermal Expansion
DBTT	Ductile-to-Brittle Transition Temperature
DEMO	DEMOnstration Power Plant
DR	Detection Rate
EDM	Electrical Discharge Machining
EDX	Energy Dispersive X-ray Spectroscopy
FAST	Field Assisted Sintering Technology
FIB	Focused Ion Beam
GB	Grain Boundary
GHG	Greenhouse Gas
GIS	Gas Injection System
GTAW	Gas Tungsten Arc Welding
HAADF	High-Angle Annular Dark-Field
HIP	Hot Isostatic Pressing
HTF	Heat Transfer Fluid
ITER	International Thermonuclear Experimental Reactor
IVAS	Integrated Visualization and Analysis Software
JET	Joint European Torus
KB	Kink Band
LEAP	Local Electrode Atom Probe
LMIS	Liquid Metal Ion Source

LOCA	Loss-Of-Coolant Accident
LPE	Laser Pulse Energy
MCF	Magnetic Confinement Fusion
MFC	Mass Flow Controller
ODS	Oxide Dispersion Strengthened
PBR	Pilling-Bedworth Ratio
PCA	Process Control Agent
RH	Relative Humidity
SDD	Silicon Drift Detector
SEM	Scanning Electron Microscopy
SIMS	Secondary Ion Mass Spectrometry
SMART	Self-passivating Metal Alloys with Reduced Thermo-oxidation
SNMS	Secondary Neutral Mass Spectrometry
SPS	Spark Plasma Sintering
STEM	Scanning Transmission Electron Microscopy
TEM	Transmission Electron Microscopy
TGA	Thermogravimetric Analysis
UHV	Ultra-High Vacuum
XRD	X-ray Diffraction

Elements:

Al	Aluminium
Ar	Argon
B	Boron
C	Carbon
Ce	Cerium
Co	Cobalt
Cr	Chromium
Cu	Copper
D	Deuterium

Fe	Iron
Ga	Gallium
H	Hydrogen
He	Helium
Hf	Hafnium
K	Potassium
La	Lanthanum
Li	Lithium
Mg	Magnesium
Mn	Manganese
Na	Sodium
Nb	Niobium
Ni	Nickel
O	Oxygen
P	Phosphorous
Re	Rhenium
S	Sulphur
Si	Silicon
T	Tritium
Ta	Tantalum
Th	Thorium
Ti	Titanium
V	Vanadium
W	Tungsten
Xe	Xenon
Y	Yttrium
Zr	Zirconium

List of Figures

List of Tables

List of Publications

Part of this thesis has been published in the following journal articles:

- A. Reuban, I. Povstugar, M. Rasiński, A. Vayyala, A. Litnovsky, J.W. Coenen, C. Linsmeier, O. Guillon, J. Gonzalez-Julian, Unveiling the diffusion pathways under high-temperature oxidation of Cr_2AlC MAX phase via nanoscale analysis, Corrosion Science 235 (2024) 112179. https://doi.org/10.1016/j.corsci.2024.112179

- A. Reuban, J. Chen, I. Povstugar, A. Litnovsky, J.W. Coenen, C. Linsmeier, J. Gonzalez-Julian, The Effect of Y Addition on Oxidation Resistance of Bulk W-Cr Alloys, Materials 17 (2024) 5749. https://doi.org/10.3390/ma17235749

Acknowledgements

First of all, I would like to thank my Doktorvater, Prof. Jesus Gonzalez-Julian, for his guidance, encouragement and support during the course of my PhD. I am also grateful to my supervisor at IFN-1, Dr. Andrey Litnovsky, for his supervision, help with administrative issues and the lively scientific discussions during the weekly group meetings.

I feel grateful that I had a very supportive scientific advisor, Dr. Ivan Povstugar, who taught me not only the principles of APT and FIB-SEM, but also how to think critically and be an individual scientific researcher. Thank you for always being available for discussions, even on short notice, and providing detailed and useful feedback on my work, it has greatly helped me grow as a scientist.

I would like to thank all my supervisors, as well as Prof. Christian Linsmeier, Prof. Bernhard Unterberg, Prof. Jan Coenen, the institute administration and the HITEC Graduate School for making sure I was comfortable and settled in, especially during my initial months in Germany in the middle of the Covid-19 pandemic, quarantine and lockdowns.

Although I was officially part of three institutes – IMD-2, IFN-1 and the erstwhile ZEA-3 – IFN-1 was where I spent most of my time when not at HNF, and the people here made it feel like a second home for me. I would like to thank everyone who trained me to use the various characterisation tools at the institute – Dr. Marcin Rasinski, Dr. Anne Houben and Ms. Beatrix Goeths. I would also like to thank Dr. Timo Dittmar for many insightful discussions. Thanks to Melina Poll from IMD-2 and Dr. Ashok Vayyala from ER-C for help with providing samples and TEM analysis.

To all the doctoral researchers and master students at IFN-1, you were more than just colleagues. Thank you for being great friends and for always being there when I needed support, whether it was in the lab or my personal life. Thank you Jie, Pawel, Gunnar, Leonardo, Tom, Xuejiao and Xiaoyue, the people I have been with as part of the SMART alloy group, for the enriching discussions and lunches together. Jie, you have been an amazing friend and colleague for the entirety of my time here, I enjoy all our discussions both work and not work related. You always have a refreshing perspective on life and it was fun travelling and attending conferences with you.

Christoph, Meike, Fatma, Erik, Alex, Eddy, Fabienne, Jannik and Sebastian, thank you for the enjoyable discussions at the PhD seminars and over food, whether it was at the institute, Seecasino or outside FZJ, and being fun teammates at the monthly Pub Quiz.

Christoph, thank you for trying to cheer me up when I'm down and the fun cooking sessions. Meike, you are one of the sweetest and most resilient people I have met, and I am glad I could share the office with someone like you. Fatma, thanks for being a great friend, even though we seldom get to meet, you are probably the person I have the most in common with here.

Daria, Mythreyi and Srinivas, you were my pillars of support from three corners of the world. Srinivas, thank you for being a great friend and mentor over the years. You give the best professional and personal advice and I appreciate that you always tell me what I need to hear. Daria and Mythreyi, the weekend phone calls with you kept me going throughout my time here. Thank you for being such amazing friends and confidantes ever since undergrad at insti, helping me get through the bad times and being someone I can always share a good laugh with.

Finally, I would like to thank my family, my parents and my sister Sheeba, for supporting my decision to pursue a PhD, and for your unconditional love and encouragement through it all. You celebrated every small success with me and I am grateful for every phone call with you, it was a small reminder of home and made me feel less alone staying on my own in a new country for more than three years.

And at last, she knew what the agony had been for.

– Taylor Swift, "The Manuscript"

Band / Volume 663
Advances in Understanding Nitrate Aerosol Formation and the Implications for Atmospheric Radiative Balance
A. Milousis (2025), 195 pp
ISBN: 978-3-95806-823-0

Band / Volume 664
Optimization of NaSICON-type lithium-ion conductors for solid-state batteries
A. Loutati (2025), viii, 104 pp
ISBN: 978-3-95806-824-7

Band / Volume 665
Innovative Plasma Sprayed Thermal Barrier Coatings for Enhanced Flexibility in Gas Turbine Operation
J. Igel (2025), V, 153, XXXVI pp
ISBN: 978-3-95806-827-8

Band / Volume 666
Techno- ökonomisches Potenzial dezentraler und autarker Energiesysteme
S. K. A. Risch (2025), xxiii, 210 pp
ISBN: 978-3-95806-829-2

Band / Volume 667
Reactive Field Assisted Sintering of Novel Rare Earth Garnets for Plasma Etching Applications
C. Stern (2025), VII, 101, XXVIII pp
ISBN: 978-3-95806-833-9

Band / Volume 668
Effects of mucilage and extracellular polymeric substances on soil gas diffusion
A. Haupenthal (2025), v, 99 pp
ISBN: 978-3-95806-834-6

Band / Volume 669
Quantifying Recombination Losses and Charge Extraction in Halide Perovskite Solar Cells
L. Krückemeier (2025), vi, 286 pp
ISBN: 978-3-95806-835-3

Band / Volume 670
Investigation of Dynamic Material Changes During the Preparation of ZnPd Nanoparticles Supported on ZnO and their Catalytic Application in Methanol Steam Reforming on the Atomic Level
A. Meise (2025), xviii, 175 pp
ISBN: 978-3-95806-838-4

Band / Volume 671
Improving Energy Efficiency of Public Buildings by Influencing Occupant Behaviour using Dashboards and Gamification
E. Ubachukwu (2025), xxi, 191 pp
ISBN: 978-3-95806-840-7

Band / Volume 672
Exploring Plant Responses to Changing Environments: Integrating Phenotyping and Modeling Across Scales
F. M. Bauer (2025), xxix, 188 pp
ISBN: 978-3-95806-845-2

Band / Volume 673
A constitutive theory to represent non-idealities in contacting of SOC interconnect contacts
R. M. Pinto (2025), xii, 139 pp
ISBN: 978-3-95806-846-9

Band / Volume 674
Strontium titanate based materials for use as oxygen transport membranes in membrane reactors
Y. Tang (2025), XIV, 132 pp
ISBN: 978-3-95806-849-0

Band / Volume 675
Scaling Methods for the Production of Tungsten Fiber-Reinforced Composites via Chemical Vapor Deposition
A. Lau (2025), untersch. Pag.
ISBN: 978-3-95806-851-3

Band / Volume 676
Nanoscale analysis of high-temperature oxidation mechanisms of Cr_2AlC MAX phase and W-Cr-Y self-passivating tungsten alloy
A. J. S. Reuban (2025), ix, 142 pp
ISBN: 978-3-95806-855-1

Energie & Umwelt / Energy & Environment
Band / Volume 676
ISBN 978-3-95806-855-1

Mitglied der Helmholtz-Gemeinschaft

JÜLICH
Forschungszentrum